DISSERTATION

SINK MARK DETECTION ON HIGHLY REFLECTIVE PLASTICS SURFACES

AUTHORED BY

DIPL.-ING. JOHANNES MACHER

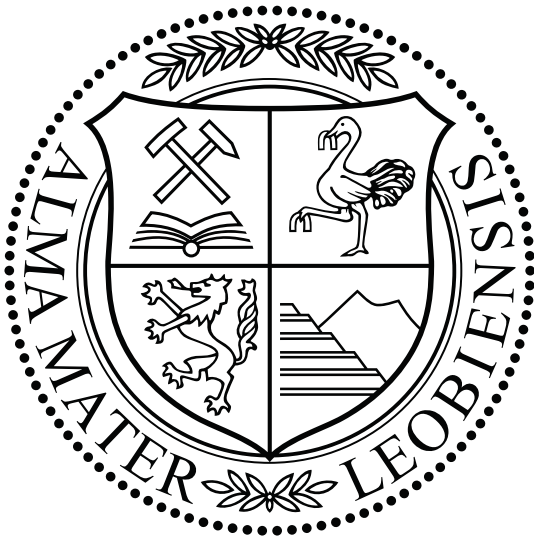

MONTANUNIVERSITÄT LEOBEN

CHAIR FOR INJECTION MOULDING OF POLYMERS

POLYMER COMPETENCE CENTER LEOBEN GMBH

KUNSTSTOFF TECHNIK LEOBEN

SPRITZGIESSEN VON KUNSTSTOFFEN

PCCL

Polymer Competence Center Leoben

Leoben, September 2014

Dipl.-Ing. Johannes Macher: *Sink Mark Detection on Highly Reflective Plastics Surfaces*, © September 2014

SUPERVISORS:
Dipl.-Ing. Dr.techn. Dieter P. Gruber
Univ.-Prof. Dipl.-Ing. Dr.mont. Walter Friesenbichler
O.Univ.-Prof. Dipl.-Ing. Dr.techn. Paul O'Leary

LOCATION:
Leoben

TIME FRAME:
September 2014

AFFIDAVIT

I declare in lieu of oath, that I wrote this thesis and performed the associated research myself, using only literature cited in this volume.

Leoben, September 2014

Johannes Macher

For my parents and Barbara
- Thanks for your support and patience

ABSTRACT

The appearance of plastics products has become one of the major factors for the buying decision of customers. Especially curved high-quality front panels with mostly black high-gloss surface enhance the look of products. However, sink marks are prominent on such surfaces, even when their depth is in the lower range of microns. In the given work, sink mark detection which is based on phase measuring deflectometry is evaluated in a laboratory testing site. Additionally, a concept design for the integration of such a testing site into an injection molding process line is introduced. In this design, a unit for sample positioning was added to the basic deflectometric setup to enable total inspection of curved high-gloss surfaces. For evaluation of the inspected surface, a model was developed to calculate sink mark intensity from sink mark curvature and area. Therein, polynomial base functions were implemented in the image processing algorithms. The main application of the polynomials was the smoothing and differentiation of the data. This approach allowed for the robust calculation of surface curvature from the deflectometric results which are proportional to the first derivative of the surface. The results for sink mark intensity were compared to topographic measurements which were obtained by a chromatic coding confocal microscope. The topographic measurements were modelled with a Gaussian-like function. The function allows for description of sink mark shape with few parameters and facilitates the calculation of features which can be used to evaluate sink mark visibility. Despite the fact that the two measurement methods are based on different principles, the results of topographic and deflectometric measurements show high correlation. For this reason, deflectometric measurements of sink marks on at least black high-gloss surfaces can be calibrated with data from topographic measurements.

ZUSAMMENFASSUNG

Das Erscheinungsbild von Kunststoffteilen rückt immer mehr in den Vordergrund bei Kaufentscheidungen von Kunden. Vor allem gekrümmte, hochqualitative Blenden mit meistens schwarzer Hochglanzoberfläche werden verwendet, um das Aussehen von Produkten zu verbessern. Allerdings treten gerade auf solchen Oberflächen auch Einfallstellen ausgeprägt in Erscheinung, die eine Tiefe von wenigen Mikrometern aufweisen. In dieser Arbeit wird eine Methode zur Qualitätskontrolle in einem Laborprüfstand evaluiert, die auf der Anwendung der phasenmessenden Deflektometrie basiert. Zusätzlich wird ein Konzeptdesign für die Einbindung eines solchen Prüfstands in eine Spritzgussprozesslinie vorgestellt. In dem Konzept wurde der grundlegende Aufbau für die deflektometrische Messung um eine Einheit für die Probenpositionierung ergänzt, um eine vollständige Inspektion einer Probenoberfläche zur ermöglichen. Die Evaluierung der inspizierten Oberfläche wurde mithilfe eines Modells ermöglicht, mit dem die Intensität von Einfallstellen basierend auf ihrer Krümmung und Fläche berechnet wurde. Dabei wurden polynomiale Basisfunktionen in die Image-Processing-Algorithmen eingebunden, mit denen vor allem die Datensätze geglättet und differenziert wurden. Dieser Ansatz ermöglichte die robuste Berechnung der Oberflächenkrümmung aus den deflektometrischen Messresultaten, die proportional zur ersten Ableitung der Oberfläche sind. Die so berechneten Resultate für Einfallstellenintensität wurden mit topografischen Messungen verglichen, die mit einem chromatisch-kodierten Konfokalmikroskop erhalten wurden. Dabei wurden die topographischen Messungen mit einer der Gaussfunktion ähnlichen Funktion modelliert, mit der die Einfallstellenform mit wenigen Parametern beschrieben werden kann. Zusätzlich erlaubt dieser Ansatz die Berechnung von Merkmalen, mit denen die Einfallstellensichtbarkeit evaluiert werden kann. Obwohl die beiden Methoden auf unterschiedlichen Prinzipien basieren, weisen die topografischen und deflektometrischen Messresultate eine hohe Korrelation auf. Aus diesem Grund können deflektometrische Messungen von Einfallstellen auf zumindest schwarzen Hochglanzoberflächen mit topografischen Messungen kalibriert werden.

PUBLICATIONS

Some ideas and figures have previously appeared in the following publications:

ARTICLES IN PEER-REVIEWED JOURNALS

[J1] D. P. Gruber, J. Macher, D. Haba, G. R. Berger, G. Pacher, and W. Friesenbichler. "Measurement of the visual perceptibility of sink marks on injection molding parts by a new fast processing model." In: *Polymer Testing* 33 (2014), pp. 7–12. ISSN: 01429418. DOI: 10.1016/j.polymertesting.2013.10.014.

[J2] J. Macher, D. P. Gruber, T. Altenbuchner, G. A. Pacher, G. R. Berger, and W. Friesenbichler. "A Novel Sink Mark Model for High Gloss Injection Molded Parts - Correlation of Deflectometric and Topographic Measurements." In: *Polymer Testing* 39 (2014), pp. 12–19. DOI: 10.1016/j.polymertesting.2014.07.001.

[J3] J. Macher, D. P. Gruber, T. Altenbuchner, G. A. Pacher, G. R. Berger, and W. Friesenbichler. "Detection of Visually Perceptible Sink Marks on High Gloss Injection Molded Parts by Phase Measuring Deflectometry." In: *Polymer Testing* 34 (2014), pp. 42–48. DOI: 10.1016/j.polymertesting.2013.12.008.

ARTICLES IN CONFERENCE PROCEEDINGS

[C1] J. Macher, D. P. Gruber, G. R. Berger, and W. Friesenbichler. "Application of Deflectometry for Surface Inspection of High-Glossy Injection-Molded Facing Parts." In: *Austrian-Slovenian Polymer Meeting*. Bled, Slovenia, 2013.

[C2] J. Macher, D. P. Gruber, G. R. Berger, and W. Friesenbichler. "New Methods for Quality Control of Injection-Molded Parts." In: *ANTEC - Conference and Tradeshow*. Cincinnati, USA, 2013.

There are two ways of spreading light:
To be the candle or the mirror that reflects it.

—Edith Wharton

ACKNOWLEDGMENTS

The research work of this dissertation was performed at the Polymer Competence Center Leoben GmbH (PCCL, Austria) within the framework of the COMET-program of the Federal Ministry for Transport, Innovation and Technology and the Federal Ministry of Economy, Family and Youth with contributions by the University of Leoben (*Chair of Injection Moulding of Polymers*), Wittmann Battenfeld GmbH and Schöfer GmbH. The PCCL is funded by the Austrian Government and the State Governments of Styria and Upper Austria.

SPECIAL THANKS GO TO:

Dipl.-Ing. Dr.techn. Dieter P. Gruber
who offered me the opportunity for this thesis. During my work at the PCCL, he continually guided me with his advice and experience.

Univ.-Prof. Dipl.-Ing. Dr.mont. Walter Friesenbichler and
O.Univ.-Prof. Dipl.-Ing. Dr.techn. Paul O'Leary
for academic counselling and assessment of the thesis.

my colleagues at the PCCL for their support during the work for this thesis, especially:

Dipl.-Ing. Thomas Altenbuchner
for his help with the electronics of the testing sites

Dipl.-Ing. Gernot Pacher
for the discussions about sink mark formation

Robert Hinterberger
for his assistance with the photographic presentation of the parts and the testing sites

CONTENTS

1 INTRODUCTION

1.1 MOTIVATION

Besides functionality, the appearance of plastic products has become one of the major factors for the buying decision of customers. Especially, high-gloss plastics front panels, which have become complexly shaped in recent times, enhance the look of products. Fast and reproducible production of such parts is facilitated by injection molding, since even complex parts can be produced rapidly and cheaply after the investment in a mold. However, due to properties of plastics such as their low hardness compared to inorganic materials, their low thermal conductivity or their relatively high thermal expansion coefficient, plastics engineers have to consider specific rules for the conception and production of injection molded parts [73].

Nevertheless, because of the need to ensure the functionality of the parts and their aesthetic appearance as well as to reduce costs, designers have to violate the rules of plastics manufacture. For this reason, such parts are prone to surface defects. Sink marks, which are caused by characteristic thermal shrinkage of plastics and local geometry of the part, are one common type of surface defects related to injection molding. Especially on high-gloss surfaces, this defect type can influence the appearance considerably due to distorted reflections of the surroundings on the defected surface area.

Traditionally, quality inspection is performed manually, despite the fact that sink marks in particular are hard to evaluate reproducibly by human observers when the visibility of defects is close to the threshold of perceptibility [53]. Also, human observers are prone to fatigue and boredom which prevents objective part evaluation [15, 83]. Machine vision methods would ensure 100%-inspection with objective and reproducible results. However, the inspection of high-gloss parts is still challenging, since the reflection of the surroundings outshines the reflection of the surface itself, causing virtual invisibility of the surface. For this reason, methods exist which provide information about the shape of the inspected part's surface by evaluating how the surface influences the reflection of the surroundings, a point light source or a known light pattern.

In this work, the applicability of the phase measuring deflectometry, which was introduced by Horneber et al. [63], is analyzed especially for

the detection of sink marks on high-gloss injection molded parts. The measurement results are evaluated using a mathematical model which correlates sink mark perceptibility to a numerical value. Additionally, smoothing and differentiation of the measurement results, which is essential for the processing of the measurement results, is accomplished by implementation of polynomial base functions [50, 87, 89, 91]. Parallel conducted measurements of the inspected sink marks with a commercial chromatic coding confocal microscope are used for the evaluation of the measurement results.

1.2 STATE OF THE ART

Since the advent of digital image processing, machine vision methods have become increasingly important for quality inspection. Extensive reviews [75, 122] exist which describe texture analysis methods. These methods detect surface defects in surface textures which result from the interaction between surface structure and shadowing, which in turn is created by the setup of the lighting. The importance of suitable lighting for reliable defect detection was investigated for example by Chantler [19, 20] and Chantler and McGunnigle [21]. They analyzed the influence of the lighting setup on the textures of surfaces and found that the detectability of surface defects is strongly dependent on the direction of light incidence.

Parallel extensive studies have been carried out to measure the reflective behavior of surfaces. As an example, the bi-directional reflection function (BRDF), which describes the reflection of a surface depending on the direction of light incidence mathematically, was introduced by the National Bureau of Standards [86]. The advancement of automation technology and electronics such as six-axle-robots or new light sources allowed the development of several methods for the measurement of the BRDF in the last few years [13, 25, 26, 45, 52].

The BRDF is a convenient way to describe two extreme cases of surface reflection: Diffuse reflection and specular reflection. Surfaces with diffuse reflection reflect light proportional to a cosine squared distribution independent to light incidence, while specular reflecting surfaces reflect incoming light mirrorlike. In nature, surfaces never reflect light purely diffusely or specularely. Real surfaces' reflection consists of diffuse and specular reflection in a specific ratio which defines several aspects of surface appearance like for example gloss or distinctness of image. Gruber et al. found surface inspection methods that are based on analysis of texture or distinctness of image. Such methods facilitate the detection of

defects [39, 42] or the evaluation of gloss [36, 44] on plane surfaces in correlation to human perception.

For curved surfaces, the mentioned methods have to be adapted, since the direction of light incidence in relation to the surface normals changes with the position on the surface [112]. On plane or slightly curved surfaces the direction of light incidence is approximately constant for a suitably small region of interest whose size is dependent on the distinctness of surface curvature. In the respective regions of interest the morphology of surface texture can be evaluated similar to plane surfaces [79, 112].

If either the surface curvature is too pronounced or if larger regions of a surface have to be evaluated at once, machine vision methods have to be applied which are explicitly developed for quality inspection or metrological reconstruction of curved surfaces. Comprehensive reviews concerning the most common methods for reconstruction and inspection of curved surfaces are given [8, 65, 109, 110, 118]. Many of these methods base on image fusion where the shape of the inspected object is calculated from several images of the object. However, the physical and mathematical principles behind these methods differ considerably. For this reason, the described methods are applicable for surfaces with specific reflection properties. Knowledge about the working principle helps to evaluate the applicability of a method for the given problem. For this reason, the working principles of the most prominent methods are shortly described.

Triangulation methods calculate the 3D position of a surface point as an intersection of two or more lines of sight or lines of light incidence. Photogrammetry (e.g. [3, 51]) is a triangulation method where two or more different cameras photograph an object. The 3D information about the object is calculated from the fusion of the images and knowledge about the respective position and viewing direction of the cameras. For this reason, it is imperative for image fusion to recognize specific points of the object surface which have to be detected with high contrast in preferably all measurement images. Therefore, this method works best when the surface is captured with high contrast regardless of the viewing directions of the cameras. This implies that this method works best on diffusely reflecting structured surfaces.

Light sectioning methods (e.g. [80, 113]) and fringe projection methods (e.g. [31, 103, 123]) are other triangulation methods where one of the cameras is replaced by a laser or a projector respectively. In this case, triangulation happens between the line of sight of the camera(s) and the line of incident light of the laser or projector. Since the laser line of the light sectioning or the known light pattern of the fringe projection are easier to detect than random points on an object's surface, these methods are more robust than photogrammetry. Nevertheless, the images of the light

patterns on the object surface have to be high-in-contrast. However, the contrast and the lighting of high-gloss surfaces changes with the viewing or lighting direction relative to the surface slope. Therefore, the working principle of these methods also requires diffusely reflecting surfaces.

Photometric stereo (e.g. [22, 58]) is a shape-from-shading method. The measuring setup normally consists of one fixed camera and three or more point light sources at defined positions. The lights are switched on subsequently with the camera imaging the surface of the inspected object for each lighting situation. Depending on the structure and shape of the surface, each image shows different shadowing on the surface. Image fusion gives information about the slope of the surface. Since highlights would outshine the surrounding surface, this method cannot be applied on high-gloss surface without considerable effort.

Interferometry (e.g. [81]) denotes methods where coherent light, mostly laser light, is reflected from a mirroring surface and interfered with itself. The image of the interference contains information about the quality of the mirroring surface. Specular reflecting surfaces can be inspected and reconstructed with high accuracy and resolution. However, interferometric methods are normally slow and require expensive specialized optics for inspection of non-plane surfaces.

Deflectometric methods on the other hand are well-suited for the measurement of specularely reflecting surfaces, since they relate the diffractions in surface reflections of known patterns to the shape of the respective surfaces. The Moiré diffraction method is one of the first methods which base on this concept. A comprehensive review about this method can be found in [24]. A coherent light beam, most often a laser, is deflected by successively arranged lattices which causes an interference pattern on the inspected surface. The pattern changes with different surface shapes. Ritter and Hahn [106] enhanced this approach with their reflecting grating method where only one lattice is used. Healey and Binfort developed specular reflectance models based on approximations of the BRDF to relate specular reflection to the shape of the inspected object [54]. Auluck implemented strongly diffracting gratings in his setup, which enabled the specific selection of diffraction order of the beam which emerged from the first grating [4]. Recombination of these orders at a defined distance to the gratings ensured a considerable increase in sensitivity of the measurements. Halstead et al. reconstructed surface models of the human cornea from the reflections of light patterns from the eye surface by fitting the measured sets of surface normals to surface models with B-splines [47]. Wang et al. reconstructed aspheric specularly reflecting surfaces using Phase-Shifting Moiré Deflectometry [116]. Their approach was the application of the Fourier Transform before phase-shifting which facilitated a

more robust reconstruction while the number of required images could be decreased.

In 2000, Horneber et al. introduced the phase measuring deflectometry in a report at the University of Erlangen-Nürnberg [63]. They used a projector to project a light pattern on a screen which was reflected by a surface into a camera. By application of phase-shifting algorithms, they could calculate a relationship between the light pattern on the screen and the image of the camera. Since this relationship is proportional to the normal vector sets of the surface, it contains information about the first derivative of the surface.

Based on their work, Kammel and León proposed this method for quality inspection of high-gloss surfaces [69, 70, 72]. They exploited that deflectometry measurements contain direct information about the surface slope and postulated that the derivatives of the measurements correspond to the directional curvatures of the inspected surface. Finally, the principal curvatures where calculated from the measurement results in accordance with the mathematical theory of differential geometry. Defect detection and evaluation were carried out by comparing a sample's measurement with the measurement of a provided "Golden sample".

Werling and Beyerer introduced the concept of inverse patterns [120]. The generated light patterns were adapted in such a way that the camera captured the undisturbed pattern in the reflection from the surface of a good part. During inspection any surface defect would be detected as disturbance of the reflected pattern. For the detection of a defect only one single frame has to be captured. However, this method is dependent on a stable measurement setup, since slight variations in the setup lead to artifacts in the measurement and therefore to reduced measurement precision. Further research on the phase measuring deflectometry concerns the metrological reconstruction of specularly reflecting surfaces. Additional information has to be introduced from other measurement concepts, since the method gives ambiguous absolute information about normal vector sets of a measured surface.

Balzer et al. used additional information which resulted from shape from shading methods for the metric reconstruction of billiard balls [6]. Lellmann et al. evaluated the optical flow of specularly reflecting surfaces to generate suitable models for the calculation of the reconstruction [78]. Horbach and Dang used two different screen positions for each measurement [62]. Comparison of the two measurements would identify the correct set of surface normal vectors for reconstruction. Contrary to the former approach, Balzer and Werling used two different camera positions to resolve the ambiguity of the normal vector sets [5]. In newer approaches, infra-red wavelength patterns are generated for the deflecto-

metric measurement of rougher surfaces or objects which are transparent in the visible spectrum [59–61].

In the last few years some commercial applications of the Phase Measuring Deflectometry have entered the market. The SpecGage created by 3D-Shape GmbH [1] enables the deflectometric measurement of lenses, silicium wafers and reflectors and can be realized for stand-alone applications as well as for in-line inspection. Small parts especially can be inspected with high accuracy. The SurfMax by Carl Zeiss OIM GmbH [18] enables the in-line inspection of glossy to high-glossy surfaces. The defect detection is carried out with a combination of gray-scale images, deflectometric measurements and gloss measurements which facilitate the detection of a wider range of defects like pores or dents. This system facilitates the inspection of ring-shaped and cylindrical parts as well as plane front panels.

1.3 CONTRIBUTION OF THIS WORK

The main contributions of this work are:

1. The evaluation of the applicability of the phase measuring deflectometry for the detection of sink marks in an injection molding process line for curved plastic parts. As far as we know, there is no other mention of such a concept in literature. The problems and challenges of such an approach will be the focus of this work. The deflectometric measurement is used for quality inspection, in contrast to metrological reconstruction of the surface shape of the inspected parts.

2. The introduction of a model for the perceptibility of sink marks on black high-gloss injection molded parts. The model is mainly based on the second derivative of surfaces, since former works at the PCCL and in literature suggest that the perceptibility of surface defects is proportional to the second derivative of the surface in the defect surface area [42, 43, 53]. Since the results of the deflectometric data are proportional to the first derivatives of the surfaces, differentiation of the data is necessary.

3. The implementation of polynomial base functions in the image processing algorithms. The main application of the polynomials in this work is smoothing and differentiation of data. This mathematical tool was developed at the Montanuniversitaet Leoben [50, 87, 89, 91], where it is used for the numerical calculation of differential problems. The application of polynomial base functions could also

facilitate the development of metrological reconstruction algorithms from the quality inspection algorithms which are introduced in this work.

4. The comparison and evaluation of deflectometric results of sink marks with shape measurements using a chromatic coding confocal microscope. The shape of the sink marks is modelled with Gaussian-like bell function. The model facilitates the calculation of features such as volume and amplitude of the sink marks which are used for visibility evaluation of sink marks on black high-gloss plastic parts.

1.4 OUTLINE OF THE THESIS

In Chapter 2, which introduces the theoretical background of this work, four main topics are approached. First, the basic principles of light reflection at surfaces are covered. Second, the basic concepts of injection molding and the formation of sink marks are addressed. Third, the theoretical background of the deflectometric measurement is explained. Finally, the theoretical background of the polynomial base functions is introduced.

In Chapter 3, the measurement setup for the deflectometric measurements is described for a laboratory environment. The sequence of a single measurement cycle is explained. Thereby, the major components of the setup are listed and their functional interaction is illustrated. Most importantly, a method for sample handling which enables the inspection of curved injection molded parts and a method for sink mark evaluation from deflectometric data are introduced.

In Chapter 4, two examples for inspected injection molded parts are described. The first part can be described comparatively simple with polynomial equations while the second part features different curvatures at different surface locations as well as a diffusely reflecting print pattern on the black high-gloss surface. The first part was used for comprehensive evaluation of sink mark detection with phase measuring deflectometry. For this reason, several test series of the injection molded part were manufactured under specified process parameters. These parts were used in the deflectometric measurements. Additionally, measurements with a chromatic coding confocal microscope were compared with the deflectometric data. Thereby, a model was developed for the description of sink mark shape.

The second injection molded part, on the other hand, is designed according to the current fashion in industry. In the second part of Chapter 4 the applicability of the developed methods on such comparatively complex surfaces is shown. Additionally, the design conception of an in-line

testing site in the injection molding process line of the injection molded part is introduced.

The outlook for future work based on the results of this thesis and the summary of this work are presented in Chapter 5 and Chapter 6, respectively.

2

THEORY

2.1 OPTICS

2.1.1 *Electromagnetic Waves*

Since deflectometric measurements are subject to the laws of optical material properties and surface reflection, a short introduction to the principles of light-matter interaction is needed. In this section, the basics of the reflection of electromagnetic waves at surfaces are discussed. The theory of reflection and transmission of light has to fulfill Maxwells's theory of electrodynamics [10, 38, 55]. Because the focus of this work lies on samples made of plastics, the discussion is restricted to dielectric media. As one solution of Maxwell's theory, the strengths of the electric field $E(r)$ and the magnetic field $H(r)$ caused by a plane wave are given by

$$E(r) = E_0 \exp\left[i(k\,r - \omega\,t)\right] \tag{2.1}$$

and

$$H(r) = H_0 \exp\left[i(k\,r - \omega\,t)\right] \tag{2.2}$$

respectively. k is the wave vector, $\omega = 2\pi f$ is the angular frequency and $r = (x, y, z)^T$ is the position vector. For the derivation of material transmission and reflection, plane waves are convenient because relationships of linear optics can thus be described in a shorter way. Additionally, it is convenient to introduce a complex wave vector for electromagnetic waves in dielectric media. By using Equation 2.1, a plane wave is given by

$$E(x) = E_0 \exp\left[i(K\,x - \omega\,t)\right] \tag{2.3}$$

for a progress in x direction. In Equation 2.3 the wave vector k becomes a scalar, while the wave number K[1] is

$$K = k + i\,\alpha. \tag{2.4}$$

Substitution of Equation 2.4 into Equation 2.3 gives

$$E(x) = E_0 \exp(-\alpha\, x) \exp[i(k\, x - \omega\, t)] \tag{2.5}$$

The factor $\exp(-\alpha\, x)$ defines a decrease of the amplitude of the wave along its path through the dielectric medium. Since the intensity of the wave is proportional to the squared absolute value of the wave's amplitude, an absorption coefficient of the medium can be calculated from α. The complex index of refraction N is related to the complex wave number by the following expression

$$N = n + i\,\kappa = \frac{c}{\omega} K \tag{2.6}$$

Thereby, c is the light speed in vacuum, n is the real component of the index of refraction, and κ is the extinction coefficient. Thereby, the real part of the index of refraction n is also defined as the ratio between the phase speed v of the electromagnetic wave in the dielectric medium and the light speed c. This relationship can be derived from the phase factor $\exp[i(kx - wt)]$ by Equation 2.6 in the following way

$$v = \frac{\omega}{k} = \frac{c}{n}. \tag{2.7}$$

2.1.2 *Reflection and Refraction at Plane Interfaces*

Electromagnetic waves that pass through an interface (1) between two media with different indices of refraction, refracted and reflected waves may be considered to emerge from the point of intersection on the interface (Figure 2.1). Due to the conditions of continuity for interfaces, the tangential components of the electric field amplitude E_0 and the magnetic field amplitude H_0 have to be continuous for incident, refracted and reflected waves at the interface.

[1] The wave number is defined as absolute value of the wave vector.

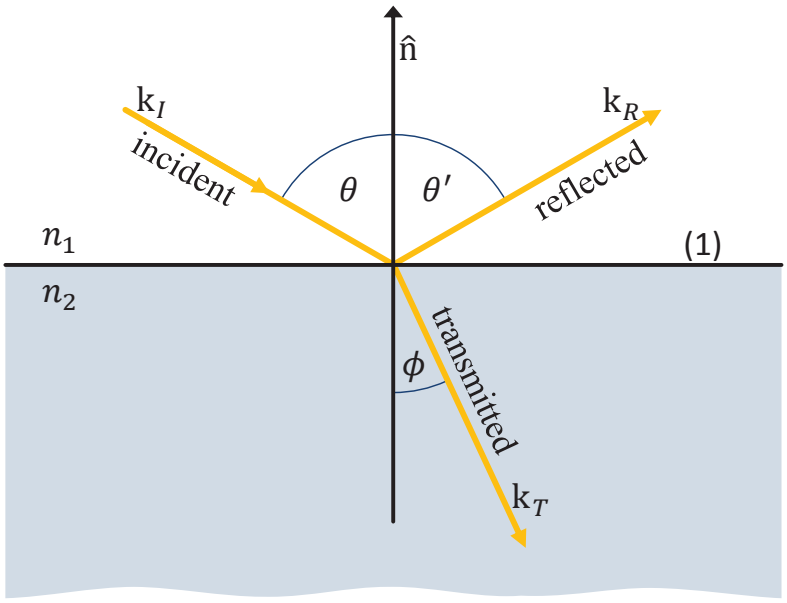

Figure 2.1: Schematics of refraction and reflection of electromagnetic waves at a planar interface.

Therefore, the amplitudes are omitted for further derivation of the relations for reflection and refraction of electromagnetic waves at plane interfaces. Only the phase factors for incident

$$\exp\left[i(k_I r - \omega t)\right] , \tag{2.8}$$

reflected

$$\exp\left[i(k_R r - \omega t + \varphi_R)\right] \tag{2.9}$$

and transmitted waves

$$\exp\left[i(k_T r - \omega t + \varphi_T)\right] \tag{2.10}$$

have to be considered for further derivation. φ_R and φ_T are phase shifts which depend on the coordinates of the point of incidence of the electromagnetic wave at the interface in the respective coordinate system. Since the conditions of continuity have to be valid for all times t, the angular frequency ω stays constant for all phase factors. Additionally, the arguments

of the phase factors have to be equal for all positions r on the interface (1) ($z = z_{(1)}$) which results in the following equations

$$k_I\, r|_{z=z_{(1)}} = k_R\, r + \varphi_R|_{z=z_{(1)}} = k_T\, r + \varphi_T|_{z=z_{(1)}} \tag{2.11}$$

Together with the continuity of the tangential components of the electromagnetic waves, Equation 2.11 ensures that the propagation directions k_I, k_R and k_T of the waves lie in the plane of incidence (co-planarity). For an arbitrary point, the equality of the first two terms in Equation 2.11 is given at the interface

$$(k_I - k_R)\, r|_{z=0} = \varphi_R \tag{2.12}$$

where φ_R depends on the chosen coordinate system. If the origin is chosen to be at the interface (1), it is apparent from Equation 2.11 that φ_R becomes zero.

Since Equation 2.12 is the Hessian normal form of the interface (1), the vector $(k_I - k_R)$ is parallel to the unit normal vector $\hat{n}$ of the interface [55]. The relationship between the wave vectors and the normal vector can be expressed by

$$\hat{n} \times (k_I - k_R) = 0. \tag{2.13}$$

The vector product in Equation 2.13 can be also calculated using the scalar wave numbers of the electromagnetic waves ($\hat{n}$ has length 1) by

$$k_I \sin\theta = k_R \sin\theta'. \tag{2.14}$$

Since the incident and reflected waves propagate in the same medium, the absolute values of the wave vectors k_I and k_R are equal, which corresponds to the law of reflection (see also Figure 2.1)

$$\theta = \theta'. \tag{2.15}$$

Analogous to Equation 2.12, the equality between the first and the third term of Equation 2.11 can be expressed by

$$(k_I - k_T)\, r|_{r\in A_i} = \varphi_T. \tag{2.16}$$

Equation 2.16 is again the Hessian normal form of the interface (1). Therefore, the relationship between incident wave and refracted wave can be calculated analogous to Equation 2.14 by

$$k_I \sin\theta = k_T \sin\phi. \tag{2.17}$$

In the given case, the waves propagate through different media and the wave numbers differ according to the relative optical density of the media. Therefore, the wave numbers are converted into the real indices of refraction for each medium by multiplication of Equation 2.17 with the factor c/ω from Equation 2.7. Subsequent transformation of Equation 2.17 gives Snell's law of refraction (compare Figure 2.1)

$$\frac{\sin\theta}{\sin\phi} = \frac{n_2}{n_1}. \tag{2.18}$$

Snell's law and the law of reflection describe how the phase factors of electromagnetic waves behave at an interface and define the relations between the directions of incident, reflected and refracted wave. A comprehensive description of the behavior of electromagnetic waves at interfaces can only be achieved with the addition of the relation between the amplitudes of the waves. The Fresnel equations describe the ratio between the amplitudes of the electric fields of the incident wave E_I, the reflected wave E_R and the transmitted wave E_T. The derivation of the equations follows from conditions of continuity at the interface for the tangential components of the electric field strength E ($\parallel$) and the magnetic field H ($\perp$). Since most polymers are not ferromagnetic (usually they are diamagnetic), their magnetic susceptibilities χ_m are in the order of 10^{-3} and below[2] [77] . Therefore, it was assumed for this derivation that the magnetic field constants of polymers μ are similar to the magnetic field constant of vacuum μ_0. The Fresnel equations describe the relation between the amplitudes of electromagnetic waves which are polarized parallel and perpendicular to the plane of incidence. Together with the relationship between magnetic and electric field

$$H = \frac{1}{\mu\,\omega}\, k \times E, \tag{2.19}$$

[2]The magnetic susceptibility of a material χ_m can be calculated from its relative magnetic permeability μ_r by $\chi_m = \mu_r - 1$. The relative magnetic permeability μ_r is a material-specific proportionality factor of the magnetic field constant of vacuum μ_0 for the calculation of the magnetic field B inside the material.

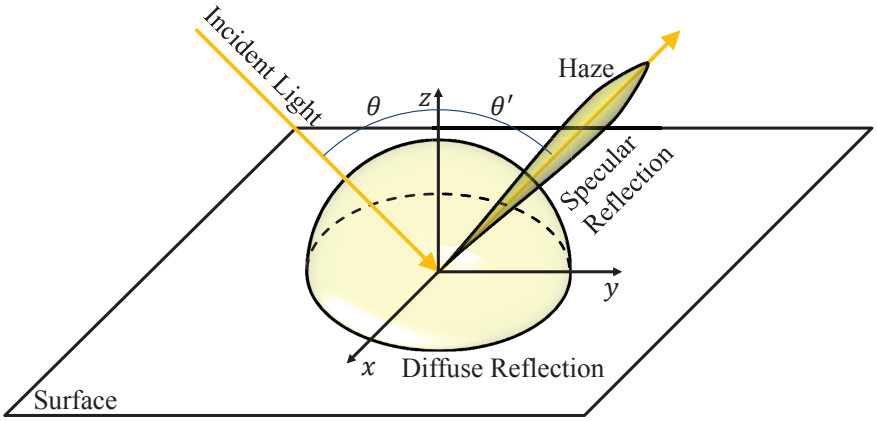

Figure 2.2: Schematics of reflection on surfaces (3D sketch according to [64]).

which can be derived from Maxwell's equations, and Snell's law, the Fresnel equations for the reflection $R_\perp$ and $R_\parallel$ and the transmission $T_\perp$ and $T_\parallel$ coefficients can be calculated by

$$R_\perp = \left[\frac{E_R}{E_I}\right]_\perp = \frac{-\sin(\theta-\phi)}{\sin(\theta+\phi)} \tag{2.20}$$

$$T_\perp = \left[\frac{E_T}{E_I}\right]_\perp = \frac{2\cos\theta\sin\phi}{\sin(\theta+\phi)} \tag{2.21}$$

$$R_\parallel = \left[\frac{E_R}{E_I}\right]_\parallel = \frac{\tan(\theta-\phi)}{\tan(\theta+\phi)} \tag{2.22}$$

$$T_\parallel = \left[\frac{E_T}{E_I}\right]_\parallel = \frac{2\cos\theta\sin\phi}{\sin(\theta+\phi)\cos(\theta-\phi)} \tag{2.23}$$

The Fresnel coefficients only describe reflection properties due to material parameters. An additional factor which influences how objects reflect light is the structure of the reflecting surface. Accordingly, smooth surfaces like mirrors cause specular reflection according to the law of reflection. On the other hand, at rough surfaces incident light is diffusely reflected because the light is scattered by small surface structures which are in many cases randomly conditioned. Accordingly, perfectly diffuse reflection is defined as reflection of light in all directions of the half space above the surface independent of the direction of incident light (Lambert scattering) [55, 84].

The reflection of surfaces in nature as well as most technical surfaces is a superposition of diffuse and specular reflection. In Figure 2.2 both types of reflection are displayed. Additionally the lobe around the peak of specular reflection is sketched, whereby its width correlates with the haze of reflection which defines a decrease of clarity of the reflection [64, 74,

84]. Many models estimate this lobe with a Gaussian distribution (e. g. [23, 117]). Therefore, the reflection of images from surfaces can be modelled as low-pass filtering of an image. However, only black high gloss parts ("piano black") are considered in this work. At such surfaces the diffuse part of reflection is clearly outshone by specular reflection.

2.2 SINK MARKS ON INJECTION MOLDED PARTS

2.2.1 *Fundamentals of Injection Molding*

Injection molding is the most important process to manufacture of plastic parts. The parts are usually produced ready-made and with high reproducibility with this process, which allows the processing of thermoplastics, thermosets or elastomers. However, all injection molded parts which were considered in this work were manufactured from thermoplastics. In the following, the components of an injection molding machine and the sequence of an injection molding process will be summarized [2, 67, 98].

An injection molding machine basically consists of three parts: The injection unit, the mold and the clamping unit. In the injection unit the polymer is melted mostly by inner friction assisted by electric heating. The main component of the injection unit is the screw which conveys and melts the polymer grains and finally transports the melt to the screw antechamber, which is connected to the sprue bush at the beginning of the cycle. The mold is the central part of the injection molding machine. It is usually custom-made for the respective part production and forms the mold cavities which define the shape of the produced parts. The clamping unit closes the mold tightly against the pressures during injection and cooling of the polymer melt and opens the mold for part ejection.

The injection molding process itself is a periodic, non-continuous process where the same sequence of events are cyclically repeated. After the mold is closed, polymer melt is injected through the gate of the mold with set injection velocity and injection pressure. Starting from the gate of the mold, the polymer melt is distributed into the cavities of the mold where the melt is shaped into parts. The melt is cooled due to the thermal exchange between the melt and the mold during the whole cycle. This causes the formation of frozen marginalized layers of the melt at the wall of the mold. Additionally the melt viscosity is continously increased because the temperature of the melt is lowered. When the mold is filled, a holding pressure is applied to compensate the thermal shrinkage of the part until the gate of the mold has frozen. At this time, the screw is set into rotation in preparation of the next injection cycle. The portion of melt for the next shot is accumulated in front of the screw causing the screw

to retract at the same time. When the part is cooled enough to keep its shape, the part is ejected and the next cycle begins.

2.2.2 *Formation of Sink Marks*

Depending on the used polymer, the machine settings and the used mold, several kinds of defects which decrease surface quality can appear on the part. However, this work only considers sink marks.

Sink marks are localized indentations in the surface of the plastic part which are normally caused by material shrinkage at localized significant changes of wall thickness, such as ribs or screw bosses at the back side of the part [2, 53, 67, 73, 98]. During injection, the polymer melt fills the mold cavity. Despite the possibility of flow irregularities (melt fracture, wall slip, jetting), the flow is assumed as laminar, because Re-numbers $\geqslant 2.300$ are usually not reached due to the the high viscosity of the melt. In this case, the melt stays in contact with cavity walls adjacent to the melt flow. Due to cooling caused by the mold, the layer of the melt which is in contact with the wall forms the solid peripheral layer (frozen layer) which becomes the surface of the manufactured part. The inside of the part still consists of liquid melt at this stage. At wall regions which intersect with structures at the back side of the part such as ribs or bosses, polymer melt is accumulated. This means that more polymeric material has to be cooled at such regions in comparison to their surroundings which causes more volumetric shrinkage at these regions. In Figure 2.3 the cross section of wall intersecting with a boss (filled) is sketched. The accumulated mass of the polymer melt leads to stronger volumetric shrinkage in the surroundings. Therefore, the peripheral layer is pulled inwards which causes the formation of a sink mark.

Sink marks can be prevented either by smart part design or by choosing suitable settings of process parameter such as injection and holding pressure, holding pressure time and temperatures of melt and mold. Smart part design is characterized by constant wall thickness, thin structural elements compared to wall thickness, and short distance of the structures to the gate. Process settings which reduce the formation of sink marks are high injection and holding pressure, a long holding pressure time and low melt and mold temperatures. [17, 67, 98]

2.2.3 *Visibility of Sink Marks*

Besides strategies to prevent the formation of sink marks itself, there exist strategies to conceal sink marks. The visual perceptibility of sink marks

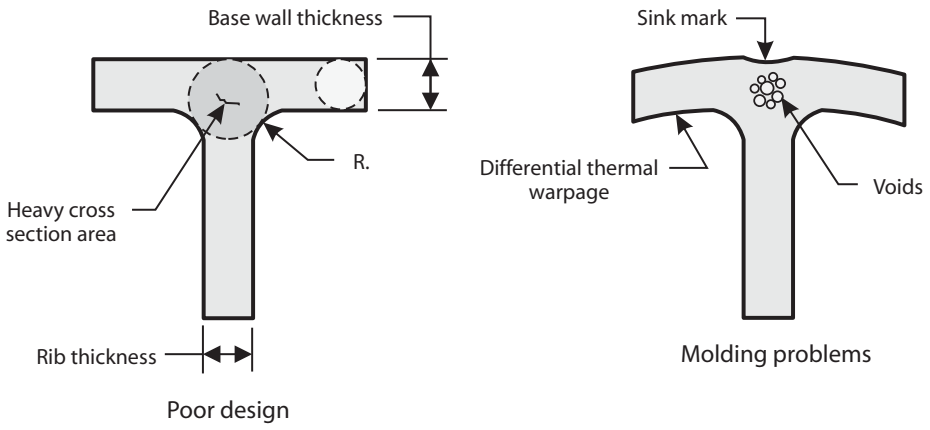

(a)

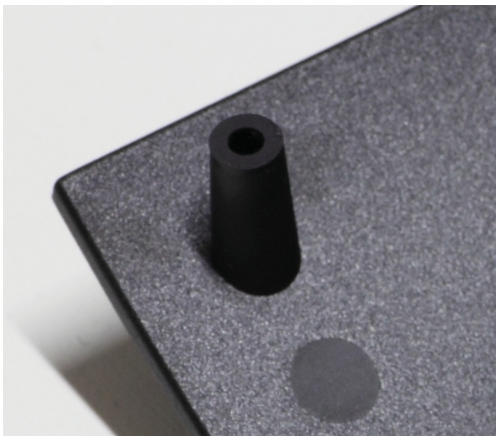

(b)

Figure 2.3: a) Wall section intersecting with a rib before material shrinkage (left) and after material shrinkage with formation of a sink mark (right) [17]. b) Image of a wall-boss-intersection

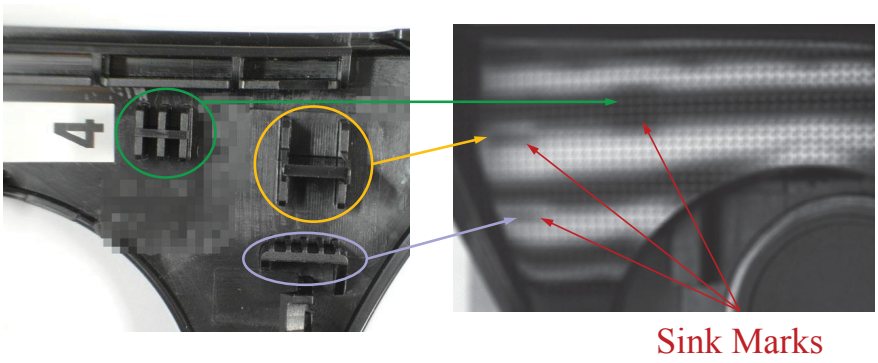

Figure 2.4: Influence of sink marks on the reflection from a high-gloss surface. Left: Picture of the structures, which cause the sink marks, at the back side of the plastic part. Right: The light pattern which is reflected from the high-gloss front side of the plastic part is distorted by the sink marks.

depends on various factors such as surface structure, gloss and color [53, 102]. A common method for concealing sink marks is the application of structure to the plastic part's surface. However, the surface of the part has to be smooth or even high-gloss in most high quality applications. In such cases, only the strategies which were mentioned in Section 2.2.2 can be applied to reduce the perceptibility of sink marks.

The success of concealing the sink marks has to be evaluated by quality inspection. In previous works, methods were introduced which evaluated the visual perceptibility of sink marks on smooth, diffusely reflecting surfaces [42, 43]. Gruber et al. used grazing light illumination during their measurement to obtain information about the shading properties of surface and especially sink marks. Gaussian and Gaussian-like functions were used for the fit of linearly and point-shaped sink mark intensity in measurement images. The fitted data was then differentiated twice to calculate the amplitude of the second derivative from the difference of maximum and minimum value of the second derivative in the respective sink mark. The resulting value was used as a feature parameter for sink mark perceptibility. When necessary, the second derivative of the measurement was fitted with a polynomial function to subtract overall shape warpage of the plastic part beforehand. The introduced methods allow the reproducible measurement of sink mark perceptibility on diffusely reflecting surfaces.

Sink marks on high-gloss surfaces on the other hand are detected visually from localized distortions in the reflections from the surface. Figure 2.4 displays the effect of sink marks on the reflection of a light pattern from the surface of a high-gloss part. The sink marks distort the pattern, which makes them clearly visible.

Hayden carried out several assessment studies and showed that the perceptibility is mainly dependent on the localized curvature of sink marks as well as the area of sink mark indentation [53]. Based on these results, the model which is introduced in Section 3.5.4 has been developed. The measurement of the curvature is introduced in Section 2.3.6.

2.3 PHASE MEASURING DEFLECTOMETRY

2.3.1 *Why Deflectometry?*

Specularly reflecting surfaces still pose a problem for machine vision. The reflection of the surroundings in such surfaces can be many orders of magnitude brighter than the texture of the surface. The surface is outshone by the reflections and therefore becomes virtually invisible. The best example is a bathroom mirror. The reflection of the bathroom and of a possible observer outshines the surface of the mirror. If the surface of the mirror is clean enough, it looks transparent to the observer. Therefore, specularly reflecting surfaces cannot be inspected in a direct way. However, it is possible to draw inferences from the reflections about the shape of such a surface. Topographically evident defects such as sink marks cause local distortions of the surface reflection. This in turn becomes apparent in the normal vector field of the surface.

Therefore, specular surfaces can be inspected indirectly by evaluating the reflections of the surrounding scene. The evaluation of the reflections becomes efficient when prior knowledge about the reflected objects is available in advance. For this reason, it is convenient to use light patterns which are generated by a diffuse structured light source for most deflectometric measurements. Accordingly, information about the light flux from the light source to the camera via the inspected surface is usually stored in such patterns. Using the proportionality of the distances between light source, sample and camera and the deflection of the light rays, deflectometric methods are sensitive to even small defects. Assuming that the distances between the components of a deflectometric testing site are large enough, it is possible to measure surface defects down to the sub-micron range. In Section 2.3.3 coding methods are discussed.

As mentioned before, the deflectometric measurement is dependent on the law of reflection and therefore on the normal vector field of the surface. In other words, the deflectometric measurement contains information about the first derivative of the surface which is obtained in a direct way. This is advantageous for quality inspection of specularly reflecting surfaces, since human defect perception is closely related to the curvature of a surface which can be calculated from the second derivative of

the surface using only one differentiation. This reduces the probability to lose information in the noise floor due to a comparatively high signal to noise ratio. In Figure 2.5 the correlation between curvature and the perceptibility of defects is sketched.

The deflectometric measurement feature several advantages for quality inspection of specularly reflecting surfaces:

1. Robust measurement: If stray light is kept to a minimum, the measurement is robust due to knowledge of the light rays because of the coding of the structured light source. Methods for coding will be introduced in Section 2.3.3.
2. High accuracy: Since even slight changes of the surface have a huge influence on the path of the reflected light rays, even tiny defects of the surface can be detected with the measurement.
3. High signal-to-noise ratio
4. Reliable detection of especially localized defects with distinct curvature.

The following sections will introduce the basic concepts behind phase measuring deflectometry.

2.3.2 *Mapping Function*

The basic deflectometric measurement setup consists of a screen which provides a structured light source, a highly reflective surface sample and a camera. Accordingly, the sample can be considered to be part of the optical setup. The camera is not focused on the surface of the sample but on the image of the light source reflected by the surface, because the reflection of the screen contains the information which is required for the deflectometric measurement. However, the resolution of surface features is decreased due to defocusing. In Section 2.3.3 a coding method is introduced which allows to position the focus plane of the camera between surface and reflection which facilitates better resolution of the surfaces without considerably decreasing the resolution of the reflection.

The evaluation of the sample's influence on the reflection is accomplished by tracing the paths of the light rays from the light source to the camera sensor. In this work, deflectometric measurements are carried out without prior calibration of screen and camera position. Additionally, there is no prior knowledge of the sample's position relative to screen and camera. Therefore, only the starting and end points of the light rays can

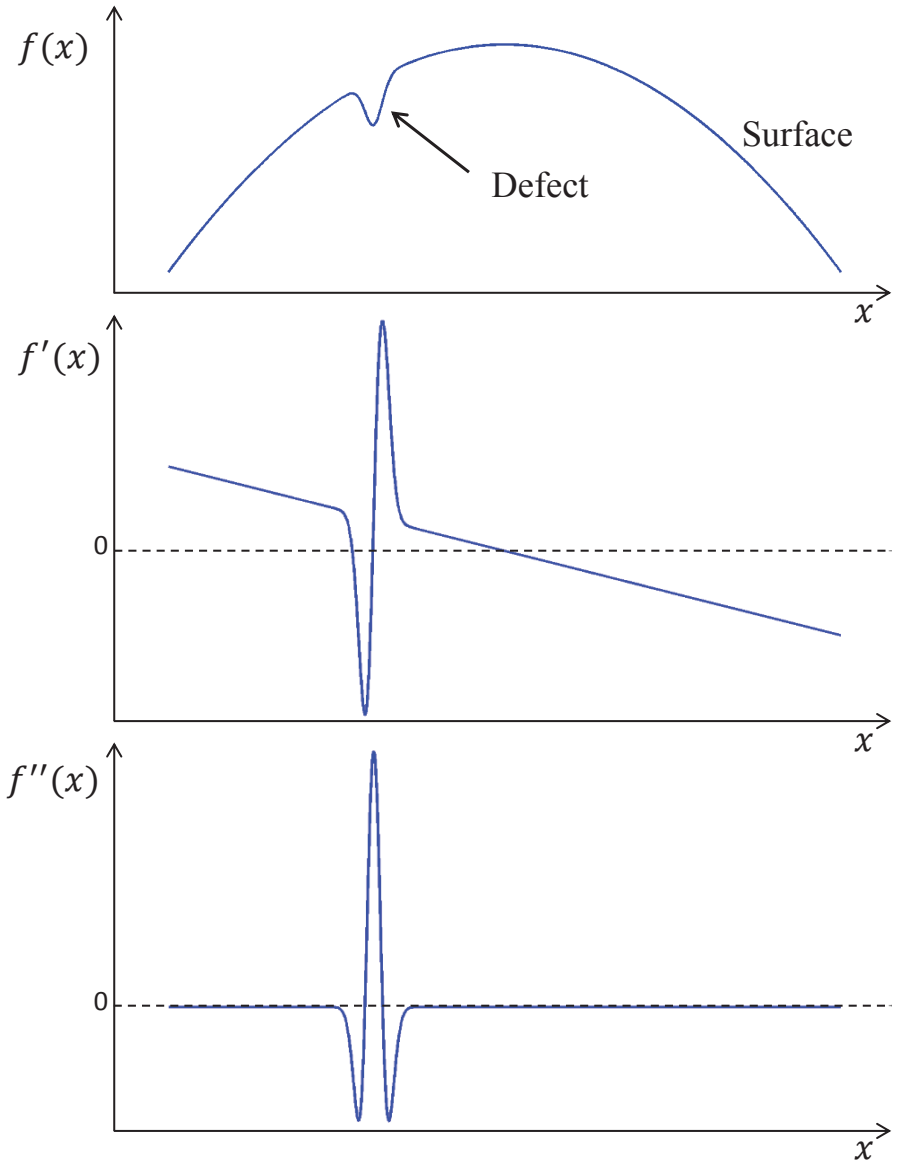

Figure 2.5: The visual perceptibility of surface defects is correlated with the curvature (second derivative) of the surface.

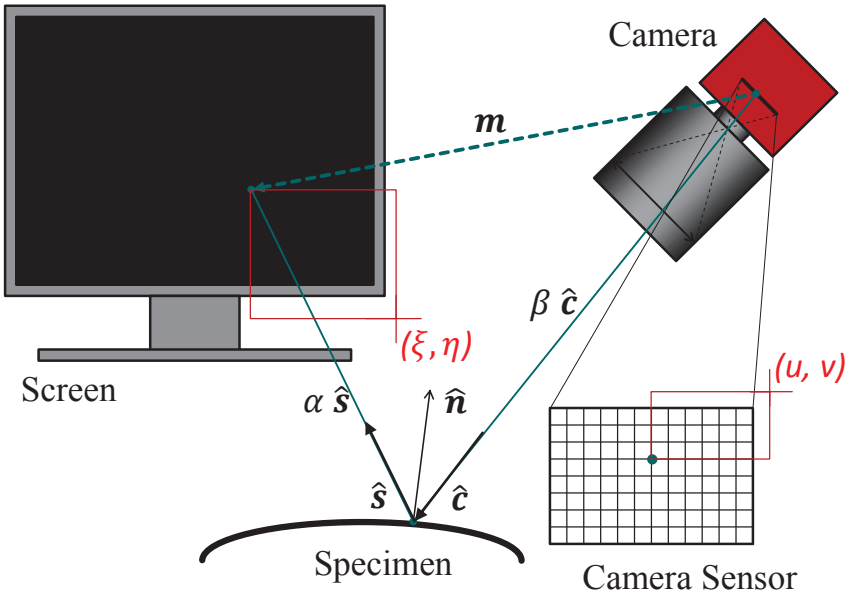

Figure 2.6: Sketch of the relation between screen and camera sensor coordinates which is described with the mapping function m. The camera is pictured with the simplest camera model, the pinhole camera.

be uniquely related to each other. However, this relation is sufficient for defect detection, since it contains unique information about the curvature of the inspected surface as will be shown latter in this section.

It is convenient to use LCD-screens and CCD-cameras for deflectometric measurements because the starting and end points of the respective light rays can be expressed in the intrinsic pixel coordinate systems of screen and camera. Figure 2.6 shows how screen pixel coordinates (ξ, η) are related to the camera pixels (i, j). The function m maps screen pixel coordinates (start points of light paths) to camera pixel coordinates (end points of light paths) [69, 72, 104]. Therefore, this function will be referred to as *mapping function*.

m is calculated from the viewing direction of a single camera sensor pixel $\hat{c}$ and its reflection onto the screen $\hat{s}$ (inversion of ray path)[3]

$$m = \alpha \hat{s} + \beta \hat{c}. \tag{2.24}$$

The law of reflection relates the directions $\hat{c}$ and $\hat{s}$ to the unit normal vector of the reflecting surface point $\hat{n}$.

[3] $\hat{c}$ and $\hat{s}$ are unit vectors.

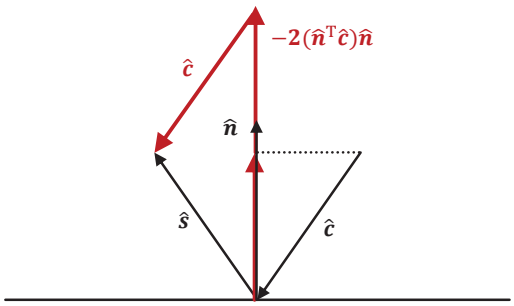

Figure 2.7: Graphical expression of the Law of Reflection.

As can be seen in Figure 2.7, the vector $\hat{s}$ can be expressed by the normal vector $\hat{n}$ and the viewing direction $\hat{c}$:

$$\hat{s} = \hat{c} - 2\left(\hat{n}^T\hat{c}\right)\hat{n}. \tag{2.25}$$

Application of Equation 2.25 on Equation 2.24 gives rise to

$$m = (\alpha+\beta)\hat{c} - 2\alpha\left(\hat{n}^T\hat{c}\right)\hat{n}. \tag{2.26}$$

The explicit calculation of $\hat{n}$ from Equation 2.26 leads to

$$\hat{n} = \frac{(\alpha+\beta)\hat{c} - m}{2\alpha(\hat{n}^T\hat{c})}. \tag{2.27}$$

Application of Equation 2.25 and Equation 2.27 on the vectorized law of reflection

$$\hat{n} = \frac{\hat{s}-\hat{c}}{\|\hat{s}-\hat{c}\|} \tag{2.28}$$

finally results in

$$\hat{n} = \frac{\frac{m}{\alpha} - \left(1+\frac{\beta}{\alpha}\right)\hat{c}}{\left\|\frac{m}{\beta} - \left(1+\frac{\alpha}{\beta}\right)\hat{c}\right\|}. \tag{2.29}$$

Equation 2.29 can be analytically solved if screen and camera position are known. However, given that the distances of camera and monitor to the measured sample are sufficiently large, calibration of camera

and screen position is not necessary. In this case, two approximations are valid:

1. The camera sensor is small compared to the distance between camera and sample and is considered as a point ($\beta = \text{const.}$, $\hat{c} = \text{const.}$)

2. All screen pixels are approximately equally distanced to the sample, given that the distance between screen and sample is sufficiently large ($\alpha = \text{const.}$). In other words, if the distance between screen and sample is large enough, the deviations between the flat screen and the surface of a sphere with radius α and the sample as center are small.

As a result, the second term in Equation 2.29 becomes constant for the whole measurement which means that the derivative of the mapping function is proportional to the directional curvatures of the sample's surface [69, 72, 104]. Consequently, calibration of the deflectometric setup is only necessary for metrological reconstruction of the sample's surface and for comparison of measurements with different viewing directions $\hat{c}$ of the respective cameras.

2.3.3 *Coding of the Light Source*

A very intuitive way of coding the pixel coordinates of the screen would be to switch each pixel on and off while taking a picture each time. Since this approach is of course not practical, several coding methods for the measurement and calculation of the mapping function have been developed. Binary coding methods, gray code imaging for example, considerably result in a low number of required images and achieve sub-pixel accuracy [33, 34, 121]. However, these methods require the exact recognition of each fringe of the structured light patterns in most cases, which makes them susceptible to image blurring due to low distinctness of image of the surface or defocusing of the camera from the reflected images of the patterns. Another possibility are phase shifting algorithms. For example in interferometry, phase shifting algorithms are used to estimate the phase information Θ, which is linearly proportional to a demanded distance (from an object or height of a surface), of an aperiodic signal with time dependent phase shift $\Phi(t)$ which can be expressed by [35]

$$g(\Theta, t) = A\ [1 + C\ \cos(\Theta + \Phi(t))] \tag{2.30}$$

where A denotes the amplitude and C the contrast of the signal. The Fourier Transformation of the signal $g(\Theta, \nu)$ at its modulation frequency ν_0 is given by

$$G(\Theta, \nu_0) = \frac{1}{2} A\, C\, W(0)\, \exp(i\,\Theta) \tag{2.31}$$

where W denotes the Fourier Transformation of a window function w, for example the rectangular confinement of a screen. Then the phase information Θ is calculated as the argument of $(G)(\Theta, \nu_0)$ using

$$\Theta = \arctan\left[\frac{\Im\{G(\Theta, \nu_0)\}}{\Re\{G(\Theta, \nu_0)\}}\right] \tag{2.32}$$

It is possible to apply a phase-shifting algorithm for encoding the screen pixel coordinates by approximation of the time dependency of the phase shift with a periodic sequence of phase-shifted sinusoidal patterns Φ_j [35, 60][4].

$$G(\Theta, \nu_0) = \sum_{j}^{N-1} g_j(\Theta, \Phi_j) w_j \exp(i\,\Phi_j) \quad j = \{0, \ldots, N-1\} \tag{2.33}$$

Since image blur can be described mathematically as a low-pass-characteristic, the application of sinusoidal patterns instead of definitely structured fringe patterns facilitates a more reliable measurement of the surface. Such patterns are defined by only one single low frequency. Therefore, the low-pass characteristics of the measurement setup, which is due to the reflection characteristics of the surface and the imaging characteristics of the camera, do not change the phase, but only decrease the contrast of the pattern [5, 69, 72]. The periodic length of the pattern as well as the dimensions and pixel numbers of the screen are known well. Therefore, the phase information Θ is directly related to the screen pixel coordinates by

$$\xi = \frac{L}{2\pi} \Theta \tag{2.34}$$

[4]For the sake of completeness, the comprehensive derivation for the phase shifting algorithm based on this approach is given in the appendix.

where ξ denotes one dimension of the screen pixel coordinates and L is the length of the screen along the same dimension. The sequence of patterns p_j is generated by using

$$p_j(\xi,\eta) = A_p \left[1 + C_p \cos\left(\frac{2\pi}{L}\xi + \Phi_j\right)\right] \quad j = \{0,\ldots,N-1\} \tag{2.35}$$

where η is the second screen pixel coordinate, A_p is the amplitude and C_p is the contrast of the patterns. Φ_j denotes the phase shifts which are applied to the sinusoidal progression of N patterns. For a phase shifting algorithm used in deflectometry, phase shifts are applied which monotonously increase in constant increments. The patterns are reflected from the surface of a sample into the camera which generates an intensity matrix g_j (the measurement image) for each pattern p_j. These measurement images include the information about the screen coordinates encoded as phase information and the light path from screen to camera. Therefore, application of the mapping function m_l in Equation 2.35 leads to the intensity matrices of the measurement images $g_j(u,v)$

$$g_j(u,v) = A_g \left[1 + C_g \cos\left(\frac{2\pi}{L} m_l(u,v) + \Phi_j\right)\right] \tag{2.36}$$

where (u,v) are the camera pixel coordinates while A_g and C_g denote the amplitude and the contrast, respectively, of the patterns in the image. In this case, m_l codes only one coordinate direction (either u or v) for screen and camera.

The mapping function, which is encoded as phase information of this pattern sequence, is calculated from the application of Equation 2.36 on Equation 2.33 and then by application of Equation 2.32:

$$m_l(u,v) = \frac{L}{2\pi} \arctan\left[\frac{\sum_j g_j(u,v)\sin(\Phi_j)}{\sum_j g_j(u,v)\cos(\Phi_j)}\right] \tag{2.37}$$

As mentioned before, the window functions w_j relate to the dimensions of the screen. Therefore, the weights of the window functions are assumed to be either 0 or 1.

Equation 2.37 is a general formula for the development of phase shifting algorithms. Accordingly, the explicit formulation depends on the number of patterns and the phase shift increment which is used for their generation. However, the development and comparison of phase shifting

algorithms is outside the scope of this work. Several reviews exist in literature which list and evaluate important phase shifting algorithms (e.g. [46, 56, 57]).

In this work, the 4-Bucket-Algorithm [82]

$$m_l(u,v) = \frac{L}{2\pi} \arctan\left[\frac{g_3 - g_1}{g_0 - g_2}\right] \quad \text{with} \quad \Phi_j = \left\{0, \frac{\pi}{2}, \pi, \frac{3\pi}{2}\right\}, \tag{2.38}$$

which fulfils the conditions for the derivation of Equation 2.37, was chosen for the evaluation of the deflectometric measurements. This algorithm allows for a fast numerical calculation and features comparatively low phase noise while it requires a comparatively low amount of measurement images [46]. For each direction of screen coordinates, four images of phase shifted patterns are evaluated according to Equation 2.38. These properties make the 4-Bucket-Algorithm suitable for an in-line application of a deflectometric setup for quality inspection of injection molded parts. In the following figures, examples of measured and processed images for the deflectometric algorithms are desplayed. An injection molded part which features a comparatively simpe shape is used in many of these examples for this reason and is introduced in Figure 2.8.

Figure 2.9 displays an example for the calculation of the mapping function from four images with different phase shift of the patterns. Since only the surface reflects the patterns into the camera, only the surface features applicable information about the phase function while other regions of the measurement image feature phase noise.

2.3.4 *Masking of the Phase Information*

The relative positions of camera and screen, as well as the shape of the inspected surface, may cause measurement images which contain no useful information but only noise in some regions. These regions can be dismissed using the modulus of the Fourier transformed phase information. $\mathcal{I}$ forms a measure for the intensity of the phase information in the images [71]

$$\mathcal{I}(u,v) = \sqrt{\left[\sum_{j=0}^{N-1} g_j(u,v)\ \sin(\Phi_j)\right]^2 + \left[\sum_{j=0}^{N-1} g_j(u,v)\ \cos(\Phi_j)\right]^2}. \tag{2.39}$$

This approach is convenient, since no additional images are necessary for the calculation of $\mathcal{I}$. The elements of $\mathcal{I}$ are high for sections in the

(a)

(b)

Figure 2.8: a) Front side of the injection molded part which is used in most examples of measured and processed images for the deflectometric algorithms due to its comparatively simple shape. b) Back side of the injection molded part. The positioning pins at the corners of the part, as well as the thickened edges of the part cause sink marks in case of unfavorable process parameters.

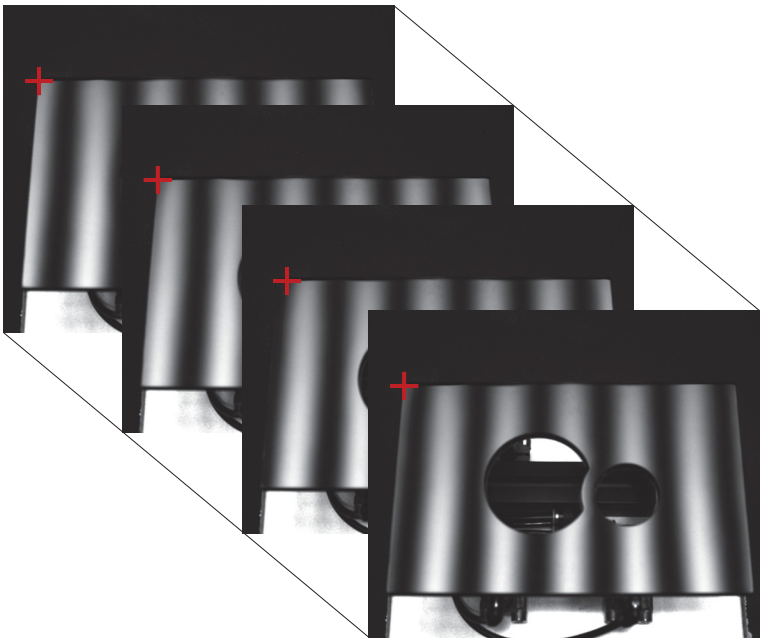

(a)

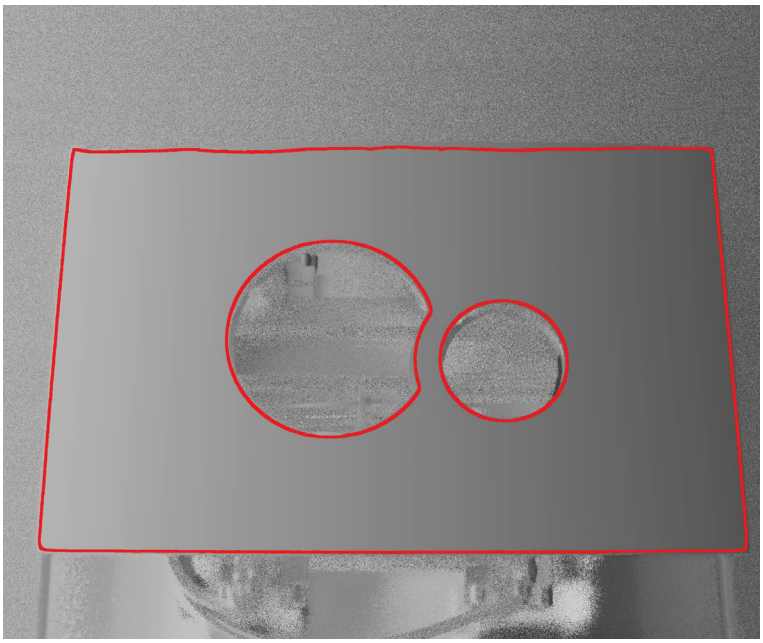

(b)

Figure 2.9: a) 4-Bucket-Algorithm: Four images with different phase shifts of the pattern (see mark in the upper left corner of the part in each image), b) Phase information Θ of the mapping function m.

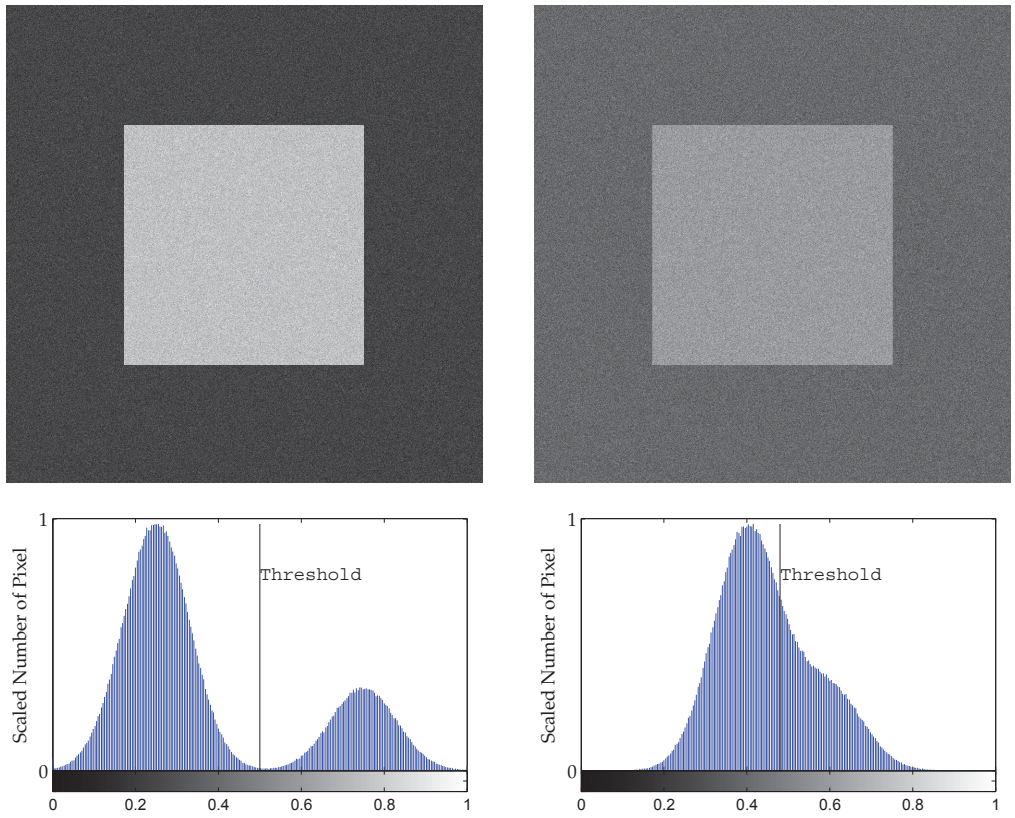

(a) (b)

Figure 2.10: Automatic calculation of a suitable threshold for image segmentation [85]: a) Bimodal distribution of pixel intensities, b) unimodal distribution of pixel intensities and the respective histograms.

measurement images where the phase information is distinctive, while sections where the intensity is nearly constant in all measurement images feature low values of $\mathcal{I}$. The binary black and white map for the segmentation of the image sections is formed according to the values of $\mathcal{I}$. The threshold was found by application of the method of Ng [85] which is an improved method to the method of Otsu [99]. An example for the calculation of the automatic threshold is displayed in Figure 2.10. With Otsu's method, a histogram of image gray values is analyzed with statistic methods to find the optimal threshold value for the discrimination of two distinct gray value distributions in a bimodal histogram. The improvement of the method of Ng consists in the option to calculate the optimal threshold value for a unimodal distribution in a histogram. This enables automatic and computationally cheap segmentation of low-contrast intensity images. In Figure 2.11 an example for the evaluation of the intensity of phase information in the measurement images is displayed.

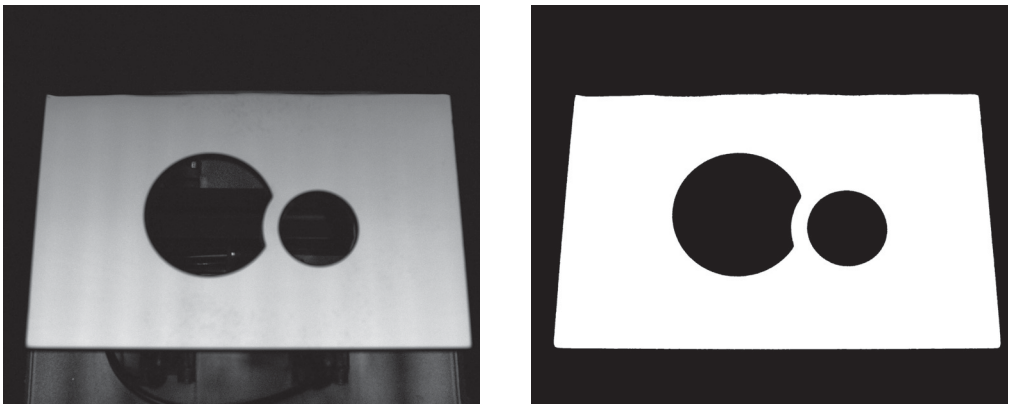

(a) (b)

Figure 2.11: Example for the segmentation of measurement results according to the distinctness of the phase information. a) displays the intensity function $\mathcal{I}$ of the fused images and b) the mask for segmentation of the measurement, which an automatically generated threshold was used for.

2.3.5 *Phase Unwrapping*

In a basic version of the deflectometric measurement, the periodic lengths of the generated patterns are equal to the respective dimension of the screen. However, the properties of screen and camera limit the resolution of the deflectometric measurement, since they possess a limited number of discrete gray levels and pixels. In Figure 2.12 this relation is displayed for one-dimensional signals where the achieved resolution for the abscissa of the diagram which relates to time or space resolution is limited by the discrete levels of the signal generator. A higher frequency provides a higher resolution of the signal's abscissa. However, the arcus tangents function in Equation 2.38 which is used for the calculation of the mapping function is unambiguously defined in the interval $[-\pi, \pi]$ only. Therefore, the measurement loses its one-to-one relation between phase information Θ and mapping function m if sinusoidal patterns are applied with periodic lengths smaller than the dimensions of the screen.

This problem, which is commonly known as phase unwrapping problem, is addressed by several approaches. For example, the Chinese remainder theorem is used to unwrap the phase information with two phase images which are generated using patterns with coprime periodic lengths [66, 124]. Another example is the application of binary coding algorithms. The combination of a phase shifting algorithm together with for example a gray code projection on the surface allows to unwrap the phase with the accuracy of deflectometry together with the robustness of gray codes [108].

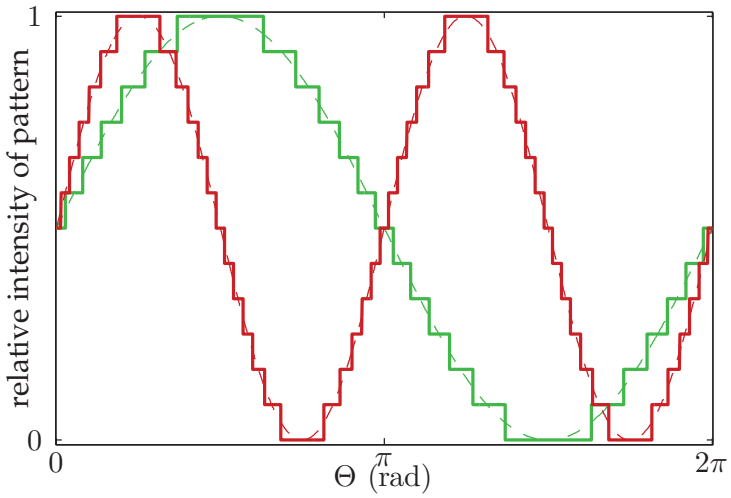

Figure 2.12: Comparison of the ambiguity of phase information Θ at limited gray levels for a low frequency signal (green) and a high frequency signal (red).

However, a more reliable and numerically less expensive way to unwrap the phase information is to iteratively apply the 4-Bucket-algorithm for sinusoidal patterns with decreasing periodic lengths. In the first stage of the measurement, the used sinusoidal patterns feature periodic lengths which are equal to the dimensions of the screen. The resulting measurement is a rough estimate of the phase information without any phase jumps. In the next stage, periodic patterns with periodic length of only a fraction of the screen dimensions are used for the measurement. This results in ambiguous but better resolved phase information. The phase information is unwrapped by comparing the ambiguous phase information with the initial unique phase information. This process can be repeated with sinusoidal patterns with decreasing periodic lengths until the demanded resolution is achieved.

A practical approach is to decrease the periodic length by factor 2 each iteration. Since the respective results pass through the image set $[-\pi, \pi]$ of the arcus tangents function within one periodic length of the respective pattern, the slope of the new phase information is increased by factor 2, compared to the slope of the phase information of the prior iteration (see Figure 2.13). This allows a very easy and straight forward phase unwrapping with

$$k(u,v) = \text{round}\left[\frac{2\,\Theta_{n-1}(u,v) - \Theta_n^*(u,v)}{2\,\pi}\right] \tag{2.40}$$

and

$$\Theta_n(u,v) = \Theta_n^*(u,v) + 2\pi k(u,v) \tag{2.41}$$

where Θ_{n-1} is the phase unwrapped phase information of the prior iteration and Θ_n^* is the wrapped phase information which is wrapped and therefore still features phase jumps. This numerically fast algorithm works for adequately smooth surfaces which can be differentiated at least twice[5]. Singular behavior of the surface like edges or nooks could prevent this algorithm from proper functioning. Since the method used in this work is based on the measurement and calculation of the curvature of surfaces which relates to the second derivatives of the surfaces, the required differentiability of the measured surfaces already restrains the surface classes which can be measured with this method. The surface classes which are suitable for deflectometric measurement and curvature evaluation are also suitable for the algorithm which was introduced in Equation 2.40 and Equation 2.41. The conversion of the phase information into screen coordinates can again be carried out by application of Equation 2.34.

2.3.6 *Calculation of Curvature Parameters from Measurement*

In Section 1.3 and Section 2.3.1 the correlation between the curvature of a surface and the perceptibility of surface defects for human observers was suggested. Phase measuring deflectometry is suitable for an approximated evaluation of perceptibility of surface defects, since its measurement results already contain information about the normal vector field, which is equitable to the first derivatives of the surfaces in direction of the camera sensor's pixel coordinates (u, v). The calculation of the principal curvatures from the measurement results and fundamental derivations of differential geometry are introduced in this section (also see Farin [30] and Bär [7]).

As mentioned in Section 2.3.5, in this work only surfaces of the category $\mathcal{C}^2$ are considered for deflectometric measurements in this work. These category of surfaces satisfies the conditions for the mathematical conventions introduced in this section.

[5] In this case "smooth" refers to the mathematical expression for a differentiable function. The mathematical symbol for the class of functions which can be differentiated twice is usually $\mathcal{C}^2$.

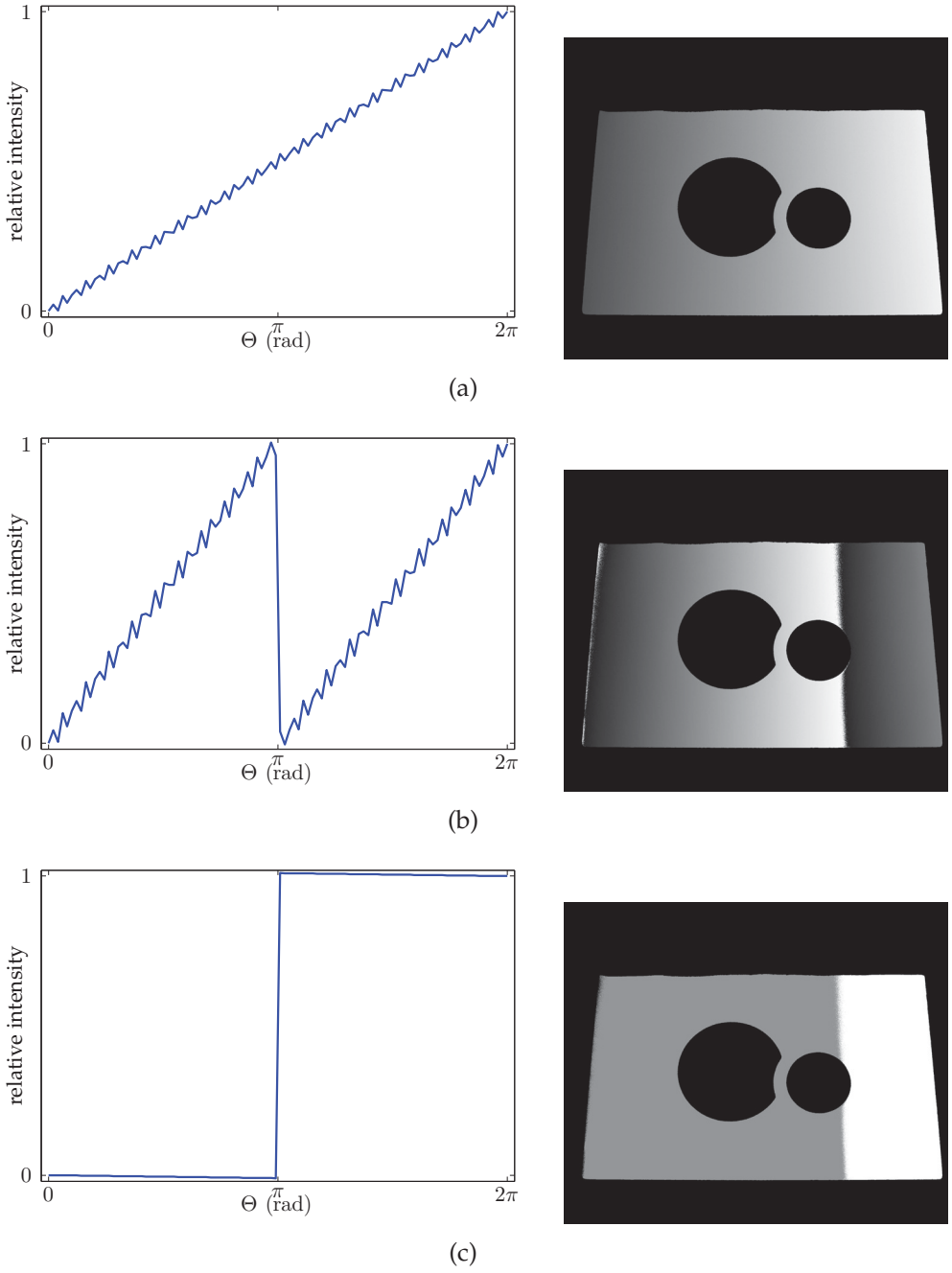

Figure 2.13: Graphs and examples of a) rough phase information without ambiguities and b) phase information with better resolution but ambiguities. Subtraction of the two phase information graphs according to Equation 2.40 gives c) a step function where the phase jumps are easily discernable.

Regular surfaces can be defined in their parametric form

$$f(u) = \begin{pmatrix} x(u) \\ y(u) \\ z(u) \end{pmatrix} \quad \text{with} \quad u = \begin{pmatrix} p \\ q \end{pmatrix} \tag{2.42}$$

where x, y and z are differentiable functions with respect to the parameters p and q. An arbitrary curve $u(t)$ in the parametric p,q-plane defines a regular curve on the surface $f(u)$ where its arc length is calculated from its parametric form

$$s(t) = \int_{t_0}^{t} \frac{\partial u(t)}{\partial t}\, dt \tag{2.43}$$

However, the calculation of the curvature of a regular surface $f(u)$ is dependent on the curve $u(t)$ which is considered for parametrization. Therefore, the curvature of regular surfaces is defined by the two principal curvatures κ_{max} and κ_{min} which define the maximal and minimal curvatures at a point on a surface. The calculation of the principal curvatures requires the introduction of the first fundamental form and the second fundamental form of classical differential geometry.

The first fundamental form of a surface $f(u)$ results from the squared differential of arc length ds of an arbitrary curvature $u(t)$ on the surface

$$\begin{aligned} I_F := \quad ds^2 &= \left\| \frac{\partial f(p,q)}{\partial t} \right\|^2 dt^2 = \\ &= \left[f_p^2 \left(\frac{dp}{dt} \right)^2 + 2\, f_p\, f_q \frac{dp}{dt} \frac{dq}{dt} + f_q^2 \left(\frac{dq}{dt} \right)^2 \right] dt^2 \end{aligned} \tag{2.44}$$

where f_p denotes the first derivative of $f(u)$ with respect to parameter p and f_q denotes the first derivative respect to parameter q. Equation 2.44 can be expressed in matrix form with

$$I_F := \quad ds^2 = du^T \begin{bmatrix} f_p^2 & f_p\, f_q \\ f_p\, f_q & f_q^2 \end{bmatrix} du = du^T\, G\, du \quad \text{with} \quad du = \begin{pmatrix} dp \\ dq \end{pmatrix} \tag{2.45}$$

where the matrix G is symmetric and possesses only three independent components. Additionally, it is required to be positive-definite. The first fundamental form I_F enables the calculation of lengths and areas on surfaces. The derivation of the second fundamental form of a surface $f(u)$ starts with the calculation of the curvature κ by differentiating a curve $u(t)$ on the surface $f(u)$ with respect to the arc length s

$$\frac{\partial^2 f(u)}{\partial s^2} = \kappa \hat{v} \tag{2.46}$$

where $\hat{v}$ is the unit normal vector of the curve u in direction of the curvature radius at surface point $x(u)$. Multiplication with the unit normal vector $\hat{n}$ of the surface $f(u)$ at point $x(u)$ gives

$$\kappa \hat{v}\hat{n} = \kappa \cos\theta \tag{2.47}$$

where θ is the angle between the normal vectors $\hat{v}$ and $\hat{n}$. Since the normal vector $\hat{n}$ of a point $x(u)$ is perpendicular to the tangential plane at this point ($\hat{n}f_p = \hat{n}f_q = 0$) which implies that, as an example for parameter p,

$$\frac{d}{dp}\left(\hat{n}f_p\right) = \hat{n}_p f_p + \hat{n}f_p p = 0, \tag{2.48}$$

Equation 2.46 transforms to

$$\kappa \cos\theta = \hat{n}f_{pp}\left(\frac{dp}{ds}\right)^2 + 2\,\hat{n}f_{pq}\frac{dp}{ds}\frac{dq}{ds} + \hat{n}f_{qq}\left(\frac{dq}{ds}\right)^2. \tag{2.49}$$

For the calculation of the second fundamental form Equation 2.49 is multiplied with the squared differential of the arc length ds. The second fundamental form is given in matrix form with

$$II_F := \kappa \cos\theta\, ds^2 = u^T \begin{pmatrix} \hat{n}f_{pp} & \hat{n}f_{pq} \\ \hat{n}f_{pq} & \hat{n}f_{qq} \end{pmatrix} u = u^T H\, u \tag{2.50}$$

The second fundamental form is dependent on the spatial position of the surface. It allows the computation of curvatures for any given direction du and angle θ.

For $\hat{v} \parallel \hat{n}$, which means $\theta = 0$, the curvature normal vector $\hat{v}$ of the considered curve is perpendicular to the tangential plane of the surface

in point $x(u)$. Then, the considered curve features the normal curvature κ_0. Equation 2.50 divided by Equation 2.45 gives for the normal curvature

$$\kappa_0 = \frac{II_F}{I_F} = \frac{u^T H u}{du^T G\, du} \tag{2.51}$$

which is independent of the arc length s. Nevertheless, the normal curvature κ_0 is dependent on the direction

$$\lambda = \frac{dq}{dp} = \tan\alpha \tag{2.52}$$

of the considered curve. Division by dp^2 and with Equation 2.52, Equation 2.51 gives

$$\kappa_0(\lambda) = \frac{\hat{n} f_{pp} + 2\lambda\, \hat{n} f_{pq} + \lambda^2\, \hat{n} f_{qq}}{f_p^2 + 2\lambda\, f_p f_q + \lambda^2\, f_q^2} \tag{2.53}$$

The extreme values of the normal curvature κ_0 are the principal curvatures κ_{max} and κ_{min}. The principal curvatures can also be calculated as the eigenvalues of the Weingarten matrix

$$W = G^{-1} H\,. \tag{2.54}$$

In this case, the Weingarten matrix W, which describes the linear transformation of a vector along the tangential plane, is a 2×2-matrix, since the parameter space is of type $\mathbb{R} \times \mathbb{R}$. The calculation of eigenvalues λ_i for 2×2-matrices can be derived from the trace

$$\mathrm{tr}\,(M_{2\times2}) = \lambda_1 + \lambda_2 \tag{2.55}$$

and the determinant

$$\det(M_{2\times2}) = \lambda_1\, \lambda_2 \tag{2.56}$$

with

$$\lambda_{1,2} = \frac{1}{2}\left[\mathrm{tr}\,(M_{2\times2}) \pm \sqrt{\mathrm{tr}\,(M_{2\times2})^2 - 4\,\det(M_{2\times2})}\right] \tag{2.57}$$

The Weingarten matrix W is approximated using the mapping function which results from the deflectometric measurements [69, 72]. The directional derivatives of the mapping function are combined into a vector k in the following way

$$k_m(u,v) = \begin{pmatrix} \operatorname{sgn}\left(\frac{\partial m_1(u,v)}{\partial u}\right) & \left|\frac{\partial m(u,v)}{\partial u}\right| \\ \operatorname{sgn}\left(\frac{\partial m_2(u,v)}{\partial v}\right) & \left|\frac{\partial m(u,v)}{\partial v}\right| \end{pmatrix} \tag{2.58}$$

where m is defined as $m = (m_1, m_2)^T$. m_1 and m_2 are the components of the total mapping function for the coordinate directions u and v, respectively. The usage of the sign function (sgn) in this way is only valid, if the coordinate systems of the camera sensor and the screen are only rotated up to 90° relative to each other [69, 72]. The vector k_m is used to calculate the approximation of the Weingarten matrix with

$$\hat{W} = \begin{bmatrix} \sum_{\mathcal{R}} k_{m_1}^2 & \sum_{\mathcal{R}} k_{m_1} k_{m_2} \\ \sum_{\mathcal{R}} k_{m_1} k_{m_2} & \sum_{\mathcal{R}} k_{m_2}^2 \end{bmatrix} \tag{2.59}$$

where $\mathcal{R}$ is a region around the respective coordinate pairs (u,v). The principal curvatures κ_{max} and κ_{min} can be calculated from this approximation using Equation 2.57. However, in this work the mean curvature

$$\kappa_{mean} = \frac{1}{2}\operatorname{tr}(\hat{W}) = \frac{\kappa_{max} + \kappa_{min}}{2} \tag{2.60}$$

is used for defect evaluation, since this parameter is independent to curvature direction and can therefore be used as a scalar parameter for surface curvature.

The next section introduces the formalism of polynomial base functions which were used for polynomial regression of the data. This formalism enables the robust numerical differentiation of data sets, which is necessary for the calculation of the k_m tensor in Equation 2.58.

2.4 DISCRETE POLYNOMIAL BASE FUNCTIONS

2.4.1 *Fundamentals of Polynomial Regression*

Since numerical differentiation increases the noise in measurements, effective smoothing or fitting of the data with minimal introduction of artifacts prior to differentiation is necessary to achieve reasonable results. O'Leary and Harker proposed an approach for data analysis where they used polynomials for data fitting and filtering [88, 91, 92, 94]. The algorithms were implemented in Matlab and published according to the BSD-Licence [50]. The applications for the algorithms range from solving constrained problems [48, 49, 90, 92] to signal processing [93]. In this work, the algorithms were mainly used for data smoothing and differentiation. For the sake of completeness, a short introduction to the theory behind the algorithms is given .

Beginning with the Vandermonde matrix V which is defined as

$$V = \begin{bmatrix} 1 & x_1 & \cdots & x_1^d \\ 1 & x_2 & \cdots & x_2^d \\ \vdots & \vdots & \cdots & \vdots \\ 1 & x_n & \cdots & x_n^d \end{bmatrix} \tag{2.61}$$

for n points x_i and degree of the polynomials d, any polynomial reconstruction $\tilde{y}$ of the data set y can be defined by right multiplication of V with a coefficient vector s in the following way

$$\tilde{y} = V s \tag{2.62}$$

The coefficients s which define any data set y for such a polynomial reconstruction can be computed by

$$s = \left(V^T V\right)^{-1} V^T y = V^+ y \tag{2.63}$$

which is the least-squares solution for the calculation of polynomial coffi-cients from data sets with non-orthonormal polynomial bases. The resid-

ual error r of the polynomial approximation of the data y is expressed as

$$r = (I - V V^{+})\, y \tag{2.64}$$

V^{+} indicates the pseudo-inverse to the normally non-invertible matrix V. If the matrix is invertible, its pseudo-inverse equals the normal inverse of the matrix. The expression of r is independent of the coefficient vector s for any polynomial base which was generated from the Vandermonde matrix V. In contrast, the magnitude of the residual error r is only dependent on the exactness of the numerical calculation of the expression $V V^{+}$. Since polynomial regression is independent of the basic polynomial set, Harker and O'Leary propose the usage of an orthonormal polynomial base, since they deem the generation of the base from the Vandermonde matrix as ill-conditioned for numerical calculation [88]. The generation of the polynomial base is executed with high numerical precision by application of the three-term recurrence relationship between the polynomials[6] [87, 88, 94]

$$b_n = \alpha\, (b_{n-1} \circ x) + B_{n-1}\, \beta \tag{2.65}$$

with

$$\alpha = \frac{1}{\| \{I - B B^{T}\}\, (b_{n-1} \circ x) \|_2} \tag{2.66}$$

$$\beta = -\alpha\, B_{n-1}^{T}\, (b_{n-1} \circ x) \tag{2.67}$$

The iteratively created orthonormal polynomials b_n are generated as column vectors and are concatenated in the matrix B in the following way

$$B_n = [b_0, b_1, \cdots, b_n] \tag{2.68}$$

The first two polynomials can be calculated comparatively easily with

[6] The operator in $(b_{n-1} \circ x)$, for example, refers to the Hadamard product of tensors.

$$b_0 = \frac{1}{\sqrt{N}} \left[1, 1, \cdots, 1\right]^T \tag{2.69}$$

$$b_1 = \frac{x - \bar{x}}{\|x - \bar{x}\|_2} \tag{2.70}$$

where x is the vector containing the x-coordinates of the nodes and N is the number of the nodes.

One of the main advantages of the application of an orthonormal polynomial base B is that its conjugate transpose B^T, which can be calculated with comparatively low computational load, equals its inverse matrix B^{-1} or its pseudo-inverse matrix B^+ if it is non-invertible. Substituting the orthonormal base B into Equation 2.63 gives

$$s = B^T y \tag{2.71}$$

for the calculation of the coefficients s [88, 91]. The estimated values for y can then be calculated with

$$\tilde{y} = B\, s = B\, B^T y \tag{2.72}$$

The residual error r approaches 0, if the maximum degree of the polynomials d_{max} corresponds to the relation

$$d_{max} = n - 1 \tag{2.73}$$

where n is the number of measurement points x_i. However, linear regression of the data is achieved if the maximum degree of the polynomial base functions is lower than the value of Equation 2.73. Then the data is approximated according to the least square solution (see also Equation 2.63). Higher variations of the signal such as noise are cut off by the maximum degree of the used polynomials, which allows for filtering and data smoothing.

If a two-dimensional data set Z is aligned with the x and y coordinate frames, its data values can be explicitly expressed as a function of x and y. In such a case, polynomial regression which is based on Equation 2.72

can be separately executed for x and y directions in the following way for polynomial degree d [88, 91]

$$\tilde{Z} = Y_{M\times(d+1)}\, Y^{T}_{M\times(d+1)}\, Z_{M\times N}\, X_{N\times(d+1)}\, X^{T}_{N\times(d+1)} \tag{2.74}$$

where Y denotes the matrix for polynomial regression along the y direction and X the matrix for polynomial regression along the x direction.

2.4.2 *Local Approximation*

The equations in the former section are expressions for global approximation of data sets where the polynomials are calculated for the whole data set. However, in many examples, global polynomial approximation will lead to Runge's phenomenon [91, 94, 107]. In such cases, local approximation, where the polynomials B are calculated for a support length l_s which is shorter than the number of data points n, can produce better results.

The polynomial expansion $B\,B^T$ is a $l_s \times l_s$ matrix because it is expanded on the support length l_s[7]. For local approximation, this matrix is extended to an $n \times n$ matrix S. This operator handles the first and last $(l_s - 1)/2$ points with the first and last $(l_s - 1)/2$ rows of the polynomial expansion $B\,B^T$. Thereby, the respective data point, which the polynomials are evaluated on, moves towards the border of the support at the edges. The central row of the polynomial expansion is used for the remaining core points of the data sets. Such an operator S ensures that the degree and support length of the polynomial expansion for data regression are constant throughout the whole data set (see Figure 2.15). Additionally, this operator is symmetric and therefore linear phase [95]. This means that in contrast to common Fourier low-pass filters such a filter matrix causes no distortion of the filtered signal but only a phase delay of the whole signal (no signal change). In Figure 2.14, the generation of such a local approximation operator S from the polynomial expansion $B\,B^T$ is displayed for $l_s = 5$ and $n = 9$.

The local approximation for two-dimensional arrays is calculated similar to Equation 2.74 with

$$\tilde{Z} = S_{M\times M}\, Z_{M\times N}\, S^{T}_{N\times N} \tag{2.75}$$

[7] Usually, the support length l_s of a polynomial expansion has to be odd.

$$\mathsf{B}\,\mathsf{B}^{\mathrm{T}} = \begin{bmatrix} \mathbf{x}_{11} & r_{12} & r_{13} & r_{14} & r_{15} \\ r_{21} & \mathbf{x}_{22} & r_{23} & r_{24} & r_{25} \\ c & c & \mathbf{x} & c & c \\ r_{41} & r_{42} & r_{43} & \mathbf{x}_{44} & r_{45} \\ r_{51} & r_{52} & r_{53} & r_{54} & \mathbf{x}_{55} \end{bmatrix}$$

(a)

$$\mathsf{S} = \begin{bmatrix} \mathbf{x}_{11} & r_{12} & r_{13} & r_{14} & r_{15} & 0 & 0 & 0 & 0 \\ r_{21} & \mathbf{x}_{22} & r_{23} & r_{24} & r_{25} & 0 & 0 & 0 & 0 \\ c & c & \mathbf{x} & c & c & 0 & 0 & 0 & 0 \\ 0 & c & c & \mathbf{x} & c & c & 0 & 0 & 0 \\ 0 & 0 & c & c & \mathbf{x} & c & c & 0 & 0 \\ 0 & 0 & 0 & c & c & \mathbf{x} & c & c & 0 \\ 0 & 0 & 0 & 0 & c & c & \mathbf{x} & c & c \\ 0 & 0 & 0 & 0 & r_{41} & r_{42} & r_{43} & \mathbf{x}_{44} & r_{45} \\ 0 & 0 & 0 & 0 & r_{51} & r_{52} & r_{53} & r_{54} & \mathbf{x}_{55} \end{bmatrix}$$

(b)

Figure 2.14: Example for the extension of (a) a 5×5 polynomial expansion $\mathsf{B}\,\mathsf{B}^{\mathrm{T}}$ to (b) a 9×9 local approximation operator S. The first two and the last two rows of the polynomial expansion are used for the two first and last points of a data set respectively. The remaining core points of the data set are evaluated with the central row of the polynomial expansion. The emphasized *x's* mark the points which the polynomial expansion with the support length of five points is evaluated on.

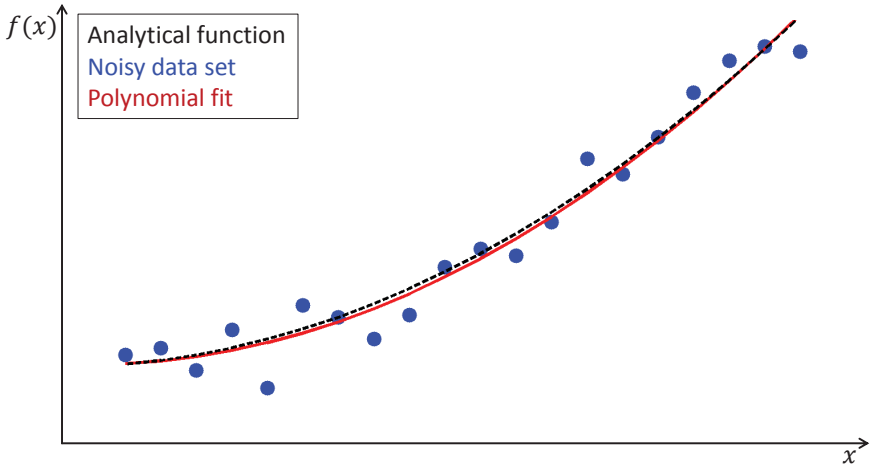

Figure 2.15: Smoothing of a noisy signal. An analytically generated signal (black) is superposed with normal distributed noise to generate artificial data points (blue dots). Polynomial regression ($d = 2$, $l_s = 5$) is used to smooth the data points (red).

where the operators S are usually extended from the same polynomial expansion to the respective dimensions of the data array Z. When the dimensions of the data sets are kept constant for all measurements, Equation 2.75 allows efficient filtering of the data. After the operators S are generated for the respective directions in the beginning, the data filtering is executed by comparatively simple and fast matrix multiplications.

2.4.3 *Polynomial Differentiation*

Conventionally, a tridiagonal matrix G, as sketched in Figure 2.16, is used for numerical differentiation, e. g. finite differences. The polynomial approximations of differentiation which are used for the generation of the operator are the first forward difference

$$f'(x_0) = \frac{f(x_0 + h) - f(x_0)}{h} + \mathcal{O}(h) \tag{2.76}$$

and the first backward difference, which is similar to Equation 2.76 except for differently signed terms, as well as the First Central Difference

$$f'(x_0) = \frac{f(x_0 + h) - f(x_0) - h}{2\,h} + \mathcal{O}(h^2) \tag{2.77}$$

Accordingly, the former approximations are used for the boundary of the data set (end points), while the center points of the data set are han-

$$G = \frac{1}{2h}\begin{bmatrix} -2 & 2 & 0 & 0 & 0 & \cdots & 0 \\ -1 & 0 & 1 & 0 & 0 & \cdots & 0 \\ 0 & -1 & 0 & 1 & 0 & \cdots & 0 \\ \vdots & \ddots & \ddots & \ddots & \ddots & \ddots & \vdots \\ 0 & \cdots & 0 & -1 & 0 & 1 & 0 \\ 0 & \cdots & 0 & 0 & -1 & 0 & 1 \\ 0 & \cdots & 0 & 0 & 0 & -2 & 2 \end{bmatrix}$$

Figure 2.16: Conventional gradient usually used for numerical differentiation, e.g. in finite differences applications. The first and last points are handled with the First Forward and First Backward Difference (see Equation 2.76), which is a two-point-approximation of degree one, while the center points are handled with the First Central Difference (Equation 2.77), which is three-point-approximation of degree two.

dled with the latter approximation. Since the first forward (backward) difference is a two-point approximation, it is of degree one. The first central difference as a three-point approximation is of degree two. Because of this inconsistency, the accuracy of numerical differentiation is reduced for the end points of the data set which, for example, makes the reconstruction of a curve from its differentials difficult [91].

However, reconstruction of data from gradients is beyond the scope of this work. The main concern with differentiation in this work is the adaptability of the support length l_s of the applied differential operator. It is preferable to adjust the differential operator according to the properties of the data from the measurements. The conventional differential operator G emphasizes the noise considerably because of the comparatively short support length of its polynomial expansions. Therefore, extensive data smoothing is necessary before the application of the operator. For this, see also Figure 2.17, where the artificial data set which is given in Figure 2.15 is numerically differentiated using the conventional differential operator G (blue line). The noise of the differentiated data without prior smoothing overlays the signal considerably.

As mentioned in Section 2.4.1, a longer support length of the polynomial expansion together with a low degree of the expanded polynomials facilitates data fitting and smoothing according to least-squares-solution. Such a differential operator also includes the data smoothing and is not as prone to noise as the conventional differential operator G. It is possible to generate an improved differential operator with the aforementioned adaptability and constancy of support length by differentiation of poly-

nomial expansions such as Lagrange Polynomials [16, 111] or Taylor Polynomial Expansion [76]. However, in this work the differential operators were generated with the orthonormal polynomials which were described in Section 2.4.1, since the differentials of the orthonormal polynomials can be generated with low additional computational load during generation using the derivative of Equation 2.65 given as [91]

$$\dot{b}_n = \alpha \left(\dot{b}_{n-1} \circ x + b_{n-1} \circ \dot{x} \right) + \dot{B}_{n-1} \beta \tag{2.78}$$

The polynomial differential operator D is calculated with

$$D = \dot{B} B^T \tag{2.79}$$

where B is a matrix with the orthonormal polynomials as column vectors while the differentials of the polynomials are concatenated as column vectors of $\dot{B}$. Local differentiation can be achieved with an extension of this operator similar to the extension of the polynomial expansion in Figure 2.14 [50, 92]. Two-dimensional data arrays can be differentiated with such local differentiation operators D for each direction x and y, respectively, in the following way

$$\frac{\partial Z}{\partial x} = Z_{M \times N} D^T_{N \times N} \quad \text{and} \quad \frac{\partial Z}{\partial y} = D_{M \times M} Z_{M \times N} \tag{2.80}$$

In this work, Equation 2.80 was used for the directional differentials of the deflectometric measurements which were used for the calculation of surface curvature. The support length of the operators was chosen according to the noise level of the measurements which was dependent on, for example, the clarity of the measured surface.

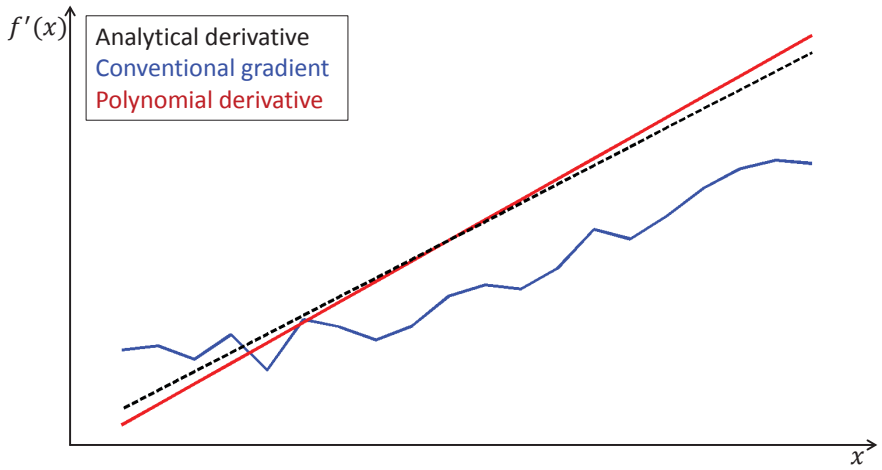

Figure 2.17: Example for numerical differentiation. The artificial data points of Figure 2.15 are differentiated using the conventional differentiation operator G (blue) and a local differentiation operator based on Equation 2.79 with $d = 2$ and $l_s = 5$ (red). The analytical differentiation of the generated function $f(x)$ is given for comparison (black). Since the conventional differentiation operator G is applied without prior smoothing, the differential of the signal is overlaid with considerably emphasized noise.

3

EXPERIMENTAL

3.1 LABORATORY SETUP OF THE DEFLECTOMETRIC TESTING SITE

In Section 2.3.2, a basic deflectometric setup was introduced. Its main components are a structured light source, in the given case an LCD-screen, a camera and the sample to be inspected. The mapping function, which describes how the screen is mapped onto the camera sensor via the surface of the sample, is determined by the deflectometric measurement. The reflections from high-gloss surfaces comply with the law of reflection, which results in that the mapping function contains information about the normal vector field of the sample's surface. The normal vector field on the other hand relates to the first derivative of the absolute surface geometry. This information is used to calculate the curvature of the inspected surface, which in turn can be used for sink mark detection.

The given task of this work was to extend this basic setup, which is only sufficient for the inspection of approximately plane surfaces, to enable total inspection of curved injection molded parts for sink marks. Accordingly, the setup should be still comparatively cheap while it does not implicate additional sources of hazards to personal or material. Additionally, models had to be found which calculated the perceptibility of possible sink marks for human observers from the results of the deflectometric measurements.

In this chapter, the strategies to achieve these tasks are explained on the basis of the laboratory testing site at the PCCL, which is displayed in Figure 3.1. In Table 3.1 the components which are used for the deflectometric measurement are listed. The screen for pattern generation during the deflectometric measurement is implemented as the secondary screen of the measurement PC, while the camera is connected to the PC via the GigE Vision interface standard. An off-the-shelf I/O-card type Agilent U2600A is used for communication between the measurement PC and the remaining electronic components of the testing site. This setup of a deflectometric measurement facilitates the semi-automatic inspection of curved injection molded parts which means that the parts are inserted manually into the mounting of the automatic positioning unit. Other components which can be seen on the testing site in Figure 3.1, such as additional cameras and light sources, are installed for the detection of morphological surface defects such as scratches, weld lines or tiger stripes on injection molded

Table 3.1: List of components of the deflectometric testing site at the PCCL laboratory

Component	Type Designation	
Frame	Bosch profile system	
1 Camera	ATV Prosilica 2450	Resolution: 2448×2250 pixels
1 Optical Lense	Fujinon HF25A-1/1.4	Focal length: 25 mm
1 Screen	Eizo FlexScan EV2333W	Resolution: 1920×1200 pixels
1 Photo resistor	Silonex NSL-5540	Temp. range: -60° to 75° C
1 Positioning Unit	Tilt: Thorlabs NR360S/M	Resolution: < 1 arcsec
	Azimuth: PiMicos DT-80R	Resolution: 0.225°
1 I/O-card	Agilent Agilent U2600A	
Software	Implemented in Matlab	

parts, which is also part of the PCCL project "Development of methods for the IN-LINE quality inspecton of freeform plastic surfaces aided by multi-axial robotic systems". These methods are applied parallel to the deflectometric measurements but are beyond the scope of this work.

The software for control and evaluation of the measurement and its results was implemented in Matlab. This language is an imperative language, which means that program execution happens sequentially. For this reason, the implementation of situation-dependent programs (e.g. automation applications) is often difficult in Matlab compared to object oriented languages such as C++. On the other hand, the advantage of this programming language lies in the efficient implementation of mathematical algorithms. Additionally, this language supports the implementation of vector-tensor-calculations with similar semantics as the algebraic formulas. For this reason, algorithms can be implemented fast with high readability.

The measurement sequence of the test setup is sketched in Figure 3.2. The representation of the process is simplified to increase readability of the figure by separating the single steps thematically. In the following

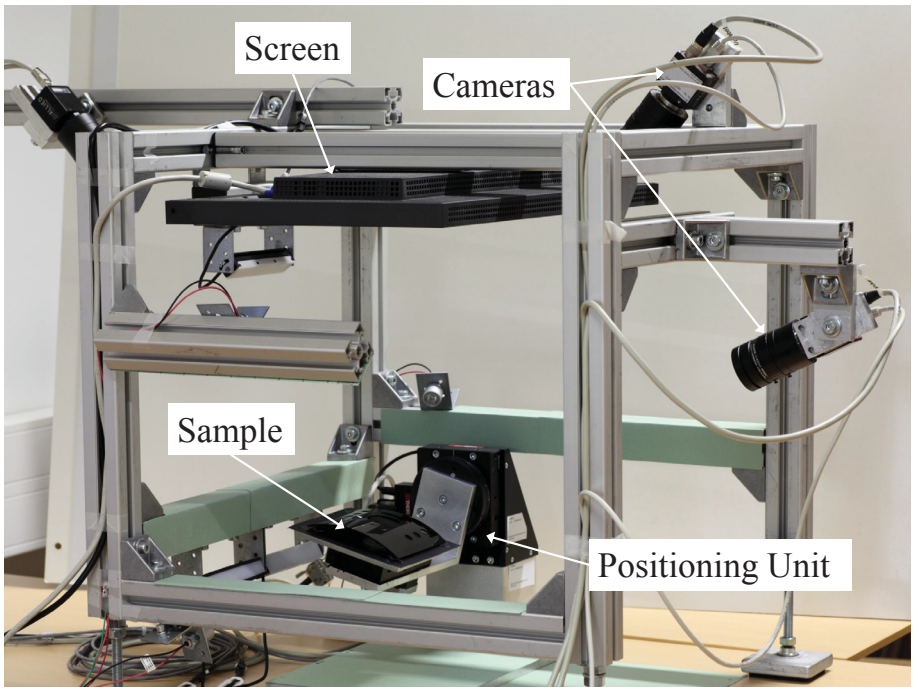

Figure 3.1: Image of the deflectometric testing site.

sections, the measurement sequence steps and the respective hardware will be described in detail.

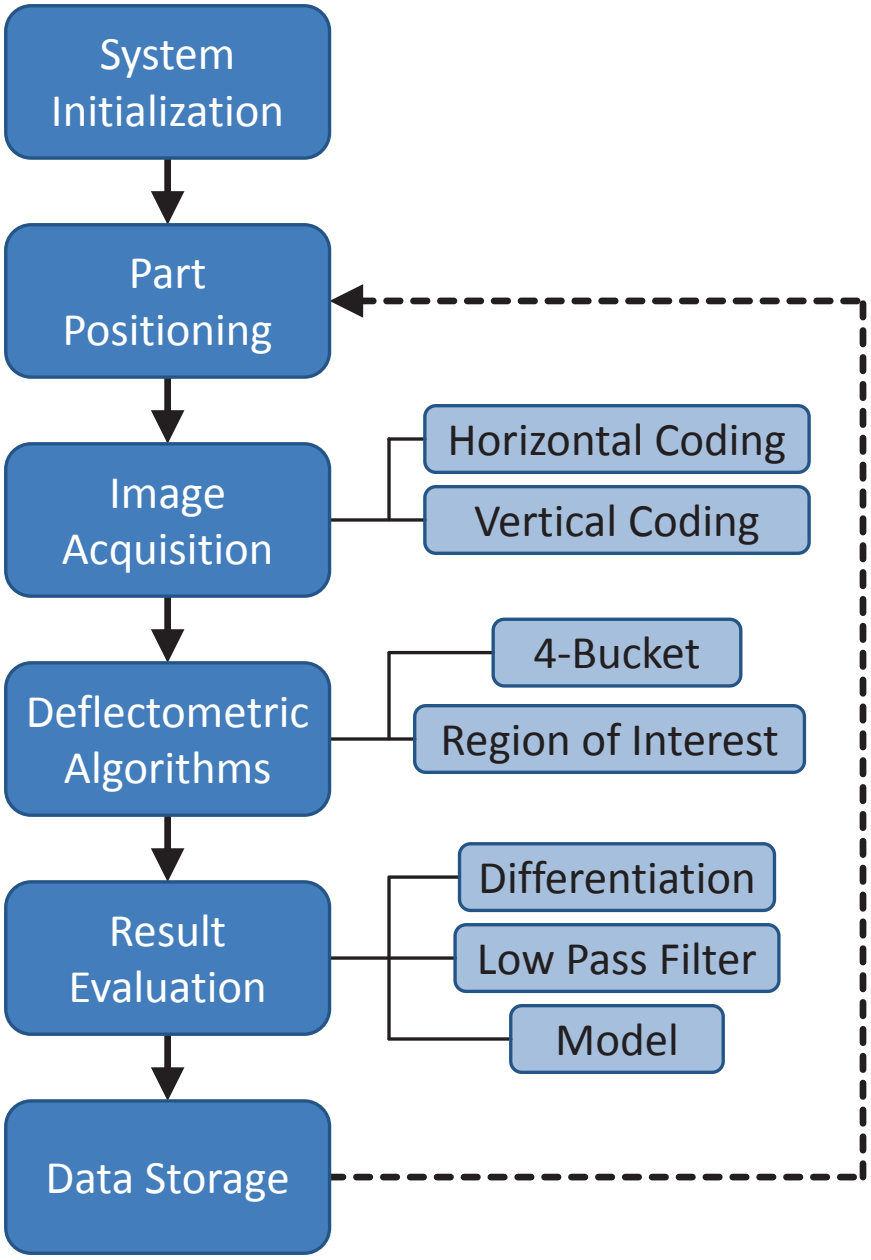

Figure 3.2: Measurement sequence for the inspection of a single injection molded part for sink marks.

3.2 SYSTEM INITIALIZATION

During initialization, the system is prepared for the actual measurement process. Working variables are calculated and allocated beforehand to decrease calculation time during result evaluation. For example, the matrices for polynomial differentiation of the deflectometric results are calculated at the startup of the system and then used for all successive measurements.

Another important task is the establishment of the communications protocols between the measurement PC and the electronic components of the testing site. In Figure 3.3 the communication between the measurement PC and the electronic components is sketched. As can be seen, the communication between the measurement PC and each component happens independently of the other communications. Therefore, feedback about the state of the electronic components was important to maintain chronological order of the measurement sequence. This approach prevented asynchronous behavior of the components, for example premature triggering of the cameras, which would result in artefacts in the measurements. For this reason, strategies for process timing which are based on the status feedback of the electronic components were implemented. These methods will be described in Section 3.3 and Section 3.4.

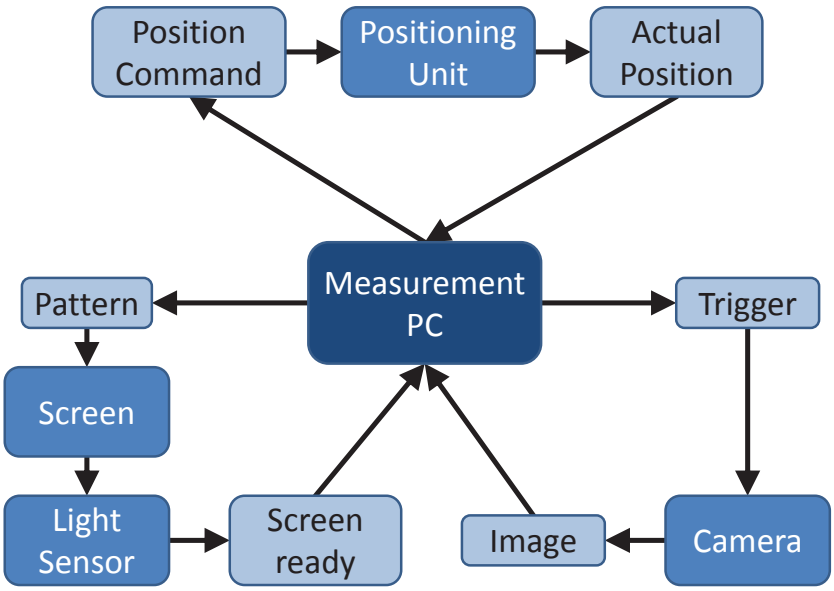

Figure 3.3: Communication between the electronic components of the testing site. The communication between the measurement PC and each component (camera, screen, positioning unit) happens independently of each other.

3.3 PART POSITIONING

Total surface inspection of curved parts is achieved by increasing the number of viewpoints of the inspection setup on the surface. One approach would be the use of one camera for each viewpoint. However, this approach would be expensive and would also require additional calibration of each camera for comparison of the single measurements. Additionally, it would be necessary to reposition the cameras according to a new part configuration. A cheaper and more flexible approach was to use only one camera which was fixed on the frame together with an automatic handling unit which positioned the part for each measurement of the surface. Accordingly, the applied part positioning unit had to be affordable without possible safety implications for staff and material due to moving parts.

The final design of the positioning unit consisted of two off-the-shelf rotation units (see Table 3.1). Aluminium parts were designed as a connection between the rotation units and as a base of the positioning unit. This configuration allowed the adjustment of the tilt and the azimuth of the part relative to the screen and the camera of the testing site.

In Figure 3.4 the tilt axis of the positioning unit is displayed as a dot-dashed line. The connection between the two rotation units was designed

to ensure that the surface of the part and the axis coincide. This was advantageous because the camera of the testing site could be held at one fixed position. Since cameras also feature only a limited depth-of-focus around the focal plane, the measuring volume was limited. This volume defines the region inside the testing site in which the part could be moved around while still remaining in a sufficiently wide depth-of-focus region of the camera. This condition had to be fullfilled to facilitate the capture of suitable measurement images for the deflectometric calculations.

Matching the surface with the tilt axis facilitates the minimization of surface movements out of the focal plane of the camera. In the optimum case, the surface would be positioned parallel to the focal plane, which would ensure that the surface is captured with high and constant sharpness. However, the part positioning had to be optimized for the reflection of the screen patterns into the camera for each surface. The surface was captured at an angle to the focal plane of the camera and, therefore, with varying sharpness. However, this effect was comparatively low due to the arrangement of the positioning unit and could be easily compensated by reducing the aperture of the camera to extend the depth-of-focus. The application of sinusoidal patterns for the deflectometric measurement, as described in Section 2.3.3, further decreases the influence of reduced sharpness due to defocussing of regions of interest on the part.

The communication between the measurement PC and the positioning unit was carried out by COM-ports on the control units for the stepper motors of the rotation units. This interface facilitates the transmission of script commands without the need of additional drivers. The script commands are interpreted by the control units which translate the commands into rotation velocity, duration and direction for the stepper motors of the rotation units. As can be seen in Algorithm 3.1, the actual position is continuously retrieved by a wait-function which pauses program execution until the positioning unit reaches its specified position for the next measurement.

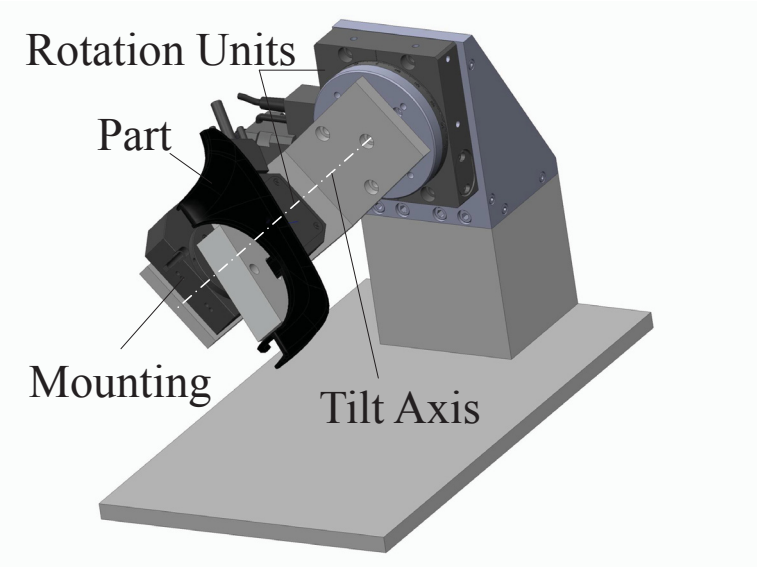

(a)

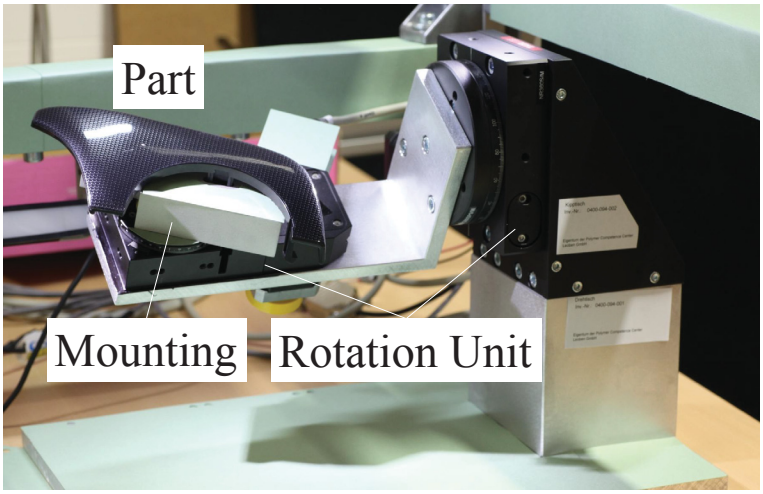

(b)

Figure 3.4: a) Sketch of the positioning unit. The designed aluminium parts are colored gray. The CAD data of the rotation units was obtained from [114] and [101]. b) Image of the positioning unit.

Algorithm 3.1 Command and feedback control of the positioning unit

1: Allocate object COM1 for the COM-port of the rotation unit which produces the tilt θ of the position unit.
2: Allocate object COM2 for the COM-port of the rotation unit which produces the azimuth φ of the position unit.
3: COM1(script command for absolute value of the specified tilt θ_1)
4: COM2(script command for absolute value of the specified azimuth φ_1)
% Define next position for the positioning unit with tilt θ_1 and azimut φ_1
5: **while** $C \neq 0$ **do**
6: Read out actual θ from COM1
7: Read out actual φ from COM2
8: $C = |\varphi - \varphi_1| + |\theta - \theta_1|$
% Cost function
9: **end while**
10: Pause for short duration
% Reduce vibrations during image acquisition
11: Start deflectometric measurement

3.4 IMAGE ACQUISITION AND DEFLECTOMETRIC ALGORITHMS

The arrangement of all components relative to each other is an important factor for the working principle of deflectometric measurements. Several studies exist which define optimum solutions for the arrangement of the components for deflectometric measurements [60, 71, 119]. The results of these studies were used in the development of the testing site. In this work, especially the positioning of camera and screen relative to each other, the focal length of the camera lens and the adjustment of camera focus are discussed further.

One of the major tasks for the development of a deflectometric testing site was to avoid the necessity of calibration. This was achieved by a camera positioned at a long distance to the sample. Such a setup fulfills the conditions which allow the approximation of surface curvature with directional derivatives of the mapping function. Thus, prior calibration of the setup is not necessary, as mentioned in Section 2.3.2. The distances between screen and sample as well as camera and sample in the final setup were chosen to be approximately 500 mm. This distance was thought to be a good compromise between the necessity of long distances between the components of the deflectometric test setup and the maximum space available for a testing site which has to be implemented into a process line. The overall dimension of the testing site, which can be practically implemented into a standard injection molding process, was considered

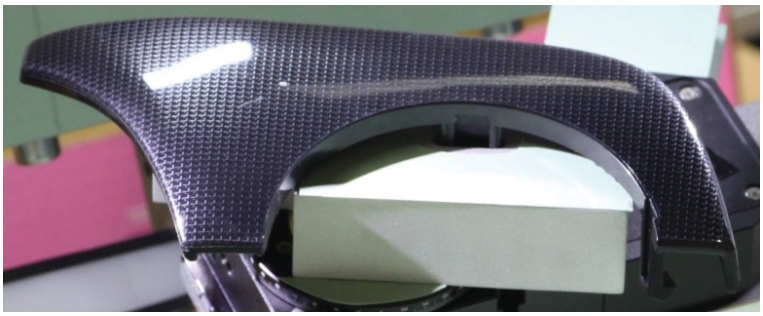

(a)

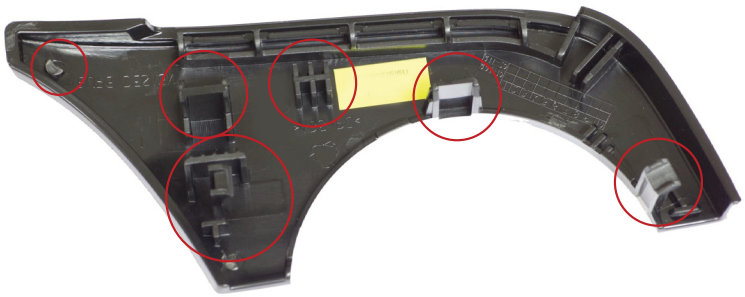

(b)

Figure 3.5: Injection molded part displayed in the mounting of the positioning unit in Figure 3.4. a) Front side of the part, b) back side of the part. All structures which could cause sink marks are marked.

to be less than one cubic meter. Additionally, the camera was positioned close to the monitor, causing the angle between the surface normal of the screen and the viewing direction of the camera to as low as possible. This arrangement facilitates a high reproducibility of the defect detection [119]. Furthermore, the intensity of the reflection from the surface is high due to a low angle of incidence.

Total surface inspection was achieved by subsequent positioning of the sample for each measurement. Accordingly, sample positions had to be found where different regions of the sample reflected the screen into the camera. This task was aided by a suitably large measurement volume which was defined by the positions of screen and camera relative to each other and the sample as well as the picture area of the camera. Besides the distance between camera and sample, the picture area of the camera was dependent on the focal length of its optical lens which had to be chosen accordingly. Small focal lengths would provide a wide-angle view but would also cause image distortions which would influence the measurements. On the other hand, a too large focal length would cause a smaller picture area and therefore a smaller measurement volume.

The injection molded part which is displayed in the mounting of the positioning unit in Figure 3.4 is closer displayed in Figure 3.5 and is used in Section 4.3 to evaluate the measurement concept. In Figure 3.6 a measurement sequence for total surface inspection is displayed for this injection molded part. In addition to one measurement image for each measurement position, the respective black and white map is given which defines the area of the inspected surface region. This black and white map was calculated from Equation 2.39.

Finally, the position of the camera's focal plane relative to the part's surface and the virtual image of the screen's reflection influences the quality of the deflectometric measurement. If the camera is focused on the reflection of the screen, the mapping function between screen and camera is measured with high resolution, while the surface features are averaged due to defocusing. On the other hand, if the camera is focused on the surface, surface features are resolved well, while the resolution of the mapping function decreases. However, a focus on the reflection of the screen caused aliasing between screen and camera pixels in preliminary tests, which caused artefacts in the measurement results. Therefore, the superior approach was to focus the camera between these two extremes but closer to the part's surface. Nevertheless, decreasing the aperture of the camera and the application of sinusoidal patterns for the deflectometric measurement facilitated quite good resolution of the mapping function.

Algorithm 3.2 displays the methods to calculate the mapping function m from the captured images. The 4-Bucket Algorithm, as expressed in Equation 2.38, requires the generation of four phase-shifted patterns (Equation 2.35) for the deflectometric measurement. The function *fullscreen*, which was downloaded from Matlab Central [115], was used for pattern generation on the measurement screen. This Java-based function facilitates fullscreen display of images on a selected screen with Matlab procedures. Acquisition of the measurement images happens after each of the light patterns is generated on the screen which is used as the structured light source. Accordingly, it is necessary to ensure that the image acquisition is not triggered before the respective pattern is fully built-up on the screen. For this reason, a light sensor was attached in one corner of the screen to measure screen luminescence.

In Section 2.3.5, algorithms are introduced to increase the resolution of the deflectometric measurement by iterative measurements. In the first iteration, sinusoidal patterns with periodic lengths which are equal to the screen dimensions are used to calculate rough but unambiguous mapping functions. The periodic lengths of the sinusoidal patterns are decreased with each iteration. Each iteration, a new mapping function is calculated

Figure 3.6: Left column: Example of measurement image for each position. Right column: Black and white maps marking the inspected surface areas which are inspected in the respective deflectometric measurement.

Algorithm 3.2 Determination of the mapping function m from deflectometric measurement

Display black image on measurement screen
repeat
  for $i = 1 : i_{max}$ **do**
% i_{max} ... maximum number of iterations
    repeat
      Generate pattern p_j according to Equation 2.35
% Period of patterns is decreased by factor 2 each iteration i
      Display pattern
      Wait for signal from light sensor
      Image acquisition
      Display black image on measurement screen
    until Image acquisition of g_j for all patterns p_j
    Calculate $\Theta_1 m_l(u,v) \leftarrow \arctan\left[\frac{g_3-g_1}{g_0-g_2}\right]$
    if $i == 1$ **then**
      $\Theta_0 \leftarrow \Theta_1$
% unwrapped phase information Θ_0
    else
      $k \leftarrow \text{round}\left[\frac{2\Theta_{old}-\Theta_1}{2\pi}\right]$
% Θ_{old} is the unwrapped phase information of the prior iteration
      $\Theta_0 \leftarrow \Theta_1 + 2\pi k$
    end if
    if $i == (i_{max} - 1)$ **then**
% Determine the region of the surface which reflects the screen into the camera
      Calculate $\mathcal{I}$ according to Equation 2.39
      Calculate region of interest (*ROI*) from $\mathcal{I}$
    end if
  end for
  $m_l = 2^{-(i_{max}-1)} \frac{L}{2\pi} \Theta_0$
% pixel number L in direction l
until m_l encoded for screen coordinate directions u and v
return Mapping function $m = (m_u, m_v)^T$, *ROI*

from the respective iteration while its ambiguities are resolved with the mapping function from the prior measurement.

The number of iterations should be optimized for the required resolution of the deflectometric measurement, since measurement duration increases considerably with each iteration. This is due to the fact that the number of required images for each measurement increases by eight images for each additional iteration in case of the 4-Bucket-Algorithm (see Section 2.3.3). The large amount of images was the main cause for the long duration of the deflectometric measurements and is a major issue for in-line applications of such a method.

Additionally, the possible maximum number of iterations also depends on the reflection behavior of the inspected surface. The signal-to-noise ratio decreases especially for high frequency patterns due to the increased low-pass behavior of diffusely reflecting surfaces [60]. In this work, four iterations of the deflectometric measurement were carried out for the inspection of the high-gloss injection molded parts.

The reliability of the masking procedure (see Section 2.3.4) was increased by using the pattern with higher periods for the calculations. The increased low-pass behavior of the surrounding surfaces, which reflected the pattern more diffusely than the inspected surface, ensured that only the regions of interest were detected. As can be seen in Algorithm 3.2, the segmentation of the region of interest was carried out in the second last iteration. This iteration was chosen instead of the last iteration to prevent a possible decrease of contrast of the segmentation parameter.

3.5 EVALUATION OF SINK MARK INTENSITY

3.5.1 *Homogenization of the Measurements Using Golden Sample Approach*

The mapping function, which is obtained as result from deflectometric measurements, describes how the screen area is mapped onto the camera sensor via the high gloss surface of the inspected part. Since the part reflects the screen into the camera according to the law of reflection, the mapping function also contains information about the normal vector field of the part's surface. On condition that the camera is positioned far from the surface, the curvature of the inspected surface can be calculated from the two-dimensional mapping function, which is obtained from deflectometric measurements, without prior calibration.

The curvature of the surface can be analyzed to evaluate the intensity of sink marks. However, the influence of the surrounding surface has to be subtracted from the curvature measurement prior to sink mark detection and evaluation, which can then be carried out with simpler and more

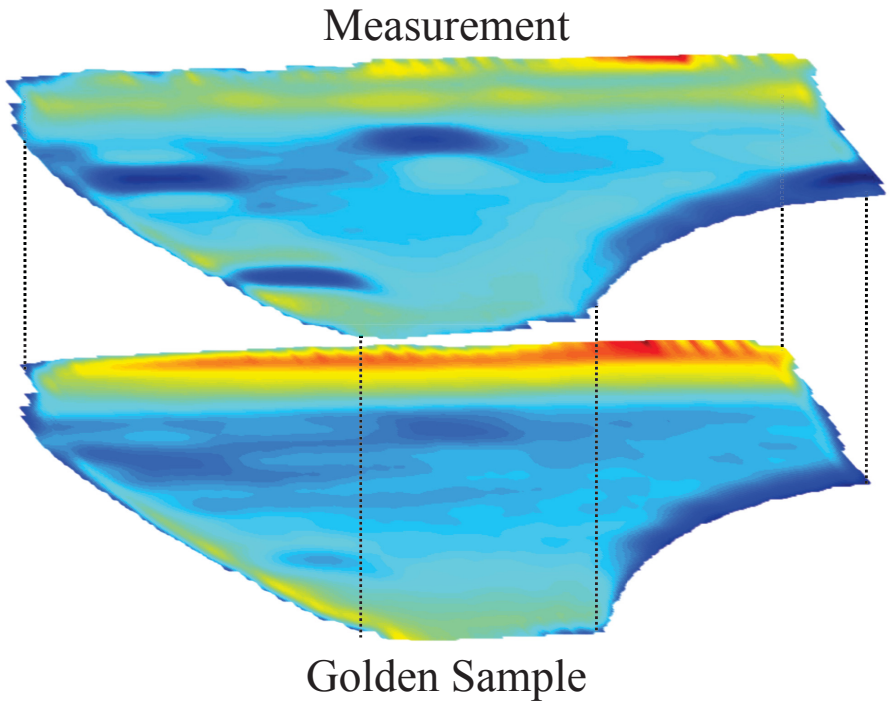

Figure 3.7: Comparison of inspected sample with Golden Sample. The color code relates to the curvature of the surfaces (cyan: flat, blue: concave, red: convex)

robust algorithms. A common option to achieve this subtraction is the application of a Golden Sample, which is formed by a measurement of a pre-defined good part (see Figure 3.7). The quality of an defective part is then classified by its deviations from the Golden Sample. These deviations can be detected using threshold algorithms and evaluated according to their intensity.

However, perfect congruence has to be achieved between the curvature data of the Golden Sample and the inspected sample to prevent artefacts in the measurement. Therefore, shape matching methods are necessary for automatic alignment of the two measurements. Two algorithms for shape matching were tested and evaluated: Shape Contexts [11, 12] and non-linear shape registration [28, 29]. These two methods are used to find point correspondences between two images of the same or similar objects. The gained information was used to enable the calculation of the planar homographic transformation for image alignment in this work. In this method, the homographic transformation matrix was calculated with the direct linear transformation algorithm (DLT; e.g. [51]). The homographic transformation matrix is approximated from the overdetermined solution of the system of equations which is constructed from the correspondences between the contour points of the two images. Since

this algorithm is a linear matrix transformation, the algorithm calculates the homographic transformation matrix between the images quite fast. However, even slight errors in the calculation of contour point correspondences cause considerable errors in the solution of the DLT-algorithm.

In Figure 3.8 shape contexts and non-linear shape registration are applied on the contour of an isosceles triangle. A test shape was generated from the original shape by a translational shift, a shape distortion of 10% of the triangle dimensions and a rotation by 3°. As can be seen in Figure 3.8, these methods work properly if size and shape of the compared objects are similar such as in the examples and if the contours of the objects are well defined. Nevertheless, there are still small deviations between the aligned images in this best case scenario, which are caused by mismatched correspondences of contour points. On the other hand, the deflectometric measurements of curved injection molded parts are optimized for total surface inspection. Therefore, some measurement results feature only a few clear contours or salient points[1]. The contour of the reflecting regions in the measurement images is not determined by the part geometries but the screen area which is reflected from the surface (compare with the measurement regions in Figure 3.6). For these reasons, non-linear optimization algorithms such as the Levenberg-Marquardt algorithm for example, together with, for instance a RANSAC-algorithm for outlier compensation would be necessary for overlaying a deflectometric measurement with a Golden Sample using shape matching algorithms. Such methods are time-consuming, while even small errors in the matching process can cause significant deviations in image alignment. Therefore, shape matching methods were considered as unsuitable for inline applications for deflectometric detection of sink mark.

3.5.2 *Evaluation of the Measurements Using Inverse Patterns*

Another promising approach for surface inspection of high-gloss injection molded parts was the application of inverse patterns [119, 120]. This approach is based on the mapping function which results from deflectometric measurement. This function mathematically describes the mapping of screen pixels onto the camera sensor pixels via the surface of the inspected part. In other words, the mapping function describes how the light pattern which is displayed by the screen is distorted because of the shape of the reflecting surface and the projection onto the camera sensor.

For inverse patterns, the deflectometric registration of the mapping function is used to calculate how the pattern on the screen has to be gen-

[1]Salient points are points of objects or images with prominent features. Therefore, such points are often used as reference points.

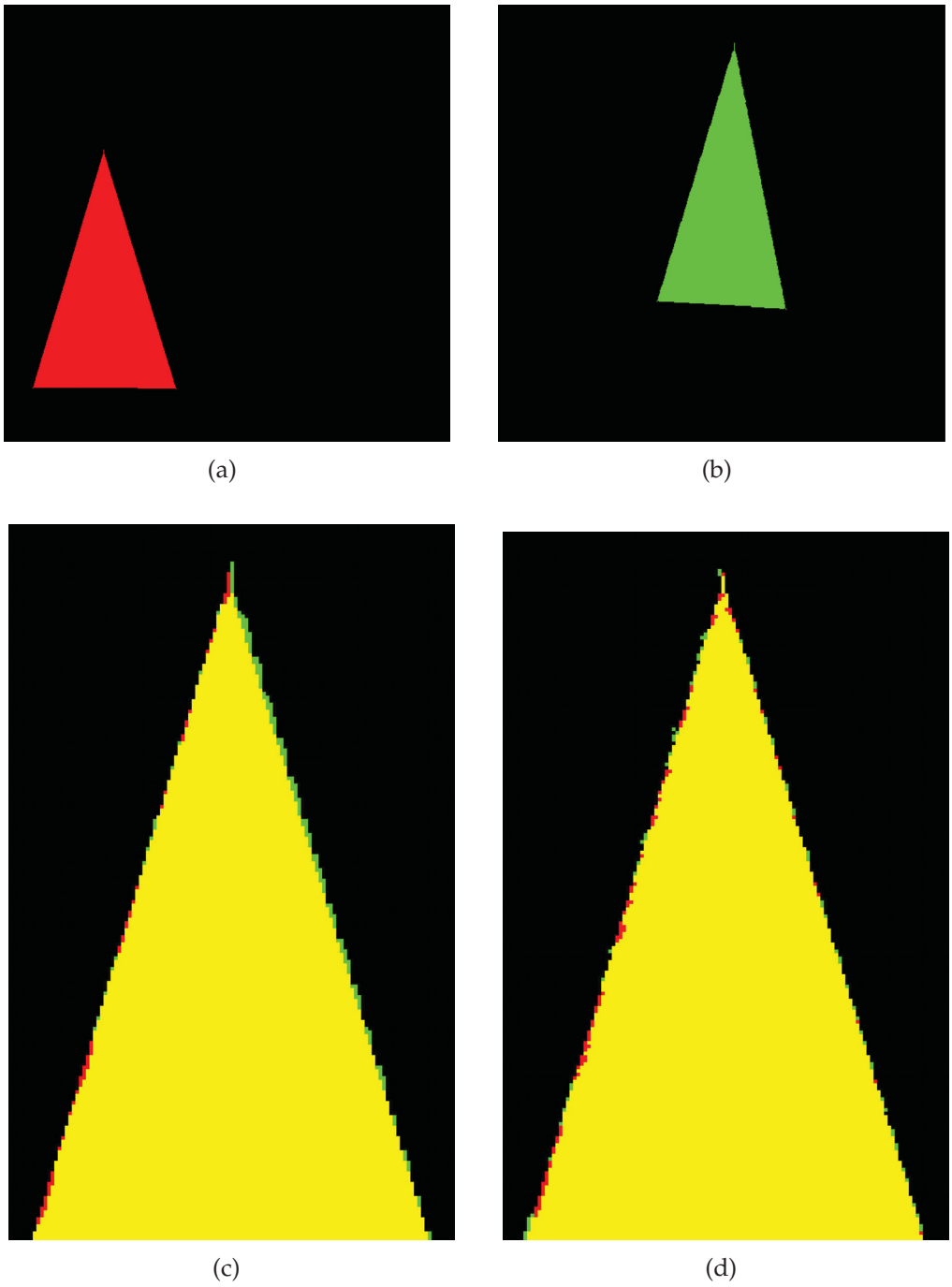

(a) (b)

(c) (d)

Figure 3.8: Performance of shape contexts and planar homography for a simple isosceles triangle. a) Original triangle, b) Shape which is translationally shifted, distorted by 10 % of the maximum dimensions and rotated by 3°. c) Zoomed in results of shape matching with Shape Context [11, 12] and d) with planar homography [28, 29]. (Red: Original Shape, Green: Aligned Shape, Yellow: Overlay)

erated to produce a predefined pattern, for example a periodic pattern such as a checkerboard pattern, on the camera sensor (see Figure 3.9). An

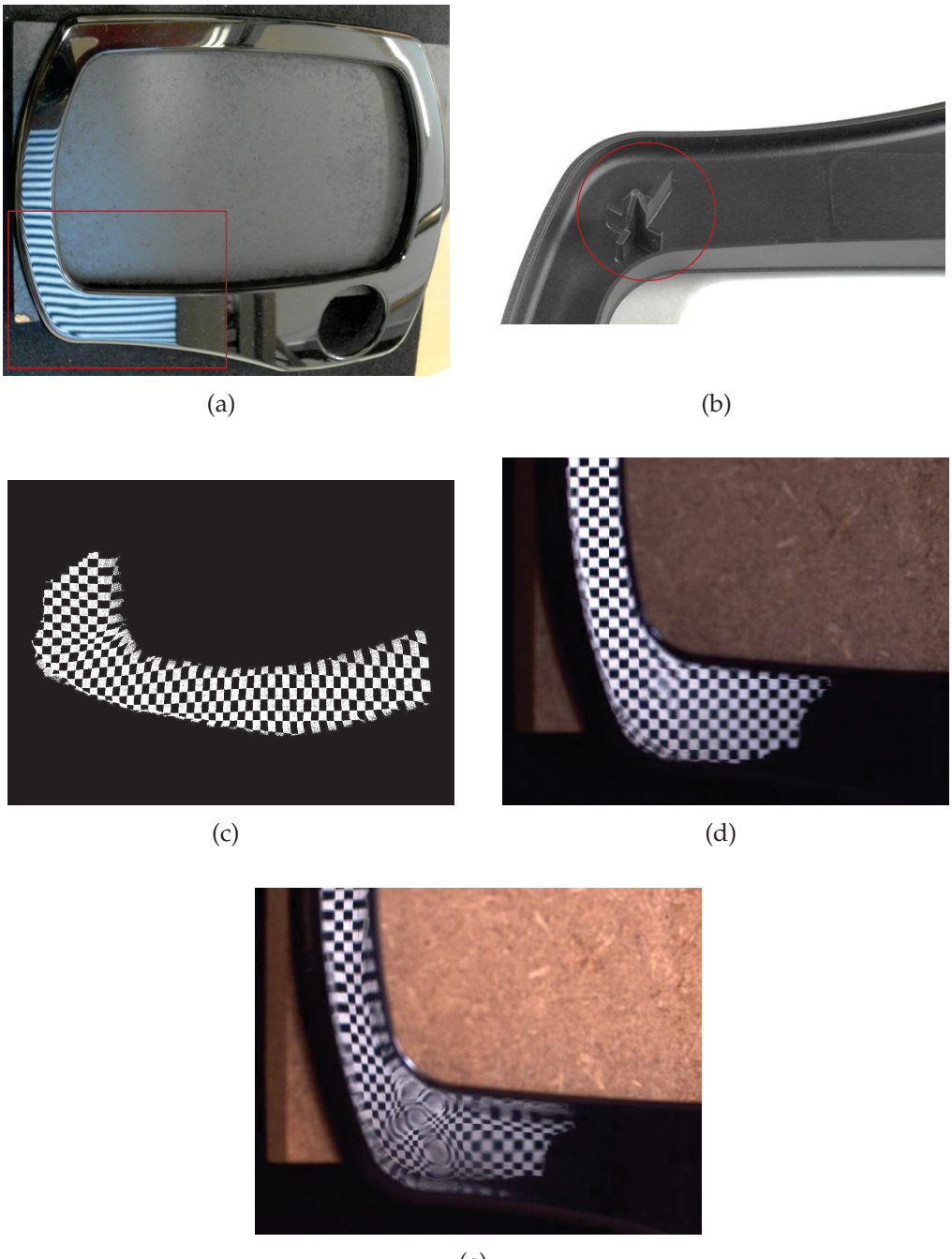

(a) (b) (c) (d) (e)

Figure 3.9: Surface inspection with inverse patterns. a) Front side of the whole injection molded part where the inspected area is marked, b) Back side of the inspected area where the positioning pin which causes the inspected sink mark is marked, c) Inverse pattern displayed by the screen, d) good part, e) bad part

inverse pattern which is generated for a specified good part can be used for quality inspection of other injection molding parts of the same series. Defects such as sink marks which change the surface shape lead to distortions in the periodic pattern which is captured by the camera. Such an approach would be suitable for in-line inspection, since it facilitates fast one-shot surface inspection and the application of simple defect detection algorithms.

However, quality inspection with inverse patterns requires sample positioning with high reproducibility, since even small displacements of the inspected part's surface or slight thermal warpage, which injection molded parts are prone to, lead to considerable distortions in the captured pattern. Such effects would cause false rejection of parts. Additionally, inverse patterns function best on surfaces with homogeneous reflection behavior. Figure 3.10 shows the results of quality inspection of a patterned surface with inverse patterns. Since the pattern of the surface reflects incident light diffusely, it changes the reflection behavior of the otherwise high-gloss surface considerably. Additionally, the inspection of all patterned parts of one test series showed that the pattern was slightly different for each patterned part. This fact was caused by slight differences during the punch out and thermoforming processes of the foils which were used for manufacture of the parts. Therefore, the captured pattern was severely distorted due to the inhomogeneous reflection behavior of the patterned surface which severely reduced the sensitivity of the quality inspection. For these reasons, inverse patterns were abandoned in this work as a quality inspection method despite their many advantages for in-line inspection.

3.5.3 *Homogenization of the Measurements Using Polynomial Base Functions*

Since the application of neither Golden Samples nor inverse patterns resulted in reliable homogenization of the deflectometric measurement, the basic geometry of the curvature was approximated by polynomial regularization. Polynomial base functions were used for regularization and differentiation of the deflectometric measurement results, whereby noise and measurement artefacts were reduced. Then, the surface's curvature was calculated from the algorithms which were introduced in Section 2.3.6. In the next step, the influences of the surrounding surface on curvature, which are large-scaled in comparison with the short-ranged impact of sink marks, were approximated with polynomial base functions from the measurement, similar to the approach of O'Leary and Harker [88].

This process resembles the application of a low-pass-filter on the measurement. However, in contrast to low-pass-filters, which are usually de-

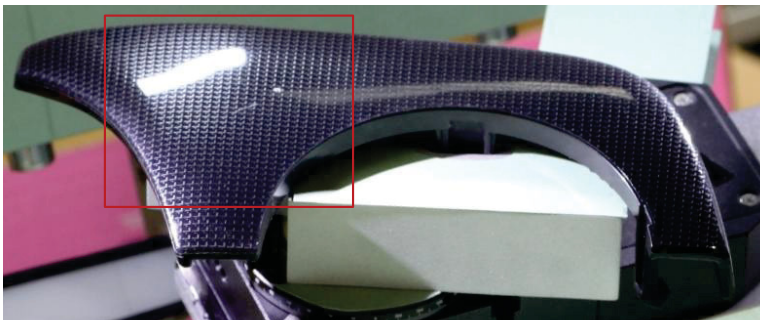

(a)

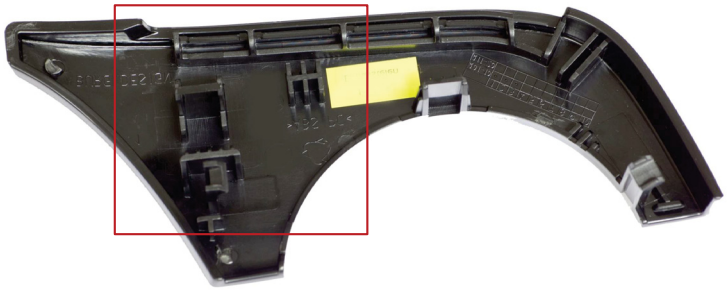

(b)

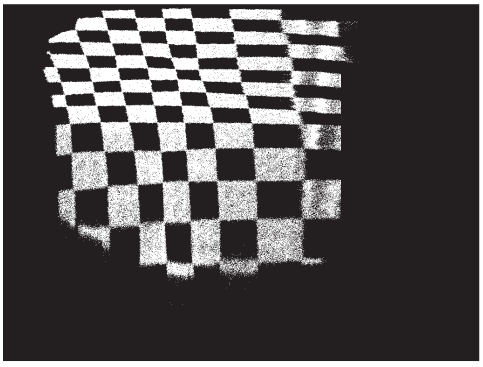

(c)

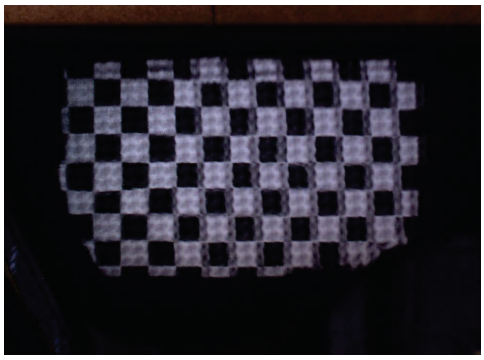

(d)

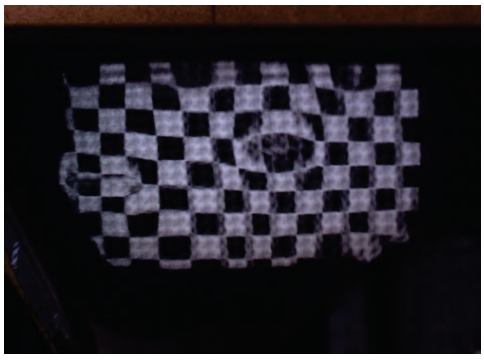

(e)

Figure 3.10: Inspection of a patterned surface with inverse patterns. a) Front side of a print patterned injection molded part where the inspected area is marked. b) Mirror-inverted back side of the injection molded part where the inspected area which features sink mark inducing structures is marked (yellow area covers company logos), c) Generated inverse pattern, d) Reflection of inverse pattern on good part, e) Reflection of inverse pattern on bad part.

(a)

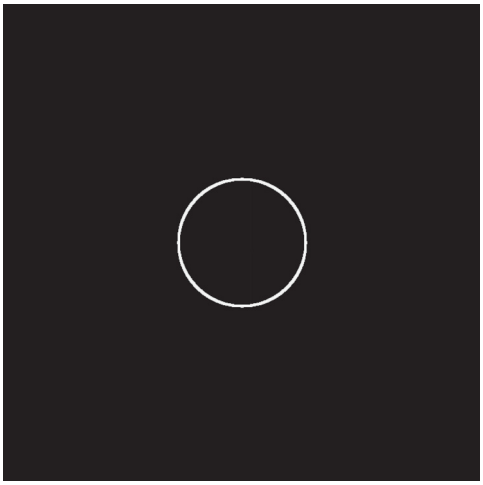

(b)

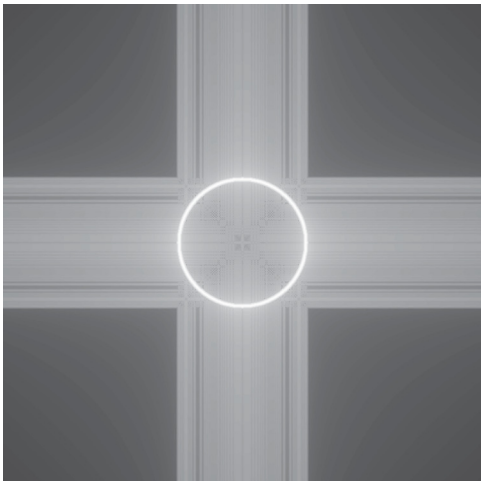

(c)

Figure 3.11: Comparison of Fourier transformation with polynomial base functions. The edge of a circle area is detected by subtracting a low-pass filtered image, b) by polynomial base functions, c) by Fourier transformation. Since the intensities of the resulting images are logarithmically scaled, spectral leakage from the Fourier transformation is visible.

rived from Fourier analysis, the application of polymer base functions facilitate the filtering of non-periodic data. Therefore, this approach reduces spectral leaking and Gibbs ringing artefacts which result from Fourier analysis of non-periodic data (see Figure 3.11 for example). Figure 3.12 shows the application of this approach on a surface region of an injection molded part. Because of the homogenization of the background by subtracting the low-pass filtered approximation, the intensity of the sink marks becomes more distinct. The color code in the following images relates to the curvature of the surface (cyan: flat, blue: convex, red: concave).

However, as mentioned before, the deflectometric measurement is captured only by a fraction of the camera sensor. The content of the complement of the sensor area is omitted by the masking process. Therefore, the correlating parts of the image feature either zeros or not-a-numbers as values. For this reason, interpolations and extrapolation processes are necessary to decrease the influence of the sharp edges in the measurements which were produced by the masking process. Additionally, image points at the border of the deflectometric measurement were strongly influenced by the values of the interpolated points. In Figure 3.13 a measurement image is weighed with the confidence for each measurement point. The center of the region of interest features 100% confidence while the confidence decreases to the border. Thereby, the ratio between extrapolated and measurement points which were used for the calculation of the smoothed measurement is used to estimate the confidence. The contour points of the region-of-interest feature the lowest confidence because of the maximum number of $(n-1)/2$ estimated points, where n is the number of points which were used in the smoothing calculation. Therefore, surface regions which featured sink marks were put in the center of measurement regions when the setup of the testing site allowed it.

3.5.4 *Evaluation Model*

In the next step, the sink marks are detected by applying a regional maximum search algorithm and evaluated with a model which is based on the results of Hayden [53]. In several assessment studies Hayden found that the perceptibility of sink marks on high-gloss surfaces is mainly dependent on the local curvature as well as the area of the sink marks. Therefore, the following model combines area and curvature of sink marks into

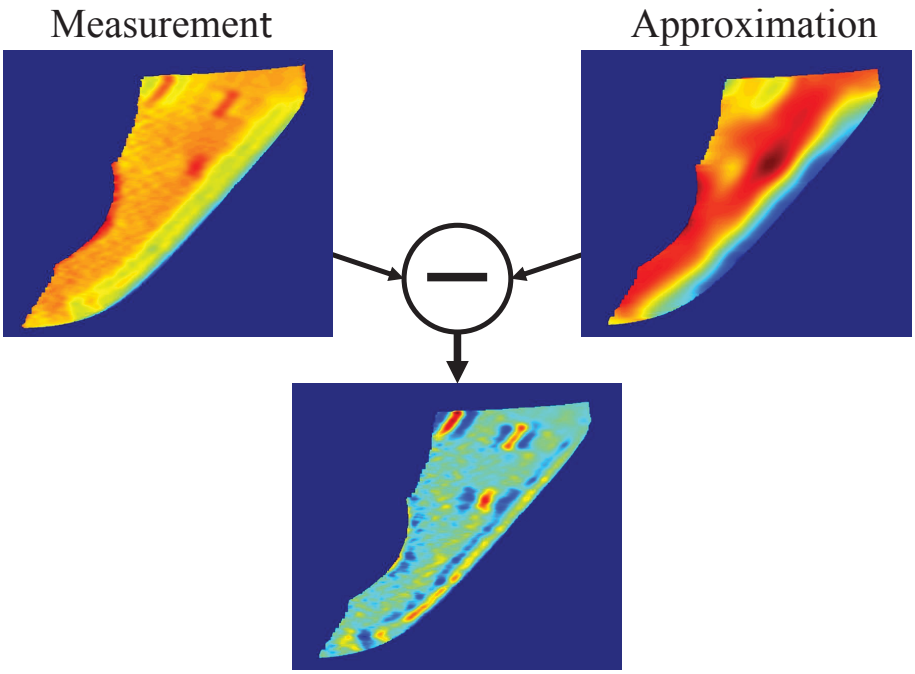

Figure 3.12: Preprocessing of the measurement results of an inspected surface region by application of polynomial base functions (injection molded part is displayed in Figure 3.10(a)). The approximation (right) is calculated from the measurement (left) using polynomial base functions. After subtraction of the approximation from the original measurement, the distinctness of the sink marks in the processed image (below) is increased. The color code relates to the curvature of the surface (cyan: flat, blue: convex, red: concave).

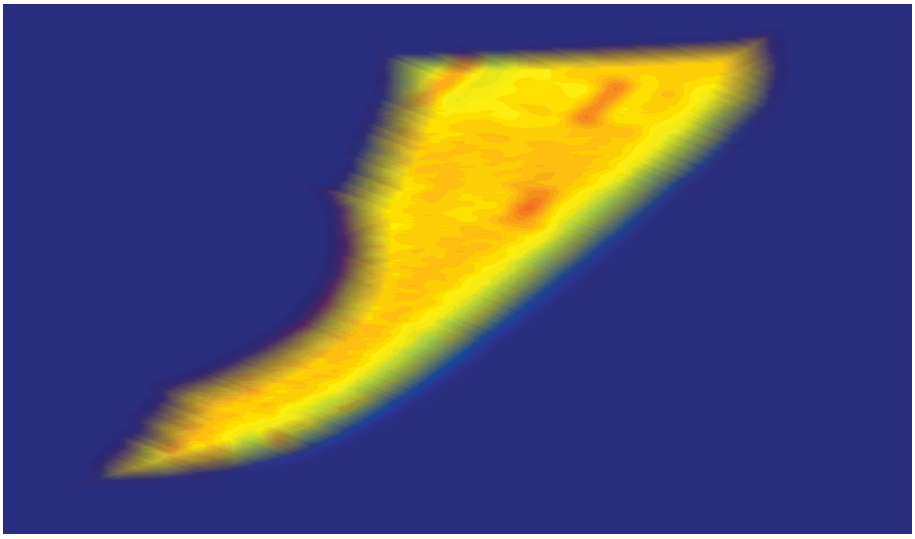

Figure 3.13: Deflectometric measurement of curvature (see Figure 3.12) with its confidence value in dependence to number of extrapolated image points. The measurement becomes transparent proportionally to the decrease of confidence.

a feature parameter to calculate the visual intensity of the sink marks. Mathematically it can be expressed by

$$\text{Intensity} = \int_{A_s} \kappa \mathbf{d}A, \tag{3.1}$$

where κ is the curvature of the evaluated sink mark and A_s its area. The size of the area is defined by the width at half maximum of sink mark curvature. This model works well for point-shaped sink marks because of their rotational symmetry. However, sink marks with more complex shapes can only be roughly approximated with this model, since the model does not take the dependence of sink mark intensity on the viewing direction into account. However, the model can still be used for qualitative evaluation of the intensity of such sink marks.

In Algorithm 3.3 the strategies for the calculation of sink mark intensity from the mean curvature κ_{mean} are shown. First the mean curvature is calculated from the mapping function which resulted from the deflectometric measurement. Afterwards, the model as stated in Equation 3.1 is applied on the mean curvature which was homogenized with the regularized approximation of the basic curvature geometry.

Algorithm 3.3 Evaluation of sink mark intensity

1: **repeat**
2: Prepare regression matrices S_x and S_y
3: Prepare differentiation matrices D_x and D_y
% Matrices generated with the DOP-toolbox [50]
4: $T_1 = m_u D_x + m_v D_x$
5: $T_2 = D_y m_u + D_y m_v$
% Approximation of the Weinberg-Matrix according to Equation 2.59
6: $\kappa_{mean} = \frac{1}{2}(T_1 \circ T_1 + T_2 \circ T_2)$
% Equation 2.60
7: Use average-filter to calculate the $\sum_{\mathcal{N}}$ of the neighborhood $\mathcal{N}$
% The order of linear operations has no influence on the result
8: $\kappa_{mean} \leftarrow \kappa_{mean} - S_y \kappa_{mean} S_x$
% Homogenization of the background
9: Detection of sink marks using local maximum detection
10: Calculate the area of the sink marks
11: Calculate sink mark intensity according to Equation 3.1
12: **until** done for all inspected regions of the part's surface
13: **return** Sink mark intensities

4

RESULTS

4.1 GENERAL CONSIDERATIONS CONCERNING THE INSPECTED INJECTION MOLDED PARTS

The injection molded parts which were selected for the test series had to feature several properties. First, it was crucial that the inspected injection molded parts were examples for current designs in industry. This ensured the applicability of the deflectometric method for quality inspection problems which the plastics industry has to face nowadays. Therefore, the inspected injection molded parts were chosen from the recent production of industrial partners. Accordingly, parts with curved surfaces were chosen to evaluate the performance of the introduced deflectometric test setup for such parts.

Besides shape, an important criterion for the choice of suitable test samples was the color of the inspected parts. Experience showed that bright colored surfaces facilitate considerable emission of diffusely reflected light which interferes with the deflectometric measurement concept. In Figure 4.1 the measurement images of a white and a black sample are shown. In comparison to the black sample, the contrast of the light pattern on the white surface is considerably decreased due to diffuse reflection. Therefore, the sensitivity of the deflectometric measurement was expected to decrease to the same effect.

However, a comprehensive study on the effects of color on the performance of the deflectometric measurement was beyond the scope of this work. It was decided to focus on the evaluation of the deflectometric method combined with an affordable system for part positioning for the measurement of curved injection molded parts. Another topic of this work was the development of a model for sink mark intensity. In Section 4.2 and Section 4.3 two parts which were used to evaluate the measurement concept and their measurement results will be introduced. Contrary to the examples in Section 2.3, these parts are curved, which makes the application of a positioning unit necessary.

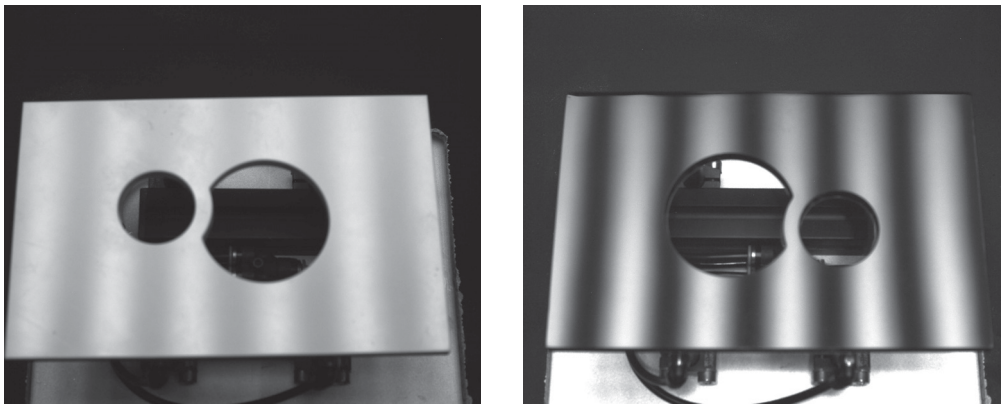

(a) (b)

Figure 4.1: Influence of the inspected sample's color on the contrast of the light pattern in measurement images: a) white sample, b) black sample.

4.2 INJECTION MOLDED PART "COFFEE MAKER FRONT PANEL"

4.2.1 *Part Description and Test Series Preparation*

Figure 4.2 displays the inspected part "Coffee Maker Front Panel" (courtesy of Wittmann Battenfeld GmbH). The process called BFMOLD®, which is licensed by Wittman Battenfeld GmbH, was used to achieve a high-gloss surface of the part without the need of coatings or quality increasing foils. This process applies a two-way system of hot and cold water to rapidly heat and cool the fixed half of the mold during the process cycle. This facilitates the application of a higher mold temperature without a large increase of cooling time. In Table 4.1 the settings of the main parameters test series production are displayed. The material which was used for manufacture was Terluran® GP35 by BASF Österreich GmbH (see Section A.2).

The high-gloss injection molded part is curved, however, its shape can still be described in terms of polynomial equations, in this case as parabola or cylinder jacket. The specification of measurement positions was easily achieved with the positioning unit introduced in Section 3.3 due to its cylindrical symmetry. For the same reason, the surface of the part was only negligibly moved outside of the focal plane. The inspected sink marks are nearly spot-shaped and are caused by screw bosses on the back of the part which are located close to its corners (see Figure 4.3). The model introduced in Section 3.5.4 was expected to give a good estimate for the intensity of the sink marks because of their rotational symmetry. For these reasons, this injection molded part was considered to be well-suited for a first evaluation of the measurement concept of "sink mark

Table 4.1: Processing parameters for production of the "Coffee Maker Front Panel" test series

Parameters	Values
Die temperature, C	250
Injection volume rate, cm^3/s	25
Max. injection pressure, MPa	136
Holding pressure, MPa	75 – 95 (inkr. 2.5)
Cooling time, s	30
Mold temperatures, C	
low value	75
high value	155

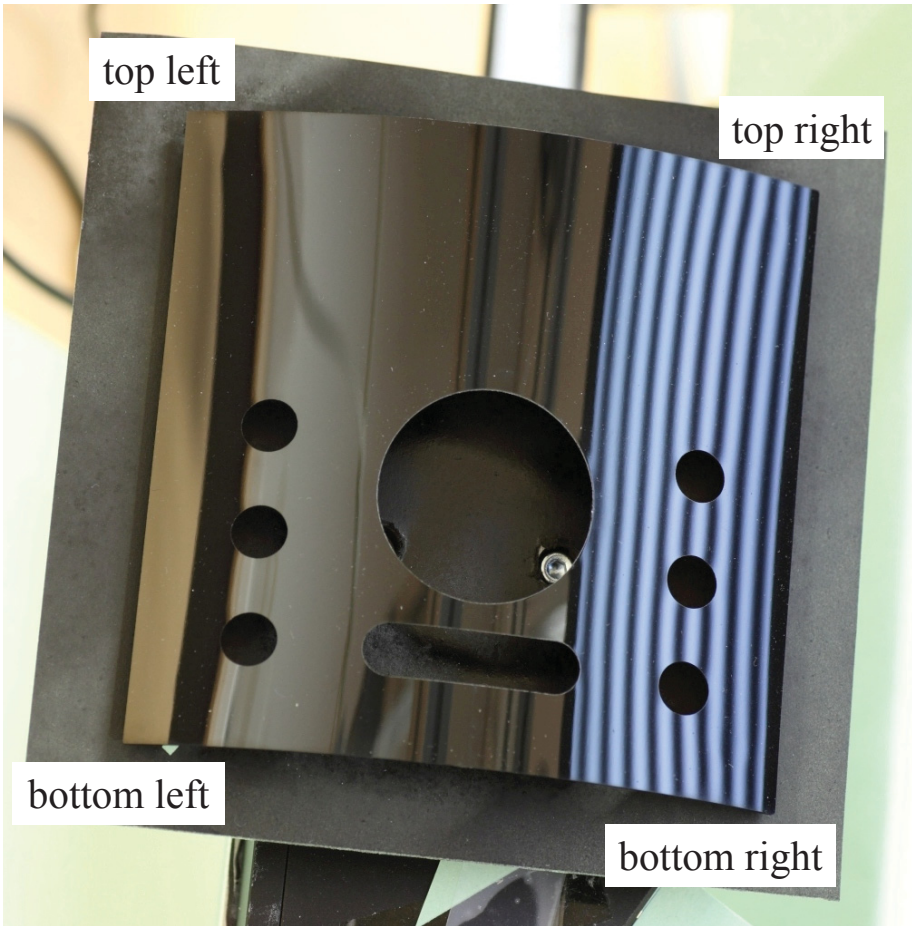

Figure 4.2: Front side of the injection molded part "Coffee Maker Front Panel" (courtesy of Wittmann Battenfeld GmbH) with dimensions of $100 \times 100\,mm^2$. The inspected sink marks are located in the corners of the part.

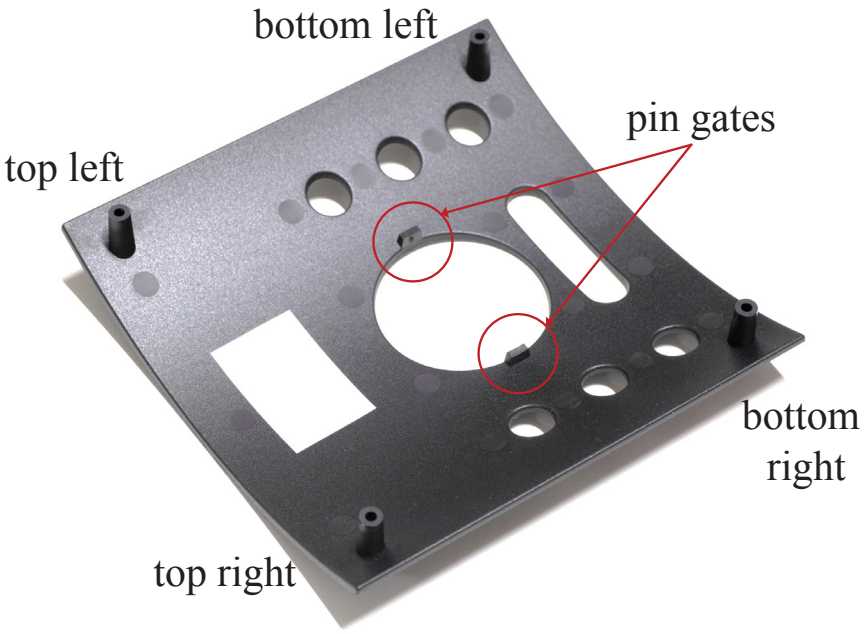

Figure 4.3: Back side of the injection molded part "Coffee Maker Front Panel". The screw bosses in the corners of the part cause the inspected sink marks.

intensity", which uses the phase measuring deflectometry as a detection method as described in Section 2.3 and Section 3.4.

For the evaluation of the testing site and the intensity model used, test series had to be manufactured. It was important to ensure that the production of the parts was as reproducible as possible within one series. As suitable parameter settings were found for the production of good parts, only the holding pressure was varied for test series production. The holding pressure, one of the main factors for sink mark formation or prevention [42], can be changed fast without long latency until the process is stabilized again.

The production of the test series was carried out by reducing the holding pressure, which started from 95 MPa, incrementally in 2.5 MPa steps. For each test series, the parts of the series were taken after at least ten molding cycles had passed after the change in holding pressure to ensure a stable process. In this case, the process stability was evaluated by checking the hydraulic pressure curve and the mold temperature each cycle. This procedure was repeated until test series were manufactured for a holding pressure range from 75 MPa to 95 MPa.

4.2.2 *Results of the Deflectometric Measurements*

Figure 4.4 shows an array of cropped deflectometric measurements of the sink marks and their surroundings. To emphasize the differences between the results of the test series, the increment between the chosen test series was 5 MPa. One example for each test series and sink mark is depicted exemplarily. As can be seen, the distinctness of the sink marks intensity decreases with increasing holding pressure.

In Figure 4.5 the graphs show the calculated mean values of the intensities of the four sink marks, where six samples were used for each data point. The results were in accordance with the expectation that sink mark intensity increases as the holding pressure decreases. At a holding pressure of 85 MPa, the increase of sink mark intensity declines, which can be explained by pressure losses between the gates at the central recess of the part and its corners (see Figure 4.3). Below this level the holding pressure does not reach the corners of the parts and the thermal shrinkage is at its maximum. Comparison of the graphs in Figure 4.5 shows that the detected intensities of the bottom sink marks are higher than the intensities of the top sink marks. The differences between the intensities of top and bottom sink marks becomes more pronounced especially at maximum holding pressure. This behavior can be explained by higher pressure losses between the gate and the bottom sink marks. The flow of the melt to the two bottom sink marks is inhibited by six symmetrically positioned smaller cut-outs (see Figure 4.2), which results in a higher perceptibility of the bottom sink marks in comparison to the top sink marks. Asymmetries of the mold, such as differences in temperature, wall thickness and pin gate diameter, could be the cause for the higher intensities of the left sink marks compared to the right sink marks. Unfortunately, those properties of the mold could not be measured due to limited availability of the mold.

4.2.3 *Comparison with Topographical Measurement*

The topography of the sink marks was measured to evaluate the results of the deflectometric measurements. Based on light and matter interaction processes such as light scattering and diffraction as well as selective light absorption and reflection, the perceptibility of surface features like sink marks is normally dependent on the given surface structure, material and color [37, 40, 41]. For black high-gloss parts, this dependency is reduced to the topography of sink marks. For these reasons, the top right and bottom right sink marks (see Figure 4.2) were measured for all test series with a chromatic confocal microscope type FRT Microprof® by Fries Research &

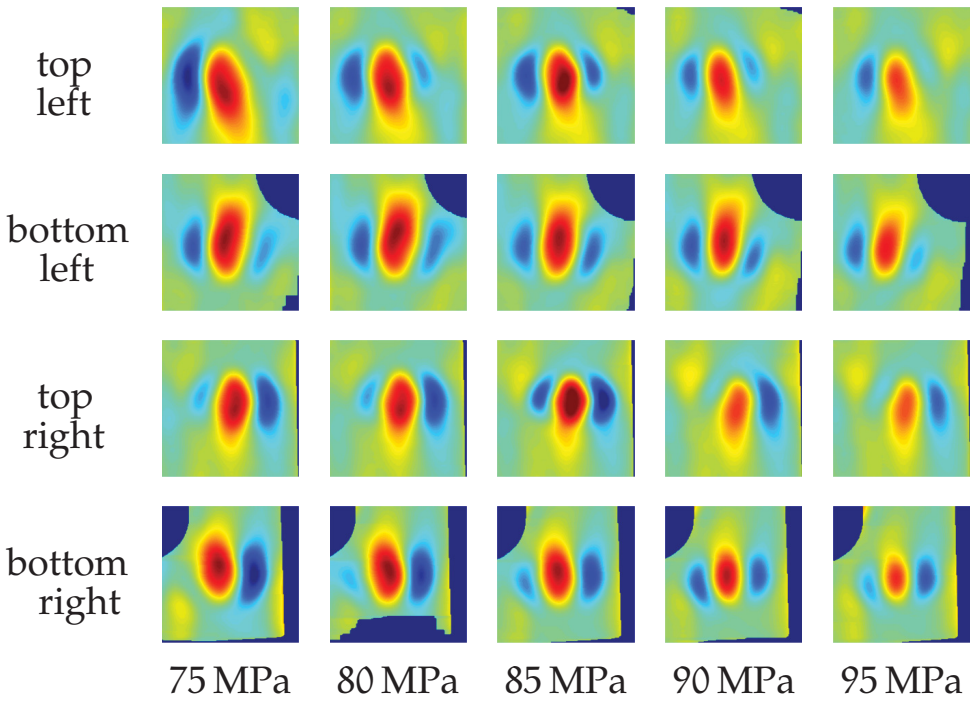

Figure 4.4: Deflectometric measurement of sink mark intensities. The increment of the holding pressure between the selected test series amounts to 5 MPa. The color code relates to the curvature of the surface (cyan: flat, red: concave, blue: convex; at 75 MPa: sink mark depth >7.5 µm, at 95 MPa: sink mark depth ~3 µm).

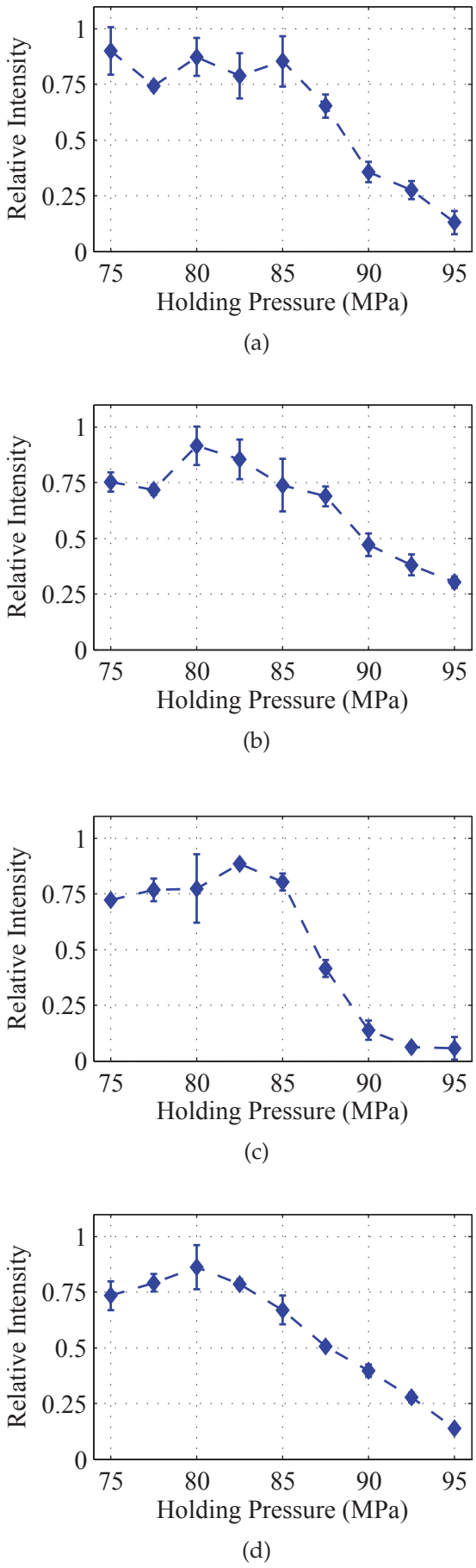

Figure 4.5: Means of sink mark intensities for each test series: a) top left, b) bottom left, c) top right, , d) bottom right sink marks.

Table 4.2: Parameters of the topographic measurements with the chromatic confocal microscope FRT Microprof®

Parameters	Values
Measured area, mm×mm	17×17
Pixel resolution, px	340×340
Max. lateral range, mm×mm	200×200
Max. vertical range, µm	3000
Lateral resolution, µm	< 6
Vertical resolution, nm	100
Measurement frequency, Hz	2000

Technology GmbH. The measurement principle of this device is based on the chromatic aberration of optical lenses. The index of refraction of materials is dependent on the wavelength of the refracted electromagnetic waves. For this reason, the colors of white light are focused at different focal lengths. The FRT Microprof features a point light source and a point detector which are used confocally with the same optical lens. Because of chromatic aberration of the lens, only electromagnetic waves with a specific wavelength are focused from the point source onto the surface and form a sharp high intensity light point on the surface. Other wavelengths are defocused and form dots of lower intensity. The light dots are detected by a photosensitive point detector. The same lens as was used to project the light dots on the surface is used to focus the light back from the surface onto the detector. Therefore, only the electromagnetic waves which were focussed on the surface are captured with high contrast and and intensity. By using the wavelength and the optical aberration of the lens, the height information of the surface is calculated. This method facilitates pointwise topographical scans of surfaces. The parameter setting of the measurement is listed in Table 4.2.

The measurement results were expected to be a superposition of two peaks due to the tilted arrangement of the hollowed screw boss at the back of the part. The base area where the screw boss connects to the wall of the part is not a circular but an elliptic ring. Therefore, the base area forms two larger areas at the ends of the longer axis of the elliptic base (see Figure 4.6). Since these two areas are at a greater distance to each other and larger sized compared to a perpenticular cut, the sink mark features two peaks instead of a ring shape.

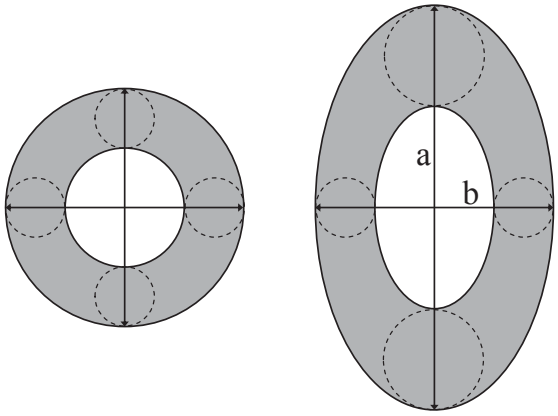

Figure 4.6: Sections of the screw boss. Left: Section of the screw boss perpendicular to its axis. Right: Angled section of the screw boss. The section becomes elliptical where two larger areas are formed opposite to each other along the larger axis a. The shorter axis b is defined by the diameter of the screw boss.

Similar to the approaches of Gruber et al. [43] and Pacher et al. [100], the measurements were fitted to an analytical model. The fitting parameters of the two peaks are calculated separately from a fitted curve. The model is given by

$$f(x, y) = A_1 \cdot p_1(x, y) + A_2 \cdot p_2(x, y) + \text{poly33}. \tag{4.1}$$

A_1 are A_2 are the amplitudes of the peaks p_1 and p_2 which are given by

$$p_i(x, y) = [\eta_i \cdot g_i(x, y) + (1 - \eta_i) \cdot h_i(x, y)]\,. \tag{4.2}$$

The peak shape was modelled as a superposition of the Gaussian function

$$g_i(x, y) = \exp\left[-\frac{(x - \mu_{xi})^2}{2\,\sigma_{xi}} - \frac{(y - \mu_{yi})^2}{2\,\sigma_{yi}}\right] \tag{4.3}$$

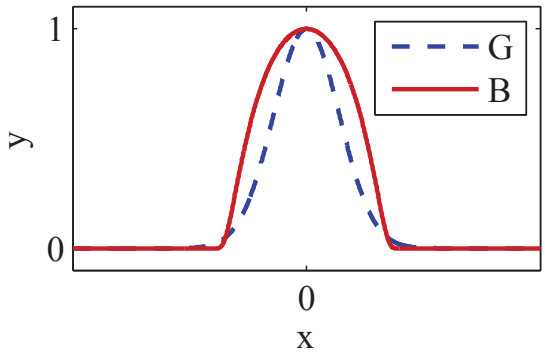

Figure 4.7: Comparison of Gaussian and bump function. The bump function features the wider peak (G...Gaussian, B...bump function).

and the elliptical bump bell function

$$h_i(x, y) = \begin{cases} \exp\left[\frac{1}{\left(\frac{x-\mu_{xi}}{b_{xi}}\right)^2+\left(\frac{y-\mu_{yi}}{b_{yi}}\right)^2-1}+1\right] & \text{for } \left(\frac{x-\mu_{xi}}{b_{xi}}\right)^2+\left(\frac{y-\mu_{yi}}{b_{yi}}\right)^2<1 \\ 0 & \text{else} \end{cases} \tag{4.4}$$

The bump bell function is based on the compact bump curve which is well-known from the theory of generalized functions (e.g. [68]). It was also chosen because this function is compact and smooth. In Figure 4.7, a bump function is plotted compared to a Gaussian function.

The model parameters of the model are listed in Table 4.3. The expression "poly33" resembles a two-dimensional polynomial of degree three which was applied to fit the macroscopic surface shape.

Table 4.3: Fitting parameters of the model for sink mark shape in Equation 4.1 where the peaks (Equation 4.2) consist of a Gaussian function (Equation 4.3) and a bump function (Equation 4.4)

Variable names	Parameters
A_i	Amplitudes of the peaks
η_i	Ratios of the superposition in Equation 4.2
μ_{xi}, μ_{yi}	Position coordinates of the function peaks
σ_{xi}, σ_{yi}	Standard deviations of the Gaussians
b_{xi}, b_{yi}	Half-axes of bump function areas

This approach to model sink mark peaks with a superposition of a Gaussian shape and another distribution is similar to the approach of Pacher et al. [100] where the Pseudo-Voigt-Function was used, which is the superposition of a Gaussian distribution and a Cauchy distribution. This model was used to describe peaks of inspected sink marks, which were caused by rectangular ribs, as function with a narrower peak and fatter tails than the peak of the Gaussian curve. The function which is introduced in the given work is considered as a complementary model to the former approach and is used for the approximation of sink marks with wider peaks and thinner tails compared to a Gaussian distribution.

Therefore, the bump function which is expressed in Equation 4.4 was chosen for superposition with the Gaussian function instead of the Cauchy distribution. The parameter *excess kurtosis* defines if a distribution is leptokurtic (narrow peak, fatter tails, positive excess kurtosis) or platykurtic (wider peak, thinner tails, negative excess kurtosis) relative to the normal distribution (excess kurtosis $= 0$). The excess kurtosis can be calculated from

$$\text{excess kurtosis} = \frac{\mu_4}{\mu_2^2} - 3 \tag{4.5}$$

where μ_2 is the second moment and μ_4 is the fourth moment of a distribution. Due to the high complexity of the integrals for the moments of the bump function, its excess kurtosis was only calculated numerically by the trapezoidal rule. Anyway, the integrals for the calculation of its moments are expected to exist because the bump function is per definition compact. The bump function is strongly platykurtic with a value of the excess kurtosis of -0.8807 which makes it suitable for the demanded analytical model[1].

Figure 4.8 shows an example for the measurements of top right sink marks of the test series with a holding pressure of 75 MPa. The model (surface) approximates the shape of the sink mark (x's) adequately, which is also reflected by a R^2 value of more than 97%. The color code of the model surface relates to sink mark depth.

The model facilitates the calculation of two feature parameters for the sink mark from the topographic measurements. The first parameter is the amplitude of a sink mark which is calculated as difference between the fitted reference plane and the deepest point of the calculated model. The

[1] In comparison: The unitary distribution features an excess kurtosis of -1.2

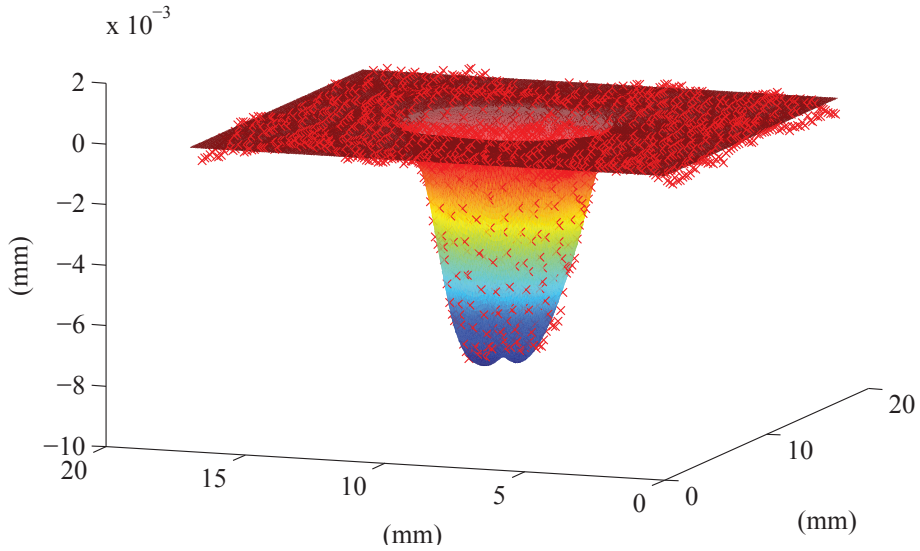

Figure 4.8: Example for a topographical measurement of the top right sink mark. The model expressed in Equation 4.1 is used for the fit (surface). Smoothing of the data points (x's) and subtraction of the macroscopic surface shape were already applied to increase the visibility of the displayed sink mark. The color code of the model surface relates to sink mark depth.

second parameter is called the volume of a sink mark. This parameter is calculated from the numerical Riemann quadrature

$$V = \int_{S_A} f(x, y)\,dx\,dy \approx h_x \cdot h_y \cdot \sum_{m,n} f(x_0 + m \cdot h_x,\, y_0 + n \cdot h_y) \qquad (4.6)$$

with the model values f(x,y) over the sink mark area S_A and the increments h_x and h_y between the point coordinates. Thereby, the borders of the area were defined by the half-maximum values of the sink mark model.

The model was fitted to the measurements of the top and bottom right sink marks. The mean values of amplitude and volume of the sink marks were calculated for all test series. In Figure 4.9 and Figure 4.10 the means of the sink mark amplitudes and volumes were plotted as a function of the holding pressure. At 82.5 MPa and 85 MPa sink mark amplitudes and volumes are higher than was expected. One explanation for this behavior is the thermal warpage that happens around the sink mark location during cooling. In contrast to expectations, the interference of the warped surface with the fitting of the sink mark leads to lower sink mark depths at the abovementioned holding pressures.

According to another explanation, voids are formed underneath the surface at very low holding pressures during manufacture. Since the wall thickness of the screw bosses is of the same order of magnitude as the wall thickness of the part, comparatively large pools of liquid melt are formed at the screw bosses. If the holding pressure is below a certain level, the strain inside the material could be high enough to form voids. The formation of cavities could release the strain on the surface of the part at the same time, which causes lower sink mark depressions. Nevertheless, the formed voids are expected to be in the range of microns because of the small effect on the sink marks' size. Such structures cannot be investigated by destructive methods such as preparation with a microtome because these fine structures would be destroyed. On the other hand, computer tomography measurements, especially with the required resolution, are expensive and not the focus of this work. However, the absolute geometries of the sink marks are well described with the topographic measurements. Therefore, it is considered to be sufficient to compare the deflectometric measurements to the features of the sink marks which result from the topographic measurements.

In Figure 4.11 and Figure 4.12, as well as, Figure 4.13 and Figure 4.14, the results for the amplitude and the volume of the sink marks are compared to the results of the deflectometric measurements. The topographic measurements strongly correlate to the deflectometric measurements, which is reflected by the high R^2 values for the line fits for the plots of the deflectometric measurement as a function of the topographic feature parameters sink mark amplitude and volume, respectively. This high linear correlation also allows for a rough estimation of the relative error and the resolution of the measurement. The largest errorbar of the deflectometric measurements was used as a reference for the relative error and was converted into the scale of the topographical amplitude measurements to get an estimate for the resolution of sink mark depth. The relative measurement error was estimated around 15 % and the resolution of sink mark depth was estimated around 1 µm.

Especially comparison of Figure 4.12(a) and Figure 4.14(a) gives the indication that the volumes of the sink mark correlate better with the deflectometric measurements than the amplitudes. This behavior was expected, since the calculation of sink mark intensity from deflectometric measurements, as well as the calculation of the volumes, is dependent on the sink mark area. Especially, the bottom right sink marks (see Figure 4.12 and Figure 4.14) show differences between the results for the amplitudes and volumes. In comparison to the top right sink mark (see Figure 4.11 and Figure 4.13), the bottom left sink marks are shallower. However, their peaks are wider, since their volumes amount to values comparable to the

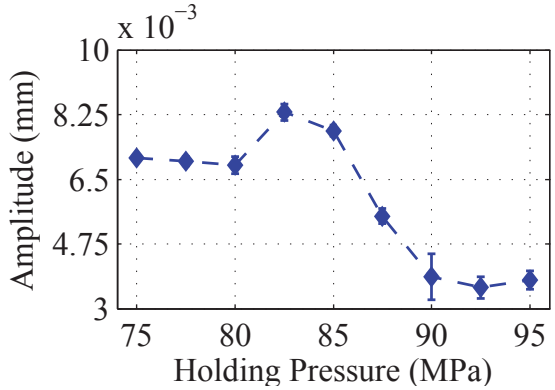

(a)

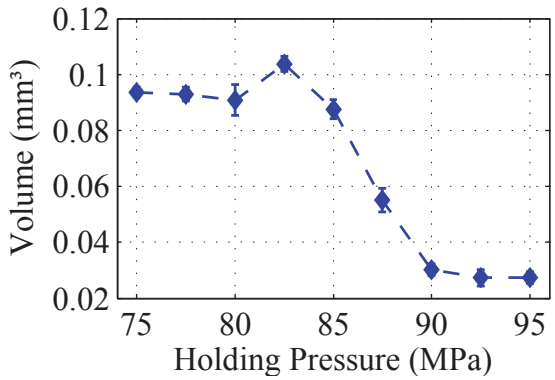

(b)

Figure 4.9: Means of amplitude and volume of the top right sink mark for each test series. In case of outliers outside the 3σ regions around the respective mean, only the worst outlier was omitted for each test series. The error bars are defined by the standard deviation of the inliers.

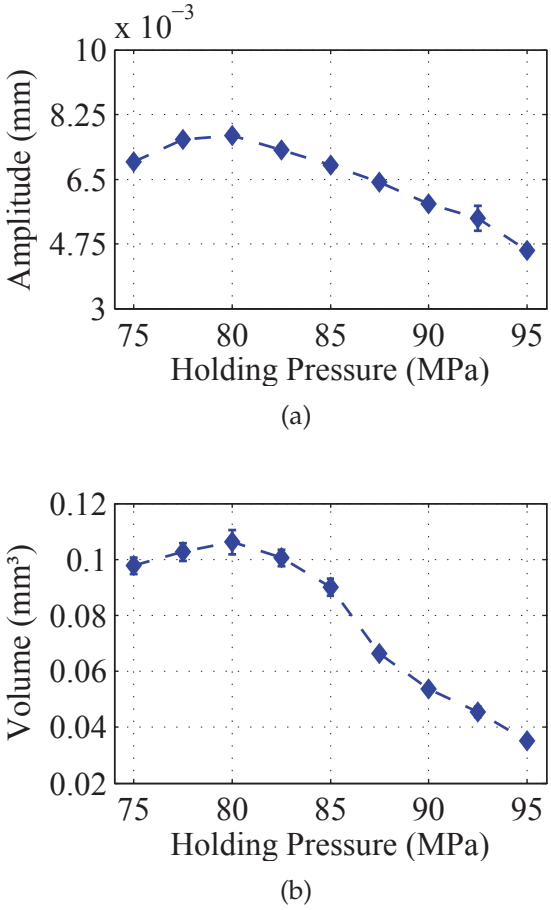

Figure 4.10: Means of amplitude and volume of the bottom right sink mark for each test series. In case of outliers outside the 3σ regions around the respective mean, only the worst outlier was omitted for each test series. The error bars are defined by the standard deviation of the inliers.

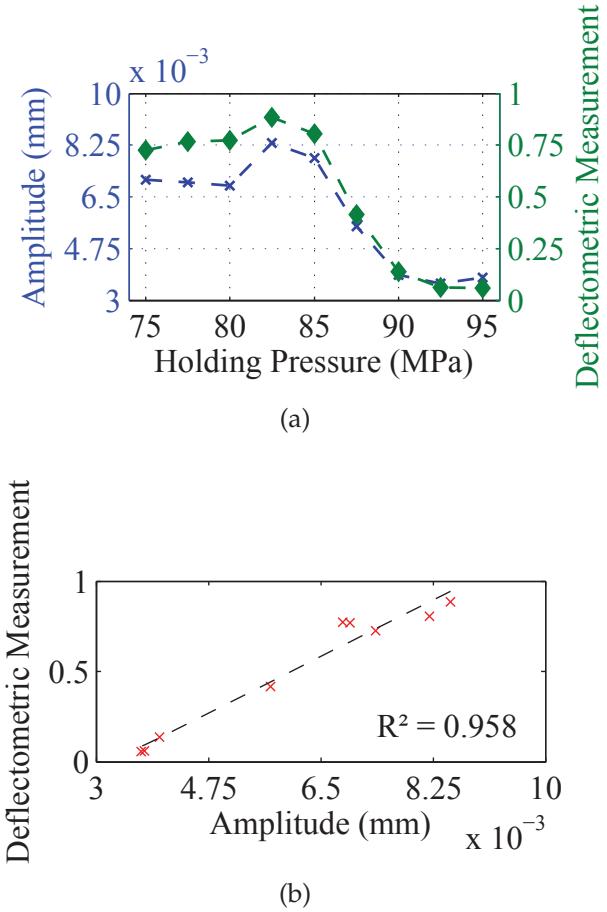

Figure 4.11: Comparison of the topographic measurement of the sink mark amplitudes (x) with the deflectometric measurements (diamonds) for the top right sink mark. b) shows the best linear fit for the plot of the deflectometric measurement as a function of the amplitudes. The R^2 value of the fit is shown to evaluate the correlation between the measurements (see Figure 4.5 and Figure 4.9).

volumes of the top right sink mark. It seems that the integration over the area causes higher stability of the volume feature of the inspected sink marks in comparison to the amplitude feature.

For this reason, the volume of sink marks is considered to be adequate as a feature for the topographical characterization of sink marks. This feature includes the depth and the width of a sink mark, which are the two properties suggested to correlate with sink mark perceptibility [53]. At the same time, the volume is in good accordance with the results of the deflectometric measurements, which are also dependent on the specified evaluation area. Therefore, the volume of sink marks is suggested for future evaluations of deflectometric measurements of sink marks on high gloss parts.

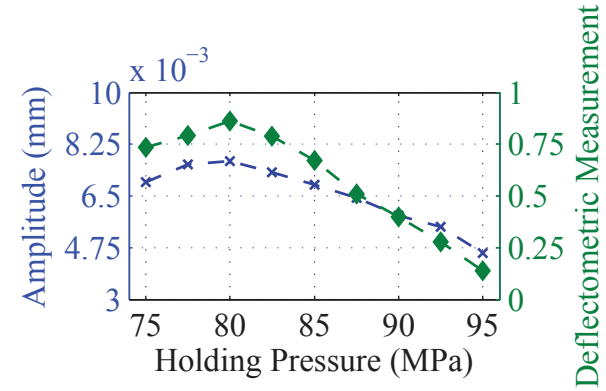

(a)

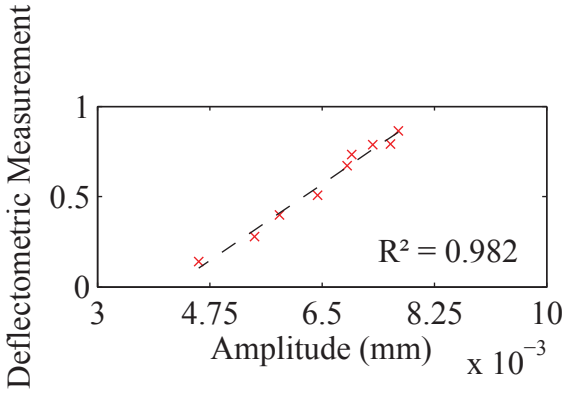

(b)

Figure 4.12: Comparison of the topographic measurement of the sink mark amplitudes (x) with the deflectometric measurements (diamonds) for the bottom right sink mark. b) shows the best linear fit for the plot of the deflectometric measurement as a function of the amplitudes. The R^2 value of the fit is shown to evaluate the correlation between the measurements (see Figure 4.5 and Figure 4.10).

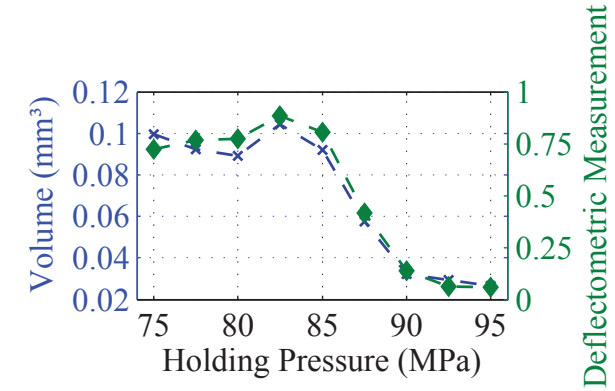

(a)

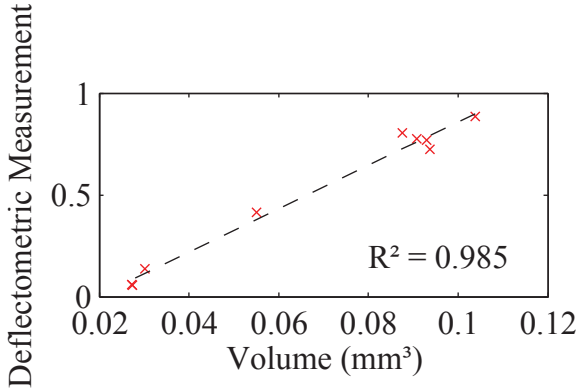

(b)

Figure 4.13: Comparison of the topographic measurement of sink mark volumes (x) with the deflectometric measurements (diamonds) for a) the top right sink mark. b) shows the best linear fit for the plot of the deflectometric measurement as a function of the volumes. The R^2 value of the fit is shown to evaluate the correlation between the measurements (see Figure 4.5 and Figure 4.9).

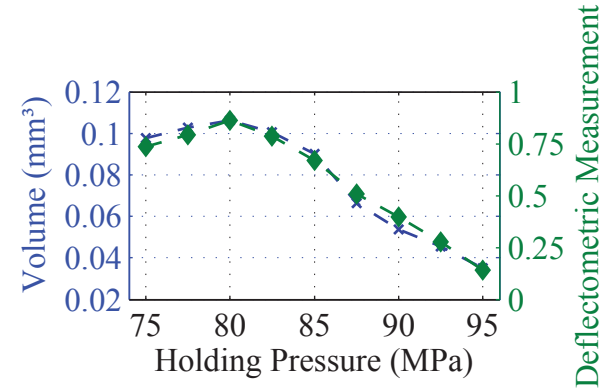

(a)

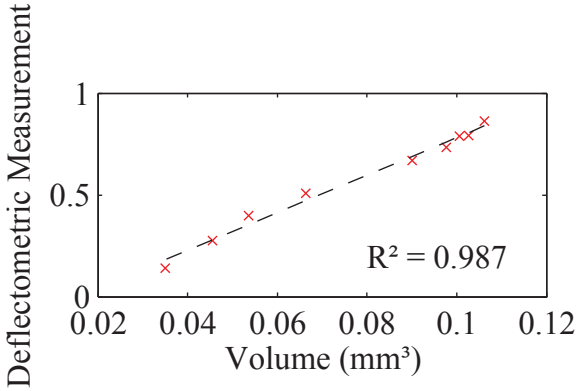

(b)

Figure 4.14: Comparison of the topographic measurement of sink mark volumes (x) with the deflectometric measurements (diamonds) for the bottom right sink mark. b) shows the best linear fit for the plot of the deflectometric measurement as a function of the volumes. The R^2 value of the fit is shown to evaluate the correlation between the measurements (see Figure 4.5 and Figure 4.10).

4.3 INJECTION MOLDED PART "AUTOMOTIVE INTERIOR FRONT PANEL"

4.3.1 *Part Description and Test Series Preparation*

Figure 4.15 shows the "Automotive Interior Front Panel" (courtesy of Schöfer GmbH). This part is manufactured with film insert molding, where a foil which is punched out and thermoformed prior to the process is appositely inserted into the mold prior to the injection molding process. Thereby, the foil defines the quality of the visible surface of the part which is independent of the properties of the plastic material. This simplifies the production of surfaces with decorative print patterns, since they can be applied with ease on the flat foil before it is thermoformed into the required shape to fit into the mold. However, the properties of the foil majorly impact the quality of the final part. For example, too high deep draw ratios lead to pressure inhomogeneities which can result in further stretch of the foil at unfavorable process conditions [67].

The part was chosen because it is designed according to the requirements and fashion movements of recent automotive interior parts. Additionally, an in-line testing site is planned which will be implemented into the process line for this part. This will allow for the evaluation of the method for state-of-the-art front panel designs and the identification of problems which such designs would pose for the inspection under real industrial conditions. Especially two features of the given part complicate the inspection of its surface. First, the surface of the part was defined according to the aesthetics and ergonomic preferences. Therefore, its shape features considerable complexity. This means that the shape of the part's surface cannot be described by one geometry. The part was asymmetric with a high aspect ratio and its surface featured different curvature radii. Therefore, the sensitivity of the measurement was not homogeneous for the whole surface and the identification of suitable measurement positions was difficult. Because of the asymmetry and high aspect ratio of the injection molded part, the distance between the inspected region of the surface and the camera differed considerably for the respective measurement positions which could be achieved with a positioning unit which consisted of rotation units. The application of sinusoidal patterns, as described in Section 2.3, made the total inspection of the surface possible due to their strong invariance to defocussing.

Additionally, some of the curvature radii were close to the limit of a proposed minimal curvature radius of about 7 cm (see Section A.3 for the calculation of this estimate). This estimate was derived from the assumption that a minimal size of the screen's reflection at the surface of

an injection molded part is necessary for, on the one hand, robust calculation of a sink mark's intensity by the measurement of a sufficiently large area of the sink mark's surroundings (see Figure 4.8 for comparison with a topgraphic measurement of a sink mark). On the other hand, the size of the screen's reflection also defines the size of surface area which can be inspected with one measurement (compare with Figure 3.6). For this reason, the number of necessary measurements decreases with increased size of the screen's reflection at the part's surface.

The second challenge was the decorative pattern on the foil. The foil itself forms a black high-gloss surface while the pattern is white and reflects diffusely. This means that the surface areas which are covered by the pattern cannot be detected with sufficient accuracy by deflectometric measurements because the working principle of the method is based on high specular reflection with good clarity of reflected images. Therefore, the pattern disturbs the deflectometric measurement either by creating holes in the measurement mask or by causing artefacts in the measurement. Figure 4.16 shows a measurement image of the part where the inspected sink marks of the part are labelled. It can be clearly seen that the print pattern disturbs the reflection of the sinusoidal pattern. For this reason, interpolation and strong smoothing of the measurement becomes necessary prior to evaluation of the results.

Additionally, only small test series were available. Since the process was already in an optimized stadium, defective parts occurred only incidentally. However, these defective parts damage the image of the manufacturer considerably when detected by a customer in a spot check. For this reason, comparison of parts was achieved by dividing them into five classes, whereby the classification of the parts was carried out by the quality engineers of the manufacturer. In this case, Class 1 included the good parts of the production while Class 5 contained the parts with the most intense sink marks.

4.3.2 *Results of the Deflectometric Measurements*

As was mentioned in the former section, the evaluation of the deflectometric measurement was difficult because of the diffusely reflecting print pattern on the surface. Therefore, the low-pass characteristics of the acquisition of measurement images were increased by defocusing the surface. Additionally, operators for image smoothing were calculated from polynomial base functions where the kernel of the polynomial expansion was larger than the size of the pattern elements in the measurement images. The combination of these two approaches considerably decreased the influence of the print pattern on the evaluation of the measurement results.

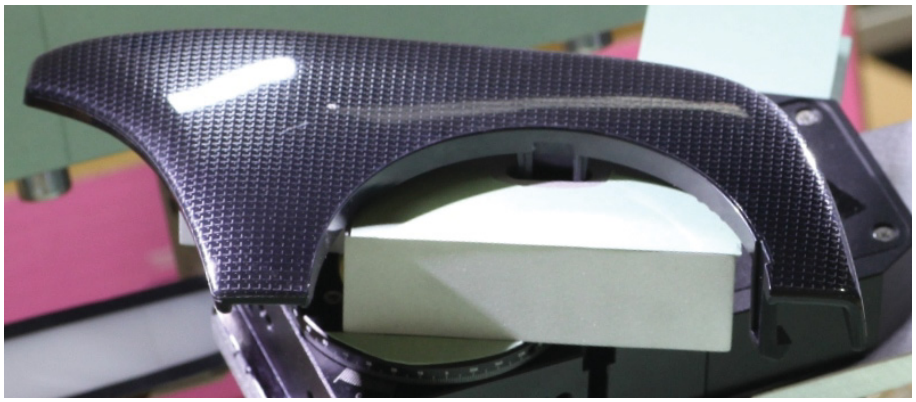

Figure 4.15: Front side of the injection molded part "Automotive Interior Front Panel" (courtesy of Schöfer GmbH) which is enveloped by a rectangle of $18 \times 8\,\mathrm{cm}^2$. The inspected sink marks are shown in Figure 4.16.

However, fine structures of the surface could not be resolved because of the massive smoothing of the measurements. Fortunately, the sink marks in this case are considerably larger than the single elements of the pattern, which ensures that the impact of the smoothing procedures on the response of the sink marks is sufficiently low.

The complex shape of the part made a lot of measurement positions necessary for total surface inspection (see also Figure 3.6). This is problematic for inline inspection because, as was mentioned before, the number of measurement positions strongly increases measurement time. One option to increase the efficiency of the measurements is to concentrate on surface regions where the back side of the part features structures which can cause sink marks. Especially the regions which were marked in Figure 4.16 are prone to sink mark formation. Therefore the examples in this work focus on these three sink marks where the notation in the following figures refers to the name tags in Figure 4.16.

In Figure 4.17 an array of exemplary cropped deflectometric measurements of the three sink marks is displayed where the color code refers to the measured curvature (cyan: flat, blue: convex, red: concave). Accordingly, one example is given for each sink mark and part classification. As can be seen, the sink marks are elongated with a considerable aspect ratio. Nevertheless, the introduced model for sink mark intensity is used for the evaluation of sink mark intensity, although the visibility of such sink marks is no longer invariant to different viewing directions. However, it was considered that at least comparative evaluation of the sink mark intensities is possible, since the viewing direction of the camera in the test setup was the same for all measurements.

In Figure 4.18 the results of sink mark evaluation are shown. Since only a maximum of two parts per class were available, no statistical evaluation

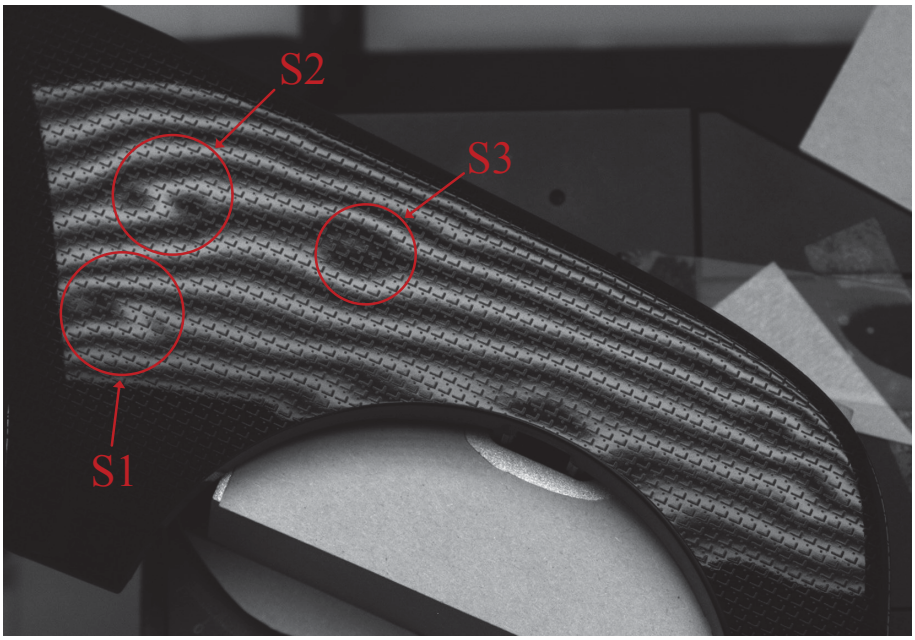

(a)

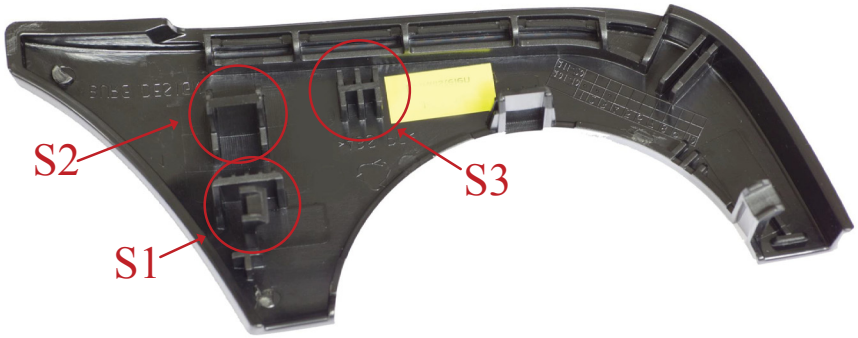

(b)

Figure 4.16: a) Measurement image. The respective sink marks are marked for further reference. Additionally, it can be seen that the print pattern disturbs the reflection of the light pattern. This causes artefacts in the deflectometric measurement. b) Mirror-inverted image of the part's back side . The three structures which cause the sink marks are marked in the same way. The yellow area hides information about the customer of the project partner, like company logos.

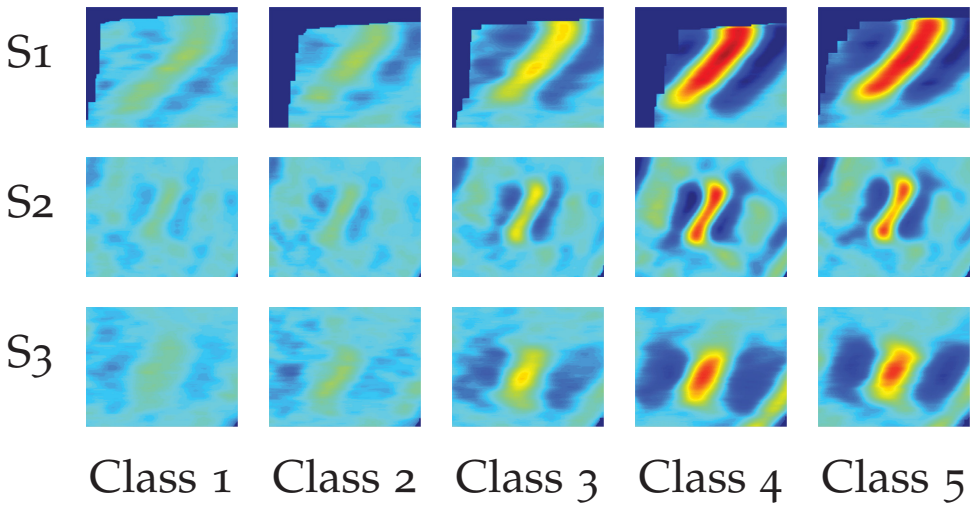

Figure 4.17: Array of examples for deflectometric measurement of sink mark intensities. The parts were categorized in different quality classes by human observers. In this case, Class 1 included the good parts of the production while Class 5 contained the parts with the most intense sink marks. The color code relates to the surface curvature intensity (cyan: flat, red: concave, blue: convex).

of the results was possible. Therefore, no error bars are given and the significance of the results can only be estimated. The distributions of the results for the intensities of the three sink marks for each part give some additional information about the confidence of the measurements. It can be reasoned from these results that the intensities of Class 2 sink marks cannot be significantly differentiated from the sink mark intensities of the Class 1 good parts, since the interferences of the print pattern and the necessary smoothing procedures decreased the sensitivity of the measurement too much to differentiate between the fine differences of those two classes. However, Class 3 is expected to be detected significantly for purpose of quality inspection. Additionally, Class 4 and Class 5 can be significantly differentiated from Class 3. However, Class 4 and Class 5 seem to hardly differ at all. It could be that the sink marks at these intensities are to pronounced for the algorithm to work properly. Additionally, the classification of the parts was carried out by human observers, which might have resulted in a subjective classification. Deeper investigation of the perceptibility of the sink mark has to be done yet.

4.3.3 *Concept of the Implemented Testing Site*

The applicability of the measurement concept will be tested in a real industrial environment in cooperation with Schöfer GmbH. A testing site will be implemented into the injection molding process lines where the

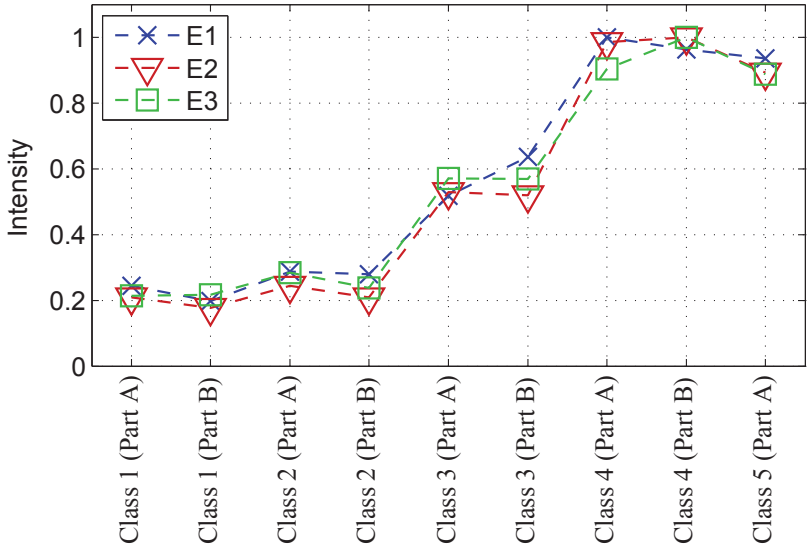

Figure 4.18: Deflectometric measurement of single parts.

given part is produced. The aim is to investigate the challenges which have to be overcome to adapt the testing site which was developed in the laboratory to industrial conditions. The main task was to implement the testing site into the process line without major changes to the setup of the process. The easiest approach for that was to clearly separate the work flows of test setup and injection molding process. The only interaction between the two systems should be the safe transfer of injection molded parts between the systems. In case of the laboratory setup the inspected parts were placed onto the positioning unit manually. For a fully automatic setup, this task will be carried out by the robotic system which is used to eject the manufactured parts from the mold.

Figure 4.19 shows a sketch of the process line at Schöfer GmbH with the testing site. A foil filling station conveys already thermoformed foils to a designed withdrawal position. There, a linear robotic system picks the foils and places them into the mold for the next injection molding cycle. After the cycle is completed, the robotic system picks the manufactured part and places it onto the positioning unit. The postioning unit was redesigned to withstand the increased stress levels in the industrial environment. The rotation units Oriental DG130 for the tilt and Oriental DG85 for the azimuth rotation can withstand moment loads of 50 Nm and 10 Nm, respectively, and have sufficient repetitive positioning accuracy of 0.004°. Figure 4.20 shows the CAD construction of the new positioning unit. Commercially available profile components were used to build the base of the positioning unit to facilitate a more flexible imple-

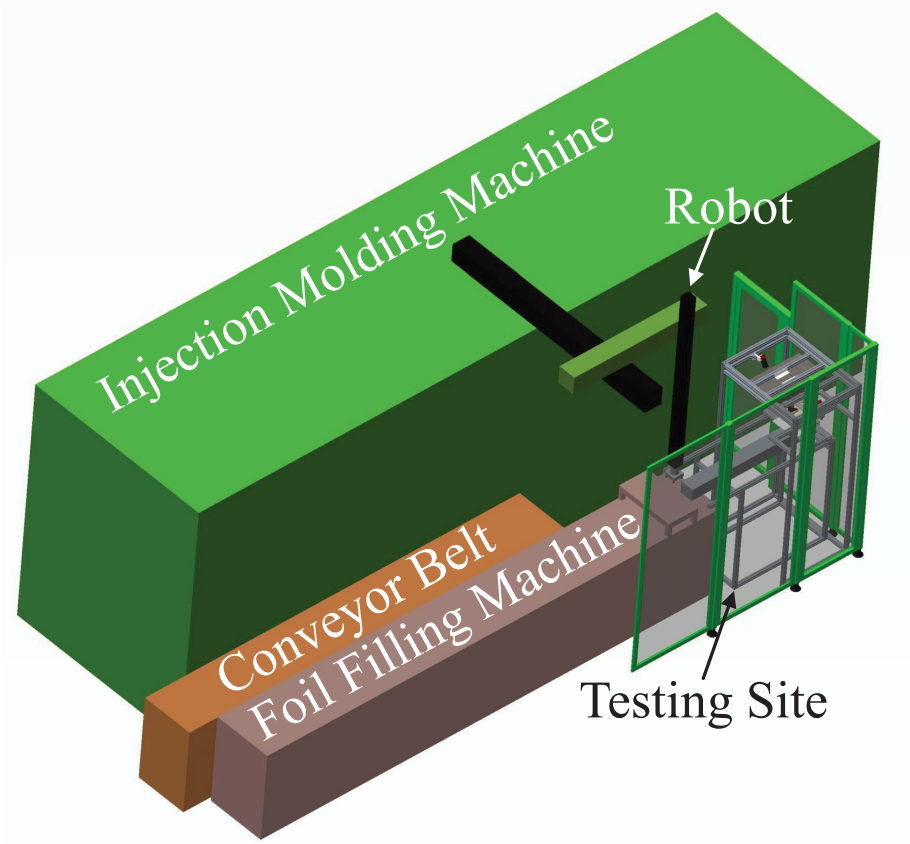

Figure 4.19: Principal sketch of the process line the testing site is implemented in.

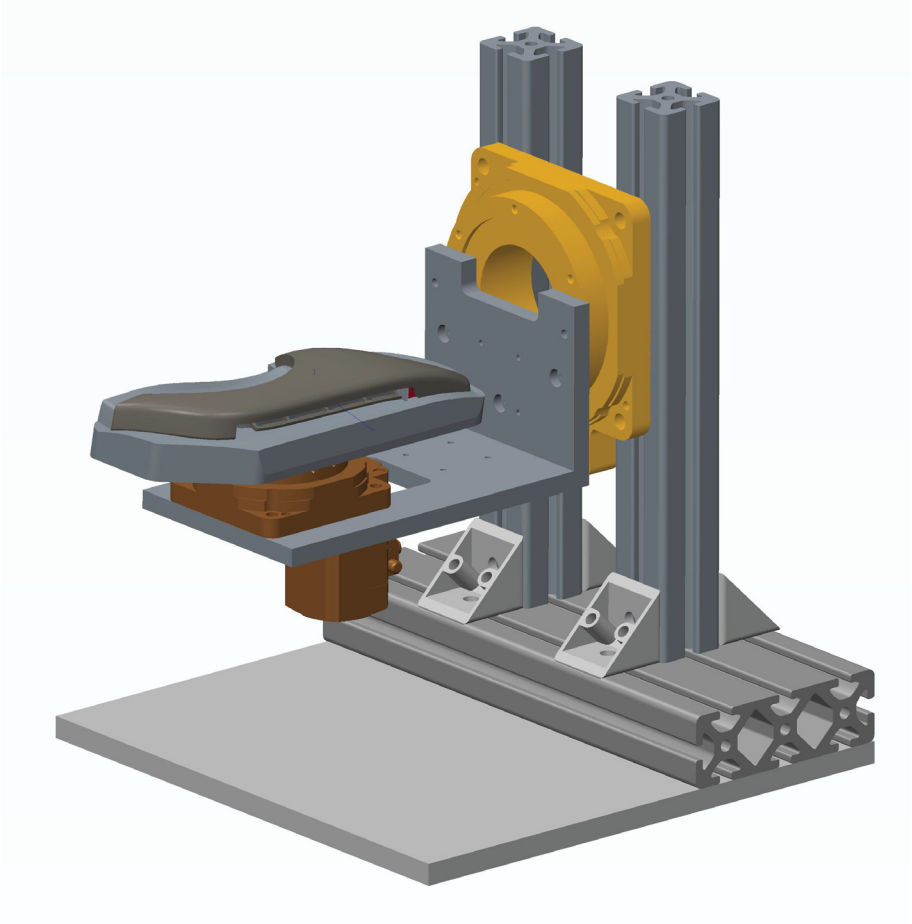

Figure 4.20: CAD-construction of the positioning unit which is adequate for industrial environment. The CAD data of the rotation units was obtained from [96] and [97].

mentation of the unit into the testing setup. The connection between the rotation units was designed to ensure that the surface of the part and the tilt axis of the positioning unit coincide. As was mentioned in Section 3.3, this reduced the influence of part positioning on the distance between surface and camera considerably.

Figure 4.21 shows the testing site in the process line. As can be seen in the figure, a linear unit is used to move the positioning unit between the position where the linear robotic system inserts the part and the measurement position inside the testing site. At the measurement position the part is positioned below the cameras and light sources according to the programmed measurement routine. Deflectometric measurements are used for sink mark detection while additional methodologies are used to detect morphological defects on the surface, such as scratches or pattern defects. After the measurement sequence the positioning unit is moved outside the testing site. The part is picked up by the robotic system and

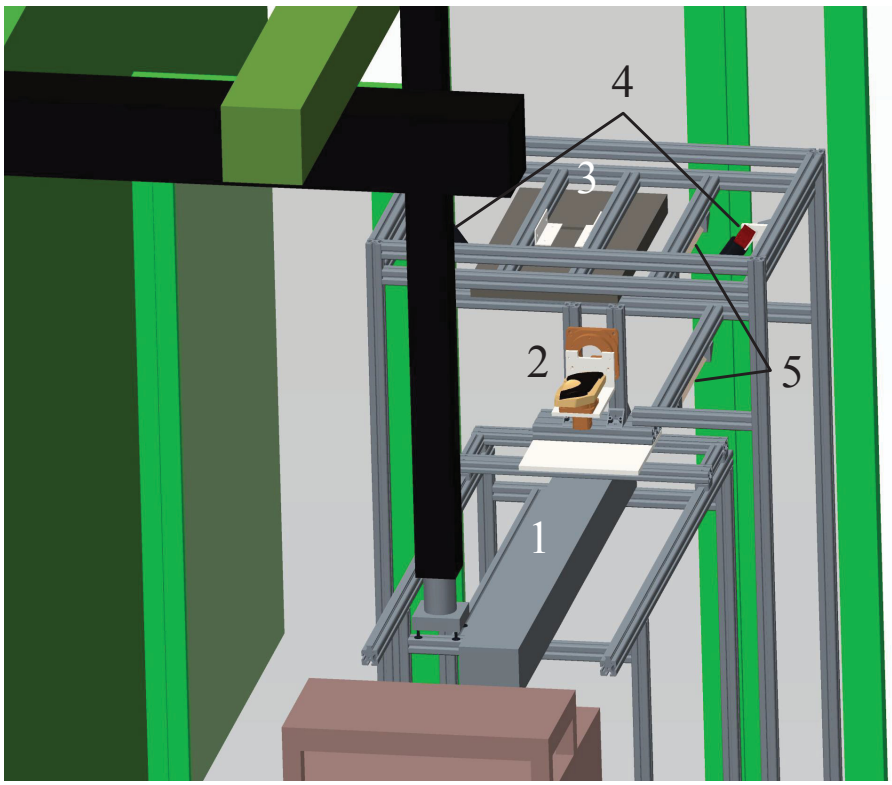

Figure 4.21: Testing site in the process line (Figure 16). (1) Linear system, (2) positioning unit, (3) screen, (4) cameras and (5) diffuse light sources for detection of morphological defects (e. g. scratches). The second camera at the right is used for the detection of morphological defects in surface texture in addition to the deflectometric measurement.

is either placed on the conveyor belt or thrown away, depending on the result of the inspection.

The process line will be ready for testing in the mid of September. The performance of the testing site will be evaluated by quality engineers of Schöfer GmbH in cooperation with the Polymer Competence Center Leoben GmbH.

5

OUTLOOK

5.1 IMPROVEMENT OF DEFLECTOMETRIC MEASUREMENT SPEED

One of the major drawbacks of the method introduced in this work is the comparatively high measurement time. Complex surfaces such as the part in Section 4.3 need several measurement cycles to provide full surface inspection. For this reason, total measurement time is still too long for 100 % in-line inspection of such parts. The time for image acquisition forms a major factor for the long measurement time because of the high number of images which are necessary for the deflectometric measurement.

Even a slight decrease of the acquisition time due to, for example, higher light intensity of the structural light source or higher sensitivity of the used camera would reduce the duration of a measurement cycle considerably. For comparison, the deflectometric test setups, which are proposed in this work, require about 0.25 s per image which mainly includes shutter time besides the time for image storage. Given the application of the 4-bucket-algorithm and four iterations of the algorithm, the deflectometric measurements require 32 images per measurement, which in turn means that each measurement takes about 8 s alone for image capture. Since complexly shaped parts require several measurements, the total measurement time including image processing and part handling could be too long for in-line quality inspection of injection molded parts. For example, the part "Automotive Interior Front Panel" requires at least two measurements or 16 s for image capture to inspect all areas of its surface which are prone to sink mark formation. With a cylcle time of about 72 s for the manufacture of two parts in one cycle, this leaves only about 20 s per part for image processing and analysis, part handling and additional inspection methods, for example texture analysis for the detection of morphological defects.

Therefore, it is necessary to decrease image capture time for in-line applications of deflectometric measurements. For example, if shutter time is decreased by 0.1 s, the duration of a single deflectometric measurement cycle of the introduced test setup will be reduced by about three seconds. However, cameras with high sensitivity are costly. On the other hand, acquisition time can also be decreased by application of brighter structured light sources, but such light sources which are based on high power LEDs are comparatively expensive. Therefore, the screens of tablet PCs, which

have become common in recent years, would be a cheaper option. Since the screens of tablet PCs are optimized for operation in full sunshine, the intensity of their screens features high intensity. The increasing establishment of strategies for the manufacture of such screens could decrease the price of high intensity screens in future. Besides possible other high intensity structured light sources, such screens could help to decrease image acquisition time considerably.

Another approach would be parallel computing for image acquisition. Recently, electronic devices were developed which can be applied as low cost, low benchmark mini-computers. Examples for off-the-shelf devices are the BeagleBoard [9] and the Raspberry Pi [105]. These devices, which feature low price and small physical dimensions compared to conventional computers, could be used to decentralize the measurement process. An ensemble of cheaper industrial cameras, each controlled by such a mini-computer, would allow for simultaneous image acquisition, while a conventional measurement PC would serve as a central server for the mini-computers and would perform the main calculations and data analysis. However, such an approach would also pose additional challenges. First, the number of devices with asynchronous behavior to each other would increase with each additional camera in such a measuring setup. Therefore, a suitable I/O-connection between the embedded devices, the light sensor on the monitor and the server PC would have to be established to maintain the measurement sequence.

Additionally, the mapping function, which was expressed in Equation 2.29 in Section 2.3.2, is dependent on the viewing direction of the camera. Therefore, the calibration of the screen and the camera position becomes necessary to ensure comparability between measurements. The inner and outer parameters of the camera according to projective geometry (e.g. [51]) can be calculated using the Matlab toolbox provided by Buguet [14]. The algorithms by Zhang [125, 126] can be used for calibration of the relative positions of the cameras and screen with a mirror and checkerboard patterns on the screen. This approach was improved by Werling, who proposed a method for the application of Zhang's algorithms where sinusoidal patterns and the mapping functions from several deflectometric measurements of the mirror can be used instead of the analysis of the checkerboard patterns [119]. This approach would be advantageous, since it would provide sub-pixel accuracy while using the deflectometric measurement process of the test setup.

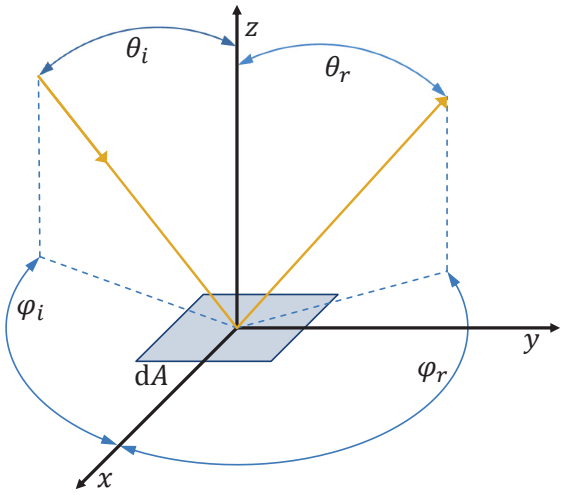

Figure 5.1: Schematics for the expression of the BRDF. The parameters of this function for a given surface element dA are the angles θ_I and φ_I of the direction of incident light, as well as the angles θ_R and φ_R of the viewing direction (sketched according to [86]).

5.2 ERROR ESTIMATION AND IMPROVEMENT OF THE INTENSITY MODEL

In this work, a model for the sink mark intensity was introduced. In Section 4.2 the results which were calculated from deflectometric measurements according to the introduced intensity model were compared to topographical measurements of the inspected sink marks. The reproducibility of the theoretical model itself can be estimated from the measurement results if the influences of part production and test setup are known. Its reliability can be evaluated with assessments studies about sink mark perceptibility. The variations of part production for a given setting of process parameters can be measured using established methods. One option would be to weigh the parts to evaluate process stability. Another option would be topographic measurements of sink marks. In this work, for example, the volume of sink marks was suggested as a feature for sink mark comparison.

Another option for the description of reflectance properties of surfaces would be the BRDF (bi-directional reflection distribution function), which was introduced by the National Bureau of Standards [86]. This function contains comprehensive information about the reflection behavior of surfaces. It is a four-dimensional function for the reflected light intensity which depends on light incidence and viewing direction (see Figure 5.1).

The comprehensive measurement and analysis of the BRDF of a given material takes a large amount of time and causes high computational cost. However, there exist several approaches for practical measurement of the

BRDF in literature [27, 32, 52]. These approaches allow the comprehensive description of reflection on the measured surface with only minor simplifications of the problem. Nevertheless, the resulting volume of data is considerable because the BRDF is a four-dimensional function. Therefore, several models were introduced to approximate the BRDF while keeping the computational load low at the same time (e.g. [23, 117]).

The reflective surface properties of the parts, especially gloss, can be measured by using an off-the-shelf gloss meter, if possible, or gloss measurement methods which were developed at the PCCL [37, 44]. Such models are used to predict the ratio of specular reflection and diffuse reflection due to material inhomogeneities and surface roughness. The results of such simulations could be used to predict the maximum possible resolution of deflectometric measurements for a given part's surface scattering. This surface property defines the low pass filtering of the reflection of the structured light source. These measurements together would allow the estimation of part variance and also facilitate the pooling of selected parts into series with inherent low variance of part properties.

Additionally, it would be convenient to also manufacture parts with different colors to evaluate the influence of different colors on the ratio of diffuse and specular reflection from plastics surfaces in the course of these BRDF measurement. As mentioned in Section 4.1, only black high-gloss parts were inspected because of the small amount of diffuse reflection from those surfaces. However, such an analysis would give important information about the applicability of the deflectometric measurements for additional colors and would allow for the prediction of the influence of a specific color on the reliability and resolution of the measurements.

Comprehensive error analysis of deflectometric measurements were introduced by Werling [119] and Höfer et al. [60]. They estimated the error of the deflectometric measurement from the non-perfect imaging by the camera lens and camera electronics as well as the scattering behavior of the surface. Additionally, they investigated the influence of the geometrical arrangement of the test setup components on the deflectometric measurement results. For example, Werling concluded that the relative error for curvature estimation could be lower than 5 % while unfavorable test arrangements could lead to relative curvature errors above 10 %. Such high curvature errors lessen the resolution of sink mark intensity measurements considerably. Analyzing the performance of the deflectometric measurement would allow for the estimation of error influence of part properties variance on the variance of the measurement results of the sink mark intensity model.

The correlation between the model results and the perceptibility of sink marks by human observers could be investigated with assessment studies.

Such assessment studies could also be extended by additional inclusion of parts with different reflection behavior. This would allow the implementation of additional feature parameters into the model which describe the interaction between reflection behavior and sink mark perceptibility. Thereby, the reflection behavior of the part could be expressed with a BRDF model.

5.3 FASTER METROLOGICAL RECONSTRUCTION OF HIGH-GLOSS PARTS

In this work, phase measuring deflectometry was used for sink mark detection on high-gloss surfaces. Another application for this method is metrological reconstruction of such surfaces. Thereby, screen-camera calibration as explained in Section 5.1 is essential for correct calculation of a surface's normal vector field from the mapping function between screen and camera. However, the shape of the normal vector field is ambiguous, since its calculation is dependent on the distance of the surface to screen and camera. Additional information is necessary because only the start points of the light beam trajectories in the screen area and end points in the camera sensor area are known from the deflectometric measurement itself. For this reason, additional information has to be employed to resolve the ambiguities of the normal vector field measurement. For example, the ambiguities can be resolved with deflectometric measurements using a stereo camera approach. In doing so, two deflectometric measurements of the same surface area are carried out by two different cameras[1]. The differences between the two measurements minimize for the correct solution of the normal vector field [62, 104, 119].

Since the normal vector field of the surface correlates to the surface gradients, the metrological reconstruction of high-gloss surfaces is an integration problem which could be improved and accelerated by the application of polynomial base functions. Harker and O'Leary used such an approach to reconstruct surfaces from measurement results from photometric stereo, which also contain the gradient field of a measured surface [49]. They were able to prove that their approach was considerably faster than state-of-the-art methods. The implementation of a similar algorithm for surface reconstruction from deflectometric measurements could facilitate the inline reconstruction of high-gloss surfaces.

[1] In contrast to the proposed approach in Section 5.1, where one of the cameras is used for the detection of morphological cameras.

5.4 SIMULATION OF SINK MARK PERCEPTIBILITY

Injection molding simulation, which include among others cavity filling, shrinkage and warpage prediction,before actual construction of the mold can help with identifying possible design flaws of a mold. Such flaws would, for example, facilitate the formation of sink marks and other surface defects which would lower the quality of the part. In so doing, costs from redesigning the mold can be avoided beforehand. However, the severity of sink marks visibility on high-gloss parts, where the perceptibility basically reduces to the distortion of surface reflection, could be further simulated by implementation of the proposed sink mark intensity models into the injection molding simulations.

Such an approach would need 3D data of the part simulation, including depth and area of possible sink marks. For example, the STL data type would be suitable for further analysis, since it represents surface data as a mesh where the data points are assigned as the vertices of triangular faces, while the normal vectors of each face is stored in the data. Using algorithms from differential geometry [7, 30], the curvature of the part at any given location on the surface can be calculated, provided that the density of the mesh is sufficient. The model introduced in this work uses curvature as one of the main feature parameters. Therefore, it would support the quantitative evaluation of sink mark perceptibility from simulated data.

Qualitative evaluation of sink mark perceptibility to human observers could be enabled by applying the expression of the mapping function in Equation 2.37 in Section 2.3.2. In this equation, the mapping from a structured light source on a camera sensor via the inspected surface is described. The calculation of the mapping function requires the interpolation of the vertices and normal vectors of the STL file in such a way that a point cloud is calculated where the corresponding normal vectors are allocated to each point.

Sink marks on high-gloss parts are identified by looking at distortions in the reflection of known patterns from the part's surface. Therefore, a virtual structured light source which produces a defined light pattern has to be simulated next where the position of this light source as well as a local coordinate system for each "pixel" of the light source has to be defined. The pinhole camera model, which is mathematically defined in projective geometry (e.g. [51]), can be applied to calculate the imaging of the reflection of the light source from the part's surface while Equation 2.29 in Section 2.3.2 can be used to calculate which part of the surface reflects the light source into the virtual camera and how the shape of the surface distorts the reflection. By investigating the simulated image, a human ob-

server could identify a possible sink mark because of the distortion it causes in the pattern. Additionally, the knowledge about the BRDF of the surface would allow the simulation of haze which could then be applied to decrease the clarity of the reflection. This would allow for simulation of the reflection closer to real-life experience.

6

CONCLUSIONS

In this work, phase measuring deflectometry was adapted for the detection of visually perceptible sink marks on high-gloss surfaces of injection molded thermoplastic parts for flat as well as curved surfaces. In a testing site a light pattern which is produced by a structured light source is reflected into the camera via the inspected surface of an injection molded part. Since the pattern is known, information about the shape of the inspected surface can be derived from the distortions of the pattern. Because the principle of phase measuring deflectometry is based on reflections with high clarity, the method is suitable for inspection of high-gloss surfaces.

An off-the-shelf computer screen was used as a cheap and convenient structured light source together with industrial cameras to build a deflectometric setup. This setup was extended with an automatic unit for part positioning to allow full inspection of curved parts. This unit was an assembly of two rotational units to adjust the tilt and the azimuth of the inspected parts for the measurement. Their resolutions of 0.225° and 1 arcsec, respectively, were considered as acceptable for the measurements. Additionally, the movement of the surface out of the focus plane of the inspecting camera was minimized by ensuring that the surface of the inspected part was close to the tilt axis of the positioning unit.

The deflectometric measurement results are proportional to the first derivative of the surface. Therefore, surface curvature which was used for sink mark detection could be acquired efficiently with only one derivation. This ensures low computational cost and a good signal to noise ratio. Additionally, discrete orthonormal polynomial base functions were shown to be a viable means for numeric processing of the measurements. The application of this mathematical algorithm was advantageous, since directional differentials of surfaces can be approximated with high quality even if noise is present in the data. Additionally, this algorithm facilitates the filtering and smoothing of non-periodic data unlike most low-pass filters, which are often derived from Fourier transformation. For this reason, strong smoothing could be applied on the measurement results to approximate the unperturbed surface of inspected parts. Subtraction of this approximation from the original measurement increased the distinctness of the sink marks in processed images. This made the application of a “Golden Sample” unnecessary for sink mark evaluation.

In this work, only black high-gloss parts were investigated because of the low amount of diffuse reflection which is advantageous for deflectometric measurements. However, the influence of color on the performance of deflectometric measurements was not evaluated. BRDF measurements of colored surfaces are planned in future to get information about the ratio of diffuse and specular light for common colors to estimate the applicability of deflectometric measurements for a given color.

Nevertheless, two practical parts, a "Coffee Maker Front Panel" and an "Automotive Interior Front Panel", were used in the measurements. Test series of the parts were manufactured to evaluate the performance of the introduced testing site. The holding pressure which is an important parameter for sink mark visibility was incrementally decreased to produce test series with increasing sink mark intensity. The experimental results of the deflectometric measurements correlated with the expected increase of sink mark intensity due to the decrease of the initial holding pressure and the in turn decreased shrinkage compensation during manufacture. The sink mark intensity was evaluated with a mathematical model which calculated sink mark intensity from sink mark curvature and area.

Additionally, topographical measurements of the sink marks were carried out for the "Coffee Maker Front Panel". The measurements were fitted with a model for sink mark shape which is based on a superposition of the Gaussian bell function with the platykurtic bump bell function. The fit facilitated the calculation of amplitude and volume of the inspected sink marks. Comparison between these topographic features and the deflectometric measurements showed good correlation. Especially sink mark volume was a robust parameter for the evaluation of sink marks on high gloss parts and featured extraordinary conformance with the deflectometric measurements. Additionally, deflectometric and topographic measurements were compared to allow for rough estimates of the relative error and resolution of the deflectometric measurement. The estimation gave 15 % for the relative error and 1 µm for the resolution of sink mark depth.

The part "Automotive Interior Front Panel" featured a more difficult geometry and also a diffusely reflecting print pattern which interfered with the deflectometric measurement. The application of sinusoidal light patterns for deflectometric measurements as well as data smoothing based on polynomial base functions facilitated the inspection of its sink marks. Additionally, the part featured several different curvatures with strong regional differences of surface curvature which made the definition of suitable measurement positions difficult. Additionally, some regions of the part's surface featured small curvature radii which resulted in a small size of the screen's reflection from the part's surface. The small size of

the screen's reflection decreased the size of surface area which can be inspected with one measurement. It was estimated that the curvature radii should not be smaller than about 7 cm to allow robust calculation of sink mark intensity, which is facilitated by measurement of a conveniently large area of the sink mark's surroundings, and efficient inspection of the part's surface due to a comparatively small number of necessary measurements.

Summing up, the main contributions of this thesis are:

1. the successful evaluation of the phase measuring deflectometry for the detection of sink marks. The proposed part positioning unit enables total inspection of curved parts without application of costly part handling tools, like multi-axial robots, which even require additional safety measures. The application of such a positioning unit also allows for the comparatively simple integration of the testing site into an industrial injection molding line by using the linear robotic handling system which is usually applied for such a line for part placement into the testing site.

2. the development of a model for the analysis of the deflectometric measurement. This model allows for the calculation of sink mark intensity as feature parameter for sink mark evaluation.

3. the implementation of polynomial base functions into the data processing of deflectometric measurements. The application of such functions allows for the homogenization of the measurements without the application of a "Golden Sample".

4. the introduction of the feature parameter sink mark volume which correlates the topographical shape of a sink mark with its visibility. The feature parameter is calculated from a model which is proposed in this work and is based on distribution functions. This feature parameter is proposed for the evaluation of at least point-shaped sink marks on high-gloss surfaces.

Based on the results of this work, an inline application of the testing site was planned for implementation into an industrial injection molding process line for the "Automotive Interior Front Panel". The testing site was adapted to be more robust under industrial conditions. Especially the automatic positioning unit was redesigned to withstand higher moment loads. The installation of the testing site will happen at a project partner of the PCCL in the course of a joined project. The research conducted in the project will allow for the investigation of the challenges which have to be overcome to adapt the testing site, which was developed under laboratory conditions, for an industrial environment.

A

APPENDIX

A.1 THEORY OF PHASE SHIFTING ALGORITHMS

A.1.1 *Derivation*

The comprehensive derivation which is introduced in this section is based on the work of de Groot [35]. The phase shifting algorithms are derived from a continuous 1-dimensional approach without loss of generality. This approach can be expanded to two dimensions by adding an additional dimension to the equations in this section. In doing so, the equation for the phase intensity in one dimension is given by

$$g(\Theta, t) = F + G \cdot \cos(\Theta + \Phi(t)). \tag{A.1}$$

g is the measured intensity, Θ is the phase information and t is the parametrisation of the phase shift Φ. This equation can be transformed into the following form

$$g(\Theta, t) = A\,(1 + C \cdot \cos(\Theta + \Phi(t))) \tag{A.2}$$

with $A = F$ the amplitude of the intensity measurement and $C = G/F$ the measured contrast in the measurement. The Fourier transformation is then used to convert the dependence of the intensities on the parametrisation factor t into a frequency dependence according to

$$G(\Theta, \nu) = \mathcal{F}\,(g(\Theta, t)) = \int_{-\infty}^{\infty} w(t) A\,(1 + C \cdot \cos(\Theta + \Phi(t)))\exp(-i2\pi\nu t)\,dt. \tag{A.3}$$

The pre-factor for the Fourier transformation was assumed as 1, since the sought results are ratios of Fourier transformations where any constant prefactors are canceled. The window function $w(t)$ defines a con-

finement such as the dimensions of a screen. Assuming that the phase shift Φ is continuous (without singularities) and linear

$$\Phi(t) \simeq 2\pi\nu_0 t \tag{A.4}$$

the Fourier transformation can be calculated in the following manner

$$\begin{aligned} G(\Theta,\nu) = & \underbrace{\int_{-\infty}^{\infty} w(t) A \exp(-2\pi\nu t)\,dt}_{I} + \\ & + \underbrace{\int_{-\infty}^{\infty} w(t) A\, C \cdot \cos(\Theta + 2\pi\nu_0 t) \exp(-i2\pi\nu t)\,dt}_{II} \end{aligned} \tag{A.5}$$

where

$$I = A \cdot W(\nu) \tag{A.6}$$

and

$$\begin{aligned} II &= A\, C \int_{-\infty}^{\infty} w(t)\, \cos(\Theta + 2\pi\nu_0 t) \exp(-i2\pi\nu t)\,dt \\ &= A\, C \int_{-\infty}^{\infty} w(t)\, \frac{1}{2} \left[\exp(i\Theta + i2\pi\nu_0 t) + \right. \\ &\quad \left. + \exp(-i\Theta - i2\pi\nu_0 t)\right] \exp(-i2\pi\nu t)\,dt \\ &= \frac{1}{2} A\, C \int_{-\infty}^{\infty} \exp(i\Theta)\, w(t)\, \exp(-i2\pi(\nu - \nu_0)t) + \\ &\qquad + \exp(-i\Theta)\, w(t)\, \exp(-i2\pi(\nu + \nu_0)t)\,dt \\ &= \frac{1}{2} A\, C\, \left[W(\nu - \nu_0)\exp(i\Theta) + W(\nu + \nu_0)\exp(-i\Theta)\right]. \end{aligned} \tag{A.7}$$

Addition of Equation A.6 and Equation A.7 gives

$$G(\Theta,\nu) = A\left\{W(\nu) + \frac{1}{2}\,C\,[W(\nu-\nu_0)\exp(i\Theta) + \right.$$
$$\left. +\;\; W(\nu+\nu_0)\exp(-i\Theta)]\right\} \tag{A.8}$$

With consideration of

$$W(\nu_0) = 0 \tag{A.9}$$

and

$$W(2\nu_0) = 0\,, \tag{A.10}$$

Equation A.8 becomes at $\nu = \nu_0$

$$G(\Theta,\nu_0) = \frac{1}{2}\,B\,C\,W(0)\exp(i\Theta) \tag{A.11}$$

This relation allows the calculation of Θ in the following manner

$$\Theta + \text{const.} = \arctan\frac{\Im\{G(\Theta,\nu_0)\}}{\Re\{G(\Theta,\nu_0)\}} \tag{A.12}$$

The finite discrete approximation of the window function $w(t)$ becomes for the discrete phase shifts Φ_j

$$w(t) = \sum_j w_j\delta\left(t - \frac{\Phi_j}{2\pi\nu_0}\right) \tag{A.13}$$

where δ is the Dirac Function. The Fourier transformation can be calculated again with the discrete window function

$$
\begin{aligned}
G(\Theta, \nu_0) &= \int_{-\infty}^{\infty} \sum_j w_j \delta\left(t - \frac{\Phi_j}{2\pi\nu_0}\right) g(\Theta, t)\, \exp(-i2\pi\nu_0 t)\, dt \\
&= \sum_j g(\Theta, \Phi_j)\, w_j\, \exp\left(-i\frac{2\pi\nu_0\Phi_j}{2\pi\nu_0}\right) \\
&= \sum_j g_j\, w_j\, \exp(-i\Phi_j) \qquad \text{(A.14)}
\end{aligned}
$$

For this discrete approach, the phase information Θ can again be calculated with Equation A.8. Nevertheless, for simplicity's sake, the real and the imaginary part of the window function respectively can be substituted with

$$c_j = \Re\left\{w_j\, \exp(-i\Phi_j)\right\} \qquad \text{(A.15)}$$

$$s_j = \Im\left\{w_j\, \exp(-i\Phi_j)\right\} \qquad \text{(A.16)}$$

$$\qquad \text{(A.17)}$$

The parameters w_j can be calculated from c_j and s_j with

$$w_j = s_j\, \sin(-\Phi_j) + c_j\, \cos(\Phi_j) + i\left[s_j\, \cos(\Phi_j) - c_j\, \sin(-\Phi_j)\right] \qquad \text{(A.18)}$$

Proof:

$$
\begin{aligned}
w_j &= s_j\, \sin(-\Phi_j) + c_j\, \cos(\Phi_j) + i\left[s_j\, \cos(\Phi_j) - c_j\, \sin(-\Phi_j)\right] \\
&= -\Im\left\{w_j\, \exp(-i\Phi_j)\right\} \sin(\Phi_j) + \Re\left\{w_j\, \exp(-i\Phi_j)\right\} \cos(\Phi_j) + \\
&+ i\left[\Im\left\{w_j\, \exp(-i\Phi_j)\right\} \cos(\Phi_j) + \Re\left\{w_j\, \exp(-i\Phi_j)\right\} \sin(\Phi_j)\right] \\
&= i\,\Im\left\{w_j\, \exp(-i\Phi_j)\right\} \exp(i\Phi_j) + \Re\left\{w_j\, \exp(-i\Phi_j)\right\} \exp(i\Phi_j) \\
&= w_j
\end{aligned}
$$

Equation A.18 can be used to evaluate established phase shifting algorithms where the parameter c_j and s_j are already known, since Equation A.18 has to be fullfilled for valid algorithms. Additionally, these parameters have to obey relations which are derived from the assumptions in Equation A.9 and Equation A.10. First, Equation A.9 is the condition for the DC term of the Fourier transformation in Equation A.8 and is satisfied in the following manner

$$
\begin{aligned}
W(\nu_0) &= 0 \\
&= \int_{-\infty}^{\infty} \sum_j w_j \delta\left(t - \frac{\Phi_j}{2\pi\nu_0}\right) \exp(-i2\pi\nu_0 t)\, dt \\
&= \sum_j w_j \exp(-i\Phi_j) \\
&= \sum_j \Re\left\{w_j \exp(-i\Phi_j)\right\} + i \sum_j \Im\left\{w_j \exp(-i\Phi_j)\right\}
\end{aligned}
$$

$$
\Rightarrow \quad \sum_j c_j = 0 \quad \text{and} \quad \sum_j s_j = 0 \tag{A.19}
$$

Equation A.10 describes the condition that the terms of the Fourier transformation of the intensities which contain the negative frequency portion of the spectrum should vanish at the modulation frequency ν_0. This condition is satisfied in the following manner.

$$
\begin{aligned}
W(2\nu_0) &= 0 \\
&= \int_{-\infty}^{\infty} \sum_j w_j \delta\left(t - \frac{\Phi_j}{2\pi\nu_0}\right) \exp(-i2\pi \cdot (2\nu_0) \cdot t)\, dt \\
&= \sum_j w_j \exp(-2i\Phi_j) \\
&= \left[\sum_j \Re\left\{w_j \exp(-i\Phi_j)\right\} + i \sum_j \Im\left\{w_j \exp(-i\Phi_j)\right\}\right] \cdot \\
&\qquad \cdot [\cos(\Phi) - i\sin(\Phi)] \\
&= \left[\sum_j c_j \cos(\Phi) + \sum_j s_j \sin(\Phi)\right] + \\
&\qquad + i\left[\sum_j s_j \cos(\Phi) - \sum_j c_j \sin(\Phi)\right]
\end{aligned}
$$

$$
\begin{aligned}
\Rightarrow \quad & \sum_j c_j \cos(\Phi) = -\sum_j s_j \sin(\Phi) \quad \text{and} \\
& \sum_j c_j \sin(\Phi) = \sum_j s_j \cos(\Phi)
\end{aligned} \tag{A.20}
$$

Further simplifications of the phase shifting algorithms are possible for the special case of a real and symmetric window function which is assumed to be always true for deflectometric measurement setups. Equation A.16 and Equation A.17 are simplified to

$$c_j = w_j \cos(\Phi) \tag{A.21}$$

$$s_j = -w_j \sin(\Phi) \tag{A.22}$$

$$\tag{A.23}$$

Since the screen of a deflectometric setup normally defines the window function, the parameters w_j become either 1 (within screen) or 0 (outside of screen). This final simplification gives the general equation for the calculation of phase information in deflectometric setups.

$$\Theta + \text{const.} = \arctan\left[-\frac{\sum_j g_j \sin(\Phi_j)}{\sum_j g_j \cos(\Phi_j)}\right] \tag{A.24}$$

A.1.2 *Examples for Phase Shifting Algorithms*

4-Bucket-Algorithm $\Phi_j = 0, \pi/2, \pi, 3\pi/2$

$$\Theta + \text{const.} = \arctan\left(\frac{g_3 - g_1}{g_0 - g_2}\right) \tag{A.25}$$

3-Bucket-Algorithm $\Phi_j = 0, 2\pi/3, 4\pi/3$

$$\Theta + \text{const.} = \arctan\left(\sqrt{3}\frac{g_2 - g_1}{2\,g_0 - g_1 - g_2}\right) \tag{A.26}$$

6-Bucket-Algorithm $\Phi_j = 0, \mathrm{pi}/3, 2\pi/3, \mathrm{pi}, 4\pi/3, 5\pi/3$

$$\Theta + \text{const.} = \arctan\left(\sqrt{3}\frac{g_2 - g_1}{2\,g_0 - g_1 - g_2}\right) \tag{A.27}$$

A.2 MATERIAL PROPERTIES OF TERLURAN® GP35

Parameters	Values
Density, kg/m^3	1040
MVR ISO 1133 [200° C/10 kg], $cm^3/10\,min$	34
Thermal conductivity, W/(m K)	0.17
Molding shrinkage, %	$0.4 - 0.7$
Heat deflection temperature (HDT, A: 1.80 Mpa), °C	78
Heat deflection temperature (HDT, B: 0.49 Mpa), °C	89
Melt temperature range, °C	$220 - 260$

A.3 ESTIMATES FOR THE MINIMUM CURVATURE RADIUS OF INSPECTED PARTS

The minimal curvature radius of a part's surface which can still be inspected is estimated according to the minimal allowed dimensions of the screen's image which is reflected from the part's surface. Considering Figure 4.8, it is suggested that the dimensions of the screen's image should not be smaller than 2 cm. This size of the screen's image allows the measurement of a sink mark and a conveniently large area of its surroundings to provide a good baseline for sink mark analysis. Additionally, the dimensions of the screen's image should not be smaller for efficiency's sake, since its size also defines the area size of the surface which can be measured with one measurement. Considering the comparatively long measurement time of this method, the number of measurements has to be kept as small as possible.

Using these considerations for the minimal dimensions of the screen's image, the theory of spherical mirrors is used to roughly estimate the minimal curvature radius of the part's surface [55]. The mirror equation

$$\frac{1}{d_o} + \frac{1}{d_i} = -\frac{2}{R} \tag{A.28}$$

relates the radius of a spherical mirror R to the distance of an object d_o and the distance of the image d_i. The radius R is positive for convex mirrors ($R > 0$) and negative for concave mirrors ($R < 0$).

The magnification m is the ratio between size of an object s_o and its image s_i and is calculated from

$$m = \frac{s_i}{s_o} = -\frac{d_i}{d_o} \tag{A.29}$$

where the distance of image d_i is positive for real images (image in front of the mirror, $d_i > 0$) and negative for for virtual images (image behind the mirror, $d_i < 0$). Combination of Equation A.28 with Equation A.29 and considering all sign changes give for convex mirrors

$$m = \frac{1}{\frac{2\,d_0}{R} + 1} \tag{A.30}$$

and for concave mirrors

$$m = \frac{1}{\frac{2\,d_0}{R} - 1} \qquad with \quad d_o > |R|/2 > 0\,. \tag{A.31}$$

Considering the applied screen type Eizo FlexScan EV2333W in the proposed testing site with the smaller screen dimension of 30 cm (s_o), the minimal dimension of the screen's image of 2 cm (s_i) and the proposed distance between screen and inspected part of 50 cm (d_o), we get for the minimal curvature radius of the part's surface (R, concave or convex surface) about 7 cm.

LIST OF APPREVIATIONS AND SYMBOLS

BRDF	bi-directional reflectance distribution function
DLT	direct linear transformation
ROI	region-of-interest
E	electric field strength
E_0	amplitude of the oscillating electric field vector
H	magnetic field strength
r	position vector
ω	angular frequency
k	wave vector
k_I, k_R, k_T	wave vectors for incident, reflected and transmitted elecromagnetic waves
K	complex wave number
k	real wave number
α	absorption loss coefficient (imaginary wave number)
N	complex refractive index
n	real refractive index
κ	extinction coefficient (imaginary refractive index)
v	phase speed
c	speed of light
$R_\perp$	Fresnel factor for perpendicularly polarized reflected electromagnetic waves
$T_\perp$	Fresnel factor for perpendicularly polarized transmitted electromagnetic waves
$R_\parallel$	Fresnel factor for parallelly polarized reflected electromagnetic waves
$T_\parallel$	Fresnel factor for parallelly polarized transmitted electromagnetic waves
m	mapping function

$\hat{s}$	unit position vector of the screen pixels
$\hat{c}$	unit position vector of the camera sensor
$\hat{n}$	unit normal vector
w_j	window function
W	Fourier transformed window function
Θ	phase information
Φ	phase shift
$g(\Theta, t)$	phase intensity
$G(\Theta, \nu)$	Fourier transformed phase intensity
ν_0	constant frequency shift
c_j	real part of the window function w_j
s_j	imaginary part of the window function w_j
L	maximum length of one screen dimension
p_j	generated phase-shifted patterns
g_j	images of the patterns
$f(u)$	parametrized form of a regular surface
s	arc length
W	Weingarten matrix
$\hat{W}$	numerical approximation of Weingarten matrix
κ_{mean}	mean curvature
κ_{max}, κ_{min}	principal curvatures (maximum, minimum)
V	Vandermonde matrix
s	coefficient vector
B	matrix of orthonormal polynomial base functions
b_0	column vector of B
d	degree of polynomial base functions
d_{max}	maximum degree of polynomial base functions
l_s	support length of polynomial base functions
S	local approximation matrix
G	matrix operator for conventional gradients
D	local differentiation matrix
A_i	Amplitudes of the peaks
η_i	Ratios of the superposition in Equation 4.2

μ_{xi}, μ_{yi}	Position coordinates of the function peaks
σ_{xi}, σ_{yi}	Standard deviations of the Gaussians
b_{xi}, b_{yi}	Half-axes of bump function areas
μ_2	second moment of a distribution
μ_4	fourth moment of a distribution
V	topografic feature parameter sink mark volume
d_i	distance of image to a spherical mirror
d_o	distance of an object to a spherical mirror
s_i	image size
s_o	object size
R	radius of a spherical mirror

LIST OF FIGURES

LIST OF TABLES

LIST OF ALGORITHMS

BIBLIOGRAPHY

[1] 3D-Shape GmbH. *SpecGage3D*. http://www.3d-shape.com/produkte/pmd_d.php. [Online; accessed 10-January-2014]. 2013 (cit. on p. 6).

[2] G. Abts. *Kunststoff-Wissen für Einsteiger*. Carl Hanser Verlag, 2010 (cit. on pp. 15, 16).

[3] K. Atsushi et al. "System for reconstruction of three-dimensional micro objects from multiple photographic images." In: *Computer-Aided Design* 43.8 (Aug. 2011), pp. 1045–1055. ISSN: 00104485. DOI: 10.1016/j.cad.2011.01.019 (cit. on p. 3).

[4] S. K. H. Auluck. "High-sensitivity Diffraction-compensated Moiré Deflectometry." In: *Journal of Modern Optics* 41.4 (Apr. 1994), pp. 791–805. ISSN: 0950-0340. DOI: 10.1080/09500349414550801 (cit. on p. 4).

[5] J. Balzer and S. Werling. "Principles of shape from specular reflection." In: *Measurement* 43.10 (2010), pp. 1305–1317. ISSN: 0263-2241. DOI: 10.1016/j.measurement.2010.07.013 (cit. on pp. 5, 25).

[6] J. Balzer, S. Werling, and J. Beyerer. "Deflektometrische Rekonstruktion teilspiegelnder Freiformflächen (Deflectometric Reconstruction of Partially Specular Free-Form Surfaces)." In: *tm - Technisches Messen* 74.11 (Nov. 2007), pp. 545–552. ISSN: 0171-8096. DOI: 10.1524/teme.2007.74.11.545 (cit. on p. 5).

[7] C. Bär. *Elementare Differentialgeometrie*. 2nd. de Gruyter, 2010 (cit. on pp. 33, 106).

[8] N. Bauer. *Handbuch zur Industriellen Bildverarbeitung*. Ed. by N. Bauer. Stuttgart: Fraunhofer IRB Verlag, 2008, pp. 1–499. ISBN: 978-3-8167-7386-3 (cit. on p. 3).

[9] BeagleBoard.org Foundation. *BeagleBoard.org*. http://www.beagleboard.org. [Online; accessed 10-January-2014]. 2013 (cit. on p. 102).

[10] D. Bedeaux and J. Vlieger. *Optical Properties of Surfaces*. 2nd. London: Imperial College Press, 2004, pp. 1–450. ISBN: 1860944507 (cit. on p. 9).

[11] S. Belongie, J. Malik, and J. Puzicha. "Shape Matching and Object Recognition Using Shape Contexts." In: *IEEE Transaction on Pattern Analysis and Machine Intelligence* 24.24 (2002), pp. 509–522 (cit. on pp. 63, 65).

[12] S. Belongie, G. Mori, and J. Malik. "Matching with Shape Contexts." In: *IEEE Workshop on Contentbased Access of Image and Video Libraries (CBAIVL-2000)*. Hilton Head Island, 2000, pp. 20–26 (cit. on pp. 63, 65).

[13] M. Ben-Ezra, J. Wang, and B. Wilburn. "An LED-only BRDF measurement device." In: *2008 IEEE Conference on Computer Vision and Pattern Recognition* i (June 2008), pp. 1–8. DOI: 10.1109/CVPR.2008.4587766 (cit. on p. 2).

[14] J.-Y. Bouguet. *Camera Calibration Toolbox for Matlab*. http://www.vision.caltech.edu/bouguetj/calib_doc/. Software. [Online; accessed 10-January-2014]. 2013 (cit. on p. 102).

[15] S. R. Bowling et al. "An Empirical Study on the Effect of Arrangement on Performance of Two Inspectors." In: *Industrial Engineering Research Conference*. Houston TX, 2004, pp. 1–6 (cit. on p. 1).

[16] R. L. Burden and J. D. Faires. *Numerical Analysis*. 9th. Boston: Cengage Learning, 2011, pp. 1–872. ISBN: 9780538733519 (cit. on p. 46).

[17] E. A. Campo. *The Complete Part Design Handbook - For Injection Molding of Thermoplastics*. Carl Hanser Verlag, 2006 (cit. on pp. 16, 17).

[18] Carl Zeiss OIM GmbH. *SurfMax*. http://www.zeiss.de/c125765c0043e76f/Contents-Frame/56ec88f30c98197fc1257730003dfcd1. [Online; accessed 10-January-2014]. 2013 (cit. on p. 6).

[19] M. J. Chantler. "The effect of variation in illuminant direction on texture classification." PhD thesis. Heriot-Watt University, 1994 (cit. on p. 2).

[20] M. J. Chantler. "Why illuminant direction is fundamental to texture analysis." In: *IEEE Proceedings of Vision, Image and Signal Processing* 142.4 (1995), pp. 199–206 (cit. on p. 2).

[21] M. J. Chantler and G. McGunnigle. "The response of texture features to illuminant rotation." In: *Proceedings 15th International Conference on Pattern Recognition. ICPR*. Vol. 3. 1. IEEE Comput. Soc, 2000, pp. 943–946. ISBN: 0-7695-0750-6. DOI: 10.1109/ICPR.2000.903700 (cit. on p. 2).

[22] H.-S. Chung. "Efficient photometric stereo on glossy surfaces with wide specular lobes." In: *2008 IEEE Conference on Computer Vision and Pattern Recognition* (June 2008), pp. 1–8. DOI: 10.1109/CVPR.2008.4587771 (cit. on p. 4).

[23] R. L. Cook and K. E. Torrance. "A Reflectance Model for Computer Graphics." In: *ACM Transactions on Graphics*. 1982 (cit. on pp. 15, 104).

[24] K. Creath and J. C. Wyant. "Moiré and Fringe Projection Techniques." In: *Optical Shop Testing*. Ed. by D. Malacara. 2nd. John Wiley & Sons, inc., 1992. Chap. 16, pp. 653–685. ISBN: 0471522325 (cit. on p. 4).

[25] K. Dana, O. Cula, and J. Wang. "Surface detail in computer models." In: *Image and Vision Computing* 25.7 (July 2007), pp. 1037–1049. ISSN: 02628856. DOI: 10.1016/j.imavis.2006.04.022 (cit. on p. 2).

[26] K. J. Dana. "BRDF / BTF Measurement Device." In: *ICCV 2001*. IEEE Computer Society, 2001, pp. 460–466 (cit. on p. 2).

[27] K. J. Dana and J. Wang. "Device for convenient measurement of spatially varying bidirectional reflectance." In: *Journal of the Optical Society of America. A* 21.1 (Jan. 2004), pp. 1–12. ISSN: 1084-7529 (cit. on p. 104).

[28] C. Domokos and Z. Kato. "Affine Puzzle : Realigning Deformed Object Fragments without Correspondences." In: *Computer Vision - ECCV 2010*. Ed. by K. Daniilidis, P. Maragos, and N. Paragios. Springer Berlin Heidelberg, 2010, pp. 777–790. DOI: 10.1007/978-3-642-15552-9_56 (cit. on pp. 63, 65).

[29] C. Domokos, J. Nemeth, and Z. Kato. "Nonlinear Shape Registration without Correspondences." In: *IEEE Transactions on Pattern Analysis and Machine Intelligence* 34.5 (May 2012), pp. 943–58. ISSN: 1939-3539. DOI: 10.1109/TPAMI.2011.200 (cit. on pp. 63, 65).

[30] G. Farin. *Curves and Surfaces for CAGD - A Practical Guide*. Ed. by D. D. Cerra. 5th. Academic Press, 2002 (cit. on pp. 33, 106).

[31] P. Fechteler, P. Eisert, and J. Rurainsky. "Fast and High Resolution 3D Face Scanning." In: *2007 IEEE International Conference on Image Processing*. Vol. 3. IEEE, 2007, pp. III81–III84. ISBN: 978-1-4244-1436-9. DOI: 10.1109/ICIP.2007.4379251 (cit. on p. 3).

[32] J. Filip and M. Haindl. "Bidirectional texture function modeling: a state of the art survey." In: *IEEE transactions on pattern analysis and machine intelligence* 31.11 (Nov. 2009), pp. 1921–40. ISSN: 1939-3539. DOI: 10.1109/TPAMI.2008.246 (cit. on p. 104).

[33] Y. Francken et al. "High quality mesostructure acquisition using specularities." In: *IEEE Conference on Computer Vision and Pattern Recognition, 2008. CVPR 2008.* Ieee, June 2008, pp. 1–7. ISBN: 978-1-4244-2242-5. DOI: 10.1109/CVPR.2008.4587782 (cit. on p. 24).

[34] Y. Francken et al. "Gloss and Normal Map Acquisition of Mesostructures Using Gray Codes." In: *Advances in Visual Computing* Part II.LNCS 5876 (2009), pp. 788–798 (cit. on p. 24).

[35] P. de Groot. "Derivation of algorithms for phase-shifting interferometry using the concept of data sampling window." In: *Applied Optics* 34.22 (1995), pp. 4723–4730 (cit. on pp. 24, 25, 113).

[36] D. P. Gruber et al. "A novel methodology for the evaluation of distinctness of image of glossy surfaces." In: *Progress in Organic Coatings* 63.4 (2008), pp. 377–381 (cit. on p. 3).

[37] D. P. Gruber et al. "Characterization of gloss properties of differently, treated polymer coating surfaces by surface, clarity measurement methodology." In: *Applied Optics* 51.20 (2012), pp. 4833–4840 (cit. on pp. 77, 104).

[38] D. Gruber, G. Meinhardt, and W. Papousek. "Spatial distribution of light absorption in organic photovoltaic devices." In: *Solar Energy* 79.6 (Dec. 2005), pp. 697–704. ISSN: 0038092X. DOI: 10.1016/j.solener.2005.06.008 (cit. on p. 9).

[39] D. P. Gruber. *Method for Automatically Detecting a Defect on a Surface of a Molded Part*. Patent, WO 2012/102319 A1. Pat. 2010 (cit. on p. 3).

[40] D. P. Gruber, G. Meinhardt, and W. Papousek. "Modeling the light absorption in organic photovoltaic devices." In: *Solar Energy Materials & Solar Cells* 87 (2005), pp. 215–223 (cit. on p. 77).

[41] D. P. Gruber et al. "Modeling the absorption behavior of solar thermal collector coatings utilizing graded α-C:H=TiC layers." In: *Applied Optics* 48.8 (2009), pp. 1514–1519 (cit. on p. 77).

[42] D. P. Gruber et al. "Novel approach to the measurement of the visual perceptibility of sink marks on injection molding parts." In: *Polymer Testing* 30.6 (Sept. 2011), pp. 651–656. ISSN: 01429418. DOI: 10.1016/j.polymertesting.2011.04.013 (cit. on pp. 3, 6, 18, 76).

[43] D. P. Gruber et al. "Measurement of the visual perceptibility of sink marks on injection molding parts by a new fast processing model." In: *Polymer Testing* 33 (Feb. 2014), pp. 7–12. ISSN: 01429418. DOI: 10.1016/j.polymertesting.2013.10.014 (cit. on pp. 6, 18, 81).

[44] D. Gruber et al. "A novel methodology for the evaluation of distinctness of image of glossy surfaces." In: *Progress in Organic Coatings* 63.4 (Nov. 2008), pp. 377–381. ISSN: 03009440. DOI: 10.1016/j.porgcoat.2008.06.008 (cit. on pp. 3, 104).

[45] J. Gu et al. "Time-Varying Surface Appearance : Acquisition , Modeling and Rendering." In: *ACM SIGGRAPH 2006*. 2006 (cit. on p. 2).

[46] E. Hack and J. Burke. "Measurement uncertainty of linear phase-stepping algorithms." In: *Review of Scientific Instruments* 82.6 (2011), pp. 061101–061101. DOI: 10.1063/1.3603452. (cit. on p. 27).

[47] M. Halstead et al. "Reconstructing curved surfaces from specular reflection patterns using spline surface fitting of normals." In: *Proceedings of the 23rd annual conference on Computer graphics and interactive techniques - SIGGRAPH '96*. New York, New York, USA: ACM Press, 1996, pp. 335–342. ISBN: 0897917464. DOI: 10.1145/237170.237272 (cit. on p. 4).

[48] M. Harker and P. O'Leary. "Least squares surface reconstruction from measured gradient fields." In: *IEEE Conference on Computer Vision and Pattern Recognition*. IEEE, June 2008, pp. 1–7. ISBN: 978-1-4244-2242-5. DOI: 10.1109/CVPR.2008.4587414 (cit. on p. 39).

[49] M. Harker and P. O'Leary. "Least squares surface reconstruction from gradients: Direct algebraic methods with spectral, Tikhonov, and constrained regularization." In: *CVPR 2011*. IEEE, June 2011, pp. 2529–2536. ISBN: 978-1-4577-0394-2. DOI: 10.1109/CVPR.2011.5995427 (cit. on pp. 39, 105).

[50] M. Harker and P. O'Leary. *Matlab Central: Discrete Orthogonal Polynomial Toolbox*. http://www.mathworks.com/matlabcentral/fileexchange/41250-discrete-orthogonal-polynomial-toolbox-dopbox-version-1-7. Software. [Online; accessed 28-January-2014]. 2013 (cit. on pp. 2, 6, 39, 46, 72).

[51] R. Hartley and A. Zisserman. *Multiple View Geometry in Computer Vision*. 2nd. Cambridge University Press, 2010, pp. 1–653. ISBN: 978-0-521-54051-3 (cit. on pp. 3, 63, 102, 106).

[52] V. Havran et al. "On cross-validation and resampling of BRDF data measurements." In: *Proceedings of the 21st spring conference on Computer graphics - SCCG '05*. New York, New York, USA: ACM Press, 2005, p. 161. ISBN: 1595932036. DOI: 10.1145/1090122.1090149 (cit. on pp. 2, 104).

[53] K. F. Hayden. “Determining the probability of the visual detection of sink marks on differently textured injection molded products.” PhD thesis. Western Michigan University, 2006 (cit. on pp. 1, 6, 16, 18, 19, 70, 88).

[54] G. Healey and T. O. Binford. “Local shape from specularity.” In: *Computer Vision, Graphics, and Image Processing* 42.1 (1988), pp. 62–86 (cit. on p. 4).

[55] E. Hecht. *Optik*. German. Bonn: Addison-Wesley (Deutschland) GmbH, 1989, pp. 1–718. ISBN: 3-925118-86-1 (cit. on pp. 9, 12, 14, 119).

[56] K. Hibino et al. “Phase-shifting algorithms for nonlinear and spatially nonuniform phase shifts.” In: *J. Opt. Soc. Am. A* 14.4 (2006), pp. 918–930 (cit. on p. 27).

[57] K. Hibino et al. “Phase shifting for nonsinusoidal waveforms with phase-shift errors.” In: *J. Opt. Soc. Am. A* 12.4 (1995), pp. 761–768 (cit. on p. 27).

[58] T. Higo, Y. Matsushita, and K. Ikeuchi. “Consensus photometric stereo.” In: *IEEE Conference on Computer Vision and Pattern Recognition (CVPR)*. IEEE, 2010, pp. 1157–1164 (cit. on p. 4).

[59] S. Höfer, S. Werling, and J. Beyerer. “Verfahren zur Erzeugung dynamischer Wärmemuster für die Anwendung in der Infrarotdeflektometrie.” In: *Tagungsband des XXVI. Messtechnisches Symposiums*. Ed. by R. Schmitt. Shaker, 2012 (cit. on p. 6).

[60] S. Höfer, S. Werling, and J. Beyerer. “Thermal Pattern Generation for Infrared Deflectometry.” In: *Proceedings SENSOR 2013*. Nürnberg, 2013 (cit. on pp. 6, 25, 57, 62, 104).

[61] S. Höfer et al. “Verfahren und Vorrichtung zur Inspektion von Glasoberflächen.” In: *Tagungsband des XXV. Messtechnisches Symposiums*. Ed. by F. P. León and J. Beyerer. Karlsruhe: Shaker, 2011, pp. 127–138 (cit. on p. 6).

[62] J. W. Horbach and T. Dang. “3D reconstruction of specular surfaces using a calibrated projectorâ€“camera setup.” In: *Machine Vision and Applications* 21.3 (Mar. 2009), pp. 331–340. ISSN: 0932-8092. DOI: 10.1007/s00138-008-0165-8 (cit. on pp. 5, 105).

[63] C. Horneber, M. C. Knauer, and G. Häusler. “Phase Measuring Deflectometry – A New Method to Measure Reflecting Surfaces.” In: *Annual Report*. Vol. 7. Universität Erlangen-Nürnberg. 2000, p. 7 (cit. on pp. 1, 5).

[64] R. S. Hunter. "Methods of Determining Gloss." In: *Journal of Research, NBS* 17.77 (1937), p. 281 (cit. on p. 14).

[65] I. Ihrke et al. "Transparent and Specular Object Reconstruction." In: *Computer Graphics Forum* 29.8 (Dec. 2010), pp. 2400–2426. ISSN: 01677055. DOI: 10.1111/j.1467-8659.2010.01753.x (cit. on p. 3).

[66] K. Ireland and M. Rosen. *A Classical Introduction to Modern Number Theory*. Ed. by J. H. Ewing, F. W. Gehring, and P. R. Halmos. Second. Springer-Verlag New York, 1990 (cit. on p. 31).

[67] F. Johannaber, B. Lungstras, and W. Michaeli. *Handbuch Spritzgießen*. 2nd. Carl Hanser Verlag, 2004 (cit. on pp. 15, 16, 92).

[68] S. G. Johnson. *Saddle-Point Integration of C∞ "Bump" Functions*. http://www-math.mit.edu/~stevenj/bump-saddle.pdf. [Online; accessed 05-March-2014]. June 2007 (cit. on p. 82).

[69] S. Kammel and F. Leon. "Deflectometric Measurement of Specular Surfaces." In: *IEEE Instrumentation and Measurement Technology*. Ottawa: Ieee, 2005, pp. 531–536. ISBN: 0-7803-8879-8. DOI: 10.1109/IMTC.2005.1604173 (cit. on pp. 5, 22, 24, 25, 38).

[70] S. Kammel. "Deflektometrie zur Qualitätsprüfung spiegelnd reflektierender Oberflächen (Deflectometry for Quality Control of Specular Surfaces)." In: *Technisches Messen/Sensoren, Geräte, Systeme* 70.4/2003 (2003), pp. 193–198 (cit. on p. 5).

[71] S. Kammel. *Deflektometrische Untersuchung spiegelnd reflektierender Freiformflächen*. Vol. Dissertation, Universität Karlsruhe (TH), Fakultät für Maschinenbau. ISBN 3-937300-28-7. Universitätsverlag Karlsruhe, 2004 (cit. on pp. 27, 57).

[72] S. Kammel and F. P. León. "Deflectometric Measurement of Specular Surfaces." In: *IEEE Transactions on Instrumentation and Measurement* 57.4 (2008), pp. 763–769 (cit. on pp. 5, 22, 24, 25, 38).

[73] M. Keuerleber and P. Eyerer. "Gestalten, Fügen, Berechnungsansätze und Simulation EDV-unterstützter Konstruktionen und Auslegung von Kunststoffbauteilen." In: *Polymer Engineering*. Ed. by P. Eyerer, T. Hirth, and P. Elsner. Berlin, Heidelberg: Springer Berlin Heidelberg, 2008. Chap. 6, pp. 466–485. ISBN: 978-3-540-72402-5. DOI: 10.1007/978-3-540-72419-3 (cit. on pp. 1, 16).

[74] G. Kigle-Boeckler. "Measurement of gloss and reflection properties of surfaces." In: *Met. Finish.* 93.5 (May 1995), pp. 28–31. ISSN: 0026-0576. DOI: 10.1016/0026-0576(95)90685-B (cit. on p. 14).

[75] S. Kitaguchi et al. *Surface Texture - A Review*. Tech. rep. September. National Physical Laboratory, 2004, pp. 1–72 (cit. on p. 2).

[76] J. Kiusalaas. *Numerical Methods in Engineering with MATLAB*. Cambridge: Cambridge University Press, 2005, p. 426. ISBN: 9780511812200. DOI: 10.1017/CBO9780511812200 (cit. on p. 46).

[77] D. W. van Krevelen and K. te Nijenhuis. *Properties of Polymers: Their Correlation with Chemical Structure; their Numerical Estimation and Prediction from Additive Group Contributions*. 4th edition. Elsevier, 2009. ISBN: 978-0-08-054819-7 (cit. on p. 13).

[78] J. Lellmann et al. "Shape from Specular Reflection and Optical Flow." In: *International Journal of Computer Vision* 80.2 (Jan. 2008), pp. 226–241. ISSN: 0920-5691. DOI: 10.1007/s11263-007-0123-3 (cit. on p. 5).

[79] Y. Li and P. Gu. "Free-form surface inspection techniques state of the art review." In: *Computer-Aided Design* 36.13 (Nov. 2004), pp. 1395–1417. ISSN: 00104485. DOI: 10.1016/j.cad.2004.02.009 (cit. on p. 3).

[80] C. W. Liao et al. "Application of the structured illumination method for automated visual inspection of the loudspeaker cones." In: *Journal of Materials Processing Technology* 200.1-3 (May 2008), pp. 59–70. ISSN: 09240136. DOI: 10.1016/j.jmatprotec.2007.11.262 (cit. on p. 3).

[81] A. J. MacGovern and J. C. Wyant. "Computer generated holograms for testing optical elements." In: *Applied optics* 10.3 (Mar. 1971), pp. 619–24. ISSN: 0003-6935 (cit. on p. 4).

[82] D. Malacara, M. Serín, and Z. Malacara. *Interferogram Analysis for Optical Testing*. 2nd. CRC Press, 2005 (cit. on p. 27).

[83] A. Mital, M. Govindaraju, and B. Subramani. "A comparison between manual and hybrid methods in parts inspection." In: *Integrated Manufacturing Systems* 9.6 (1998), pp. 344–349. ISSN: 0957-6061. DOI: 10.1108/09576069810238709 (cit. on p. 1).

[84] S. K. Nayar, K. Ikeuchi, and T. Kanade. "Surface reflection: physical and geometrical perspectives." In: *IEEE Transactions on Pattern Analysis and Machine Intelligence* 13.7 (1991), pp. 611–634. ISSN: 0162-8828 (cit. on p. 14).

[85] H.-F. Ng. "Automatic thresholding for defect detection." In: *Pattern Recognition Letters* 27.14 (Oct. 2006), pp. 1644–1649. ISSN: 01678655. DOI: 10.1016/j.patrec.2006.03.009 (cit. on p. 30).

[86] F. E. Nicodemus et al. *Geometrical considerations and nomenclature for reflectance*. Tech. rep. October. Washington, D.C.: U.S. Department of Commerce, National Bureau of Standards, 1977 (cit. on pp. 2, 103).

[87] P. O'Leary and M. Harker. "An Algebraic Framework for Discrete Basis Functions in Computer Vision." In: *IEEE Sixth Indian Conference on Computer Vision, Graphics & Image Processing*. 1. Bhubaneswar: IEEE, Dec. 2008, pp. 150–157. DOI: 10.1109/ICVGIP.2008.107 (cit. on pp. 2, 6, 40).

[88] P. O'Leary and M. Harker. "Discrete polynomial moments for real-time geometric surface inspection." In: *Journal of Electronic Imaging* 18.1 (2009), p. 013015. ISSN: 10179909. DOI: 10.1117/1.2987725 (cit. on pp. 39–42, 67).

[89] P. O'Leary and M. Harker. "Discrete Polynomial Moments and Savitzky-Golay Smoothing." In: *World Academy of Science, Engineering and Technology* 48 (2010), pp. 440–444 (cit. on pp. 2, 6).

[90] P. O'Leary and M. Harker. "Polynomial approximation: An alternative to windowing in Fourier analysis." In: *IEEE International Instrumentation and Measurement Technology Conference*. 4. IEEE, May 2011, pp. 1–6. ISBN: 978-1-4244-7933-7. DOI: 10.1109/IMTC.2011.5944262 (cit. on p. 39).

[91] P. O'Leary and M. Harker. "A Framework for the Evaluation of Inclinometer Data in the Measurement of Structures." In: *IEEE Transactions on Instrumentation and Measurement* 61.5 (May 2012), pp. 1237–1251. ISSN: 0018-9456. DOI: 10.1109/TIM.2011.2180969 (cit. on pp. 2, 6, 39, 41, 42, 45, 46).

[92] P. O'Leary and M. Harker. "Surface Modelling using Discrete Basis Functions for Real-Time Automatic Inspection." In: *3-D Surface Geometry and Reconstruction*. Ed. by U. C. Pati. IGI Global, 2012. DOI: 10.4018/978-1-4666-0113-0.ch010 (cit. on pp. 39, 46).

[93] P. O'Leary, M. Harker, and J. Golser. "Direct discrete variational curve reconstruction from derivatives and its application to track subsidence measurements." In: *IEEE International Instrumentation and Measurement Technology Conference*. Hangzhou: IEEE, May 2011, pp. 1–6. ISBN: 978-1-4244-7933-7. DOI: 10.1109/IMTC.2011.5944013 (cit. on p. 39).

[94] P. O'Leary, M. Harker, and R. Neumayr. "Savitzky-Golay smoothing for multivariate cyclic measurement data." In: *IEEE Instrumentation & Measurement Technology Conference*. Austin: IEEE, 2010,

pp. 1585–1590. ISBN: 978-1-4244-2832-8. DOI: 10.1109/IMTC.2010.5488242 (cit. on pp. 39, 40, 42).

[95] A. V. Oppenheimer and R. W. Schafer. *Discrete-Time Signal Processing*. 2nd edition. Upper Saddle River, New Jersey: Prentice Hall, 1999. ISBN: 0-13-754920-2 (cit. on p. 42).

[96] Orientalmotor. *DG130R-ARAC-1*. http://www.orientalmotor.de/Products/Linear_rotary_actuators/Hollow_rotary_actuators/Pulse_input_dgii/?arid=9847. [Online; accessed 23-October-2013]. 2013 (cit. on p. 99).

[97] Orientalmotor. *DG85R-ARAC-1*. http://www.orientalmotor.de/Products/Linear_rotary_actuators/Hollow_rotary_actuators/Pulse_input_dgii/?arid=9841. [Online; accessed 23-October-2013]. 2013 (cit. on p. 99).

[98] T. A. Oswald and J. P. Hernández-Oritz. *Polymer Processing - Modelling and Simulation*. Carl Hanser Verlag, 2006 (cit. on pp. 15, 16).

[99] N. Otsu. "A Threshold Selection Method from Gray-Level Histograms." In: *IEEE Transactions on Systems, Man, and Cybernetics* 9.1 (1979), pp. 62–66. ISSN: 0018-9472. DOI: 10.1109/TSMC.1979.4310076 (cit. on p. 30).

[100] G. A. Pacher et al. "Influence of Process Settings on the Topography of Sink Marks." In: *Proceedings of Advances in Plastics Technology*. Sosnowiec, PL., Oct. 2013 (cit. on pp. 81, 83).

[101] PI miCos GmbH. *Rotation Stage DT-80 R*. http://www.pimicos.com/web2/en/1,5,130,dt80r.html. [Online; accessed 28-November-2012]. 2012 (cit. on p. 56).

[102] M. R. Pointer. *Measuring Visual Appearance*. Tech. rep. November. NPL Report COAM 19, 2003, pp. 1–102 (cit. on p. 18).

[103] D. Qin et al. "3-D Shape Measurement of Complex Objects by Combining Color-Coded Fringe and Neural Networks." In: *Tsinghua Science & Technology* 14.June (June 2009), pp. 66–70. ISSN: 10070214. DOI: 10.1016/S1007-0214(09)70069-0 (cit. on p. 3).

[104] H. Rapp and C. Stiller. "Deflektometrische Methoden zur Sichtprüfung und 3D-Vermessung voll reflektierender Freiformflächen." In: *Forum Bildverarbeitung 2010*. 2010 (cit. on pp. 22, 24, 105).

[105] Raspberry Pi Foundation. *Raspberry Pi*. http://www.raspberrypi.org. [Online; accessed 10-January-2014]. 2013 (cit. on p. 102).

[106] R. Ritter and R. Hahn. "Contribution to analysis of the reflection grating method." In: *Optics and Lasers in Engineering* 4.1 (1983), pp. 13–24. ISSN: 0143-8166 (cit. on p. 4).

[107] C. Runge. "Über empirische Funktionen und die Interpolation zwischen äquidistanten Ordinaten." In: *Zeitschrift für Mathematik und Physik* 64 (1901), pp. 224–243 (cit. on p. 42).

[108] G. Sansoni, M. Carocci, and R. Rodella. "Three-Dimensional Vision Based on a Combination of Gray-Code and Phase-Shift Light Projection: Analysis and Compensation of the Systematic Errors." In: *Applied Optics* 38.31 (Nov. 1999), p. 6565. ISSN: 0003-6935. DOI: 10.1364/AO.38.006565 (cit. on p. 31).

[109] G. Sansoni, M. Trebeschi, and F. Docchio. "State-of-The-Art and Applications of 3D Imaging Sensors in Industry, Cultural Heritage, Medicine, and Criminal Investigation." In: *Sensors* 9.1 (Jan. 2009), pp. 568–601. ISSN: 1424-8220. DOI: 10.3390/s90100568 (cit. on p. 3).

[110] E. Savio, L. Dechiffre, and R. Schmitt. "Metrology of freeform shaped parts." In: *CIRP Annals - Manufacturing Technology* 56.2 (2007), pp. 810–835. ISSN: 00078506. DOI: 10.1016/j.cirp.2007.10.008 (cit. on p. 3).

[111] A. Savitzky and M. J. E. Golay. "Smoothing and Differentiation of Data by Simplified Least Squares Procedures." In: *Analytical Chemistry* 36.8 (July 1964), pp. 1627–1639. ISSN: 0003-2700. DOI: 10.1021/ac60214a047 (cit. on p. 46).

[112] R. Silvennoinen, K.-E. Peiponen, and K. Myller. *Specular Gloss*. Amsterdam: Elsevier Ltd., 2008, pp. 1–494. ISBN: 978-0-0804-5314-9 (cit. on p. 3).

[113] C. Teutsch et al. "Automated geometry measurement of wheel rims based on optical 3D metrology." In: *Proceedings of SPIE* 1 (2006), p. 63820I. ISSN: 0277786X. DOI: 10.1117/12.685547 (cit. on p. 3).

[114] Thorlabs. *NR360S/M - NanoRotator Stage with SM2-Threaded Center Hole, Metric*. http://www.thorlabs.de/thorproduct.cfm?partnumber=NR360S/M. [Online; accessed 28-November-2013]. 2012 (cit. on p. 56).

[115] P. Vachiramon. *Matlab Central: Fullscreen*. http://www.mathworks.com/matlabcentral/fileexchange/11112-fullscreen. [Online; accessed 5-January-2012]. 2006 (cit. on p. 59).

[116] B. Wang. "Moire deflectometry based on Fourier-transform analysis." In: *Measurement* 25.4 (June 1999), pp. 249–253. ISSN: 02632241. DOI: 10.1016/S0263-2241(99)00009-3 (cit. on p. 4).

[117] G. J. Ward. "Measuring and Modeling Anisotropic Reflection." In: *SIGGRAPH Computer Graphics* 26.2 (1992), pp. 265–272 (cit. on pp. 15, 104).

[118] A. Weckenmann et al. "Multisensor data fusion in dimensional metrology." In: *CIRP Annals - Manufacturing Technology* 58.2 (2009), pp. 701–721. ISSN: 00078506. DOI: 10.1016/j.cirp.2009.09.008 (cit. on p. 3).

[119] S. B. Werling. *Deflektometrie zur automatischen Sichtprüfung und Rekonstruktion spiegelnder Oberflächen*. Ed. by J. Beyerer. KIT Scientific Publishing, 2011 (cit. on pp. 57, 58, 64, 102, 104, 105).

[120] S. Werling and J. Beyerer. "Automatische Inspektion spiegelnder Oberflächen mittels inverser Muster (Inspection of Specular Surfaces with Inverse Patterns)." In: *tm - Technisches Messen* 74.4 (Apr. 2007), pp. 217–223. ISSN: 0171-8096. DOI: 10.1524/teme.2007.74.4.217 (cit. on pp. 5, 64).

[121] H. B. Wu et al. "3D Measurement Technology by Structured Light Using Stripe-Edge-Based Gray Code." In: *Journal of Physics: Conference Series* 48.1 (2006), p. 537 (cit. on p. 24).

[122] X. Xie. "A review of recent advances in surface defect detection using texture analysis techniques." In: *Electronic Letters on Computer Vision and Image Analysis* 7.3 (2008), pp. 1–22 (cit. on p. 2).

[123] M. Yamazaki and G. Xu. "3D Reconstruction of Glossy Surfaces Using Stereo Cameras and Projector-Display." In: *IEEE Conference on Computer Vision and Pattern Recognition (CVPR)*. 2010, pp. 1213–1220 (cit. on p. 3).

[124] L. R. Yu and L. B. Luo. "The Generalization of the Chinese Remainder Theorem." In: *Acta Mathematica Sinica* 18.3 (July 2002), pp. 531–538 (cit. on p. 31).

[125] Z. Zhang. *A Flexible New Technique for Camera Calibration*. Tech. rep. MSR-TR-98-71. Microsoft Research, 1998, pp. 1–22 (cit. on p. 102).

[126] Z. Zhang. "Flexible Camera Calibration By Viewing a Plane From Unknown Orientations." In: *ICCV*. 1999, pp. 666–673. ISBN: 0769501648 (cit. on p. 102).

COLOPHON

This document was typeset using the typographical look-and-feel `classicthesis` developed by André Miede. The style was inspired by Robert Bringhurst's seminal book on typography "*The Elements of Typographic Style*". `classicthesis` is available for both LaTeX and LyX:

`http://code.google.com/p/classicthesis/`

Final Version as of September 7, 2014 (`classicthesis` version 2).